University of California, Davis
Aeronautical and Environmental Wind Tunnel Facility
Department of Mechanical and Aeronautical Engineering
One Shields Avenue, Davis, California 95616-5294

Final Report **NASA Grant NAGS-6246**

MARS BOUNDARY LAYER STABILITY EXPERIMENTS OF DUST THRESHOLD

Bruce R. White, Principal Investigator

Rachael Coquilla, Graduate Student

Prepared for:
Reta Beebe
Planetary Atmospheres
Office of Space Science
National Aeronautics and Space Administration
300 E Street, SW
Washington, D.C. 20546

MAY 2001

EXECUTIVE SUMMARY

A wind tunnel was used to study the effects of a heated surface, thereby creating an unstable near-surface atmosphere, on the threshold of aeolian-blown dust particles under Mars-simulated pressure. Unstable conditions on Mars typically arise during the mid to late afternoon hours due to the accumulation of daytime solar-radiation. When the surface is warmer than the atmosphere just above it, vertical turbulence is increased. Thus, loose dust particles can be more easily lofted and mixed at a threshold wind speed lower than that known under neutral atmospheric conditions. For this wind-tunnel study, unstable surface conditions were simulated based on the negative temperature gradients and surface bulk Richardson numbers estimated from the Mars Pathfinder Lander (MPL) mission data during the mid-afternoon to early evening Mars period. According to other missions, evidence of highly active dust suspension during this part of the Mars daytime hours was recorded, including the presence of "dust devils". Experiments were performed in the Martian Surface Wind Tunnel (MARSWIT) located at NASA Ames Research Center, Moffett Field, California. Based on data acquired from the MPL site, the mean surface pressure was found to be *6.75 mb*. Thus, simulations in MARSWIT were conducted at *10-mb* atmospheric pressure using air, which agrees with a dynamically similar environment of *6.5 mb* on Mars. In order to attain the necessary vertical temperature gradients that would develop an unstable layer, a test bed was heated by sub-surface heaters. Three surface roughness conditions were simulated, over which not only dust threshold was measured but also velocity and temperature profiles were acquired under various heating levels. Boundary layer measurements and analysis conducted under neutral conditions were used to estimate roughness height, z_o, and the friction speed, u*, for all stability conditions. Dust threshold tests were conducted using a surrogate Mars soil, Carbondale Red Clay (CRC), which has a mean particle diameter of about *1* to *2* μm in dust form. According to boundary-layer analysis, two test beds, having $z_o = 0.015$ *mm* and *0.09 mm*, generated hydraulically smooth-wall turbulent flow. Under neutral stability conditions, the corresponding dust threshold frictions speeds for these two surface conditions were $u^* = 1.63$ *m/s* and *1.61 m/s*, respectively. Heated-surface experiments also showed that the two smoother test beds developed a decreasing trend in threshold wind speed, from *30 m/s* at neutral conditions to *8* and *20 m/s*, respectively, at increased surface heating levels. A third bed, $z_o = 0.018$ *mm*, observed the classical rough-wall "law-of-the-wall" trend. This rougher test surface, however, portrayed the opposite effect, where threshold increased for greater instability conditions. The major difference between the first two smooth beds and this rougher bed was the application of conductive roughness elements (steel nuts), which initially caused a lower threshold value of $u^* = 0.77$ *m/s* at neutral conditions, but then increased with higher surface heating. This latter result should be viewed as preliminary.

Table of Contents

Nomenclature

Symbol	Description	Units
C_z	correction to flattened Pitot tube due to velocity gradient effects	**
C_p	flattened Pitot tube coefficient of pressure	**
D	outer height of flattened Pitot tube	mm
d	inner height of flattened Pitot tube	mm
g	gravitational acceleration	m/s^2
P_c	measured chamber pressure	mb
P_T	pressure at temperature, T	Pa
P_o	surface pressure	Pa
ΔP	differential pressure	Pa
r	mixing ratio of water vapor mass to dry air mass	**
Ri	Richardson number	**
Ri_B	bulk Richardson number	**
Ri_G	gradient Richardson number	**
T	measured wind tunnel temperature	°C
U	measured wind tunnel velocity	m/s
$U(z)$	corresponding wind tunnel velocity at local height, z	m/s
U_c	corrected flattened Pitot tube velocity due to viscous effects	m/s
u^*	friction velocity	m/s
z	local height	mm
z_o	roughness height	mm
$\bar{z}$	geometric mean height between top of boundary layer to surface	mm
γ	specific heat ratio	**
ρ	density	kg/m^3
θ	potential temperature	°C
θ_v	virtual potential temperature	°C
μ	dynamic viscosity	kg/m s
ν	kinematic viscosity	m^2/s

** dimensionless

Chapter 1: Introduction

This wind tunnel study focuses on the threshold or initial movement of Aeolian-blown dust observed in a low-pressure environment and subjected to not only neutrally-stratified but also various levels of unstable atmospheric boundary-layer conditions. Low-pressure conditions for the investigation were primarily pre-set similarly to the surface of Mars. Thus, experiments were conducted at the Martian Surface Wind Tunnel (MARSWIT) located at NASA Ames Research Center, Moffett Field, California. A surrogate dust of *1–2* μm sized particles, made of a material commonly known as Carbondale Red Clay (CRC), was used as the only transport media released from the wind tunnel floor. CRC dust was chosen for this study primarily for its similarities in density and aerodynamic size to dust in the Martian atmosphere as observed by spacecraft orbital and lander missions.

Dust threshold experimental techniques included a preparation of aerodynamically settled CRC-dust onto the wind tunnel floor one day prior to the actual test. A low-pressure experimental run consisted first of an initial setting of the sub-surface heating conditions to the desired stability level and then by engaging the wind tunnel speed while continuously measuring the freestream speed and temperature, the surface temperature profile, and the signals from a particle impactor probe. Once the impactor probe detected dust movement, corresponding wind tunnel threshold conditions were extracted from the various simultaneous measurements.

Procedures also included separate experimental runs of boundary layer surveys, which specifically included the acquisition of wind profiles at neutral stability conditions.

These wind profiles were primarily used to analyze the flow quality of the boundary layer turbulence in the wind tunnel test section so that a valid prediction of surface shear can be determined at dust threshold. Two sets of roughness conditions were also arranged: a smooth bed of 32-grit sandpaper and a second rougher bed consisting of the 32-grit sandpaper plus a pre-determined pattern of one-half inch tall steel nuts. Preliminary trials of extreme subsurface heating resulted to a rippling of the sandpaper for the first test surface condition. Dust threshold and boundary layer survey experiments were made over the rippled sandpaper. After a reconditioning of the sandpaper, a much smoother surface was generated, over which experiments were also conducted. In all, three roughness conditions were simulated in the wind tunnel.

The primary objective of this wind tunnel investigation is to determine the effect of an unstable surface condition on the threshold of dust only over a given surface roughness. Theoretically, under neutral stability, the threshold speed that a loose surface-particle aerodynamically releases from the ground decreases for smaller particles until an optimum particle size is reached. In other words, larger particles tend to be more dense and heavier than smaller particles, thus requiring higher wind shear for transport. According to Bagnold (1941), a change in the threshold trend occurs at the optimum particle size of about $80\ \mu m$. From this size diameter, the threshold speed begins to increase for much smaller particles, thus needing faster winds sometimes faster than that required by much larger particles. Since such a condition was determined over a uniform-size bed of particles, such a phenomenon was apparently due to the change in turbulent flow patterns within the turbulent boundary layer from rough-wall flow to hydraulically smooth-wall flow.

Consequently, the investigators in this study are attempting to prove that by heating the surface, thereby increasing the buoyancy of the airflow near the surface, there is a potential for dust-size particles to move at much lower threshold speeds. Hence, threshold would be a function not only of size and surface roughness but also of boundary-layer stability conditions. Little is known about the effects of an unstable atmosphere on the threshold of dust. Field observations can only theorize on its outcomes, since other entrainment mechanisms are generally present. Direct numerical modeling of the atmosphere, on the other hand, can isolate the conditions and provide accurate simulations, but is limited to the capabilities and the accuracy of computer calculations. Thus, a controlled experiment is necessary to compliment the results from both visual observations and numerical models. In the present study, wind tunnel experiments were conducted to measure dust threshold under unstable atmospheric conditions. Here, solar radiation heating was emulated using heated plates along the wind tunnel test bed. Perhaps the most interesting case is the unstable atmosphere developed by the accumulation of surface heating from solar radiation during a late Martian afternoon. The presence of an unstable atmosphere may explain the spacecraft observations of Martian dust storms initiating at lower geostrophic wind speeds than previously estimated. The investigation described in this report will primarily focus on dust threshold findings from a Mars-simulated surface in a low-pressure wind tunnel under neutral to unstable stability conditions.

Chapter 2: Background

2.1 Aeolian Dust

Particles in the atmosphere can appear in various shapes and chemical compositions. Once suspended into the air, they are categorized as aerosols. By definition, an aerosol is the suspension of particles within a gas medium. Atmospheric particles can measure from as small as 10^{-3} μm in diameter up to as large as 100 μm in diameter. In general, atmospheric particle size-distributions fall into two ranges: fine, which possess diameters less than 2.5 μm, and coarse, which are 2.5 μm or greater in diameter [Seinfeld and Pandis (1998)]. The fine-particle range is divided into two distinct modes: a nuclei mode and an accumulation mode. Representing the smallest sizes, the nuclei mode is primarily comprised of particles generated from condensed hot vapors released from combustion processes and from the nucleation of atmospheric gases. Particles in the accumulation mode are the result from the coagulation of particles in the nuclei mode and from the growth of nuclei matter by vapor condensation. Coarse particles are specifically mechanically emitted solid matter originating from either natural or man-generated sources, and are the primary size elements that form a dust cloud.

Dust is considered as a type of aerosol, consisting of primarily solid, coarse-size particles, commonly known as “particulate matter”. It primarily originates from arid and semi-arid regions where there are abundant sources of bare, loose and mobile sediments [Middleton (1997)]. According to most terrestrial researchers, aeolian dust contains particle diameters of less than 62.5 μm. Of this size range, suspended dust particles larger than 20 μm in diameter tend to quickly settle back to the ground as the intensity of

atmospheric turbulence decreases. Particles, smaller than *10* μm, can transport to great distances and can remain suspended in the Earth's atmosphere for several weeks [Pye (1987)]. When ideal conditions are met, regional sand and dust storms such as those that occur over the Saharan Desert can prompt long-term dust suspension. Such storms have the intensity to not only damage the environment but also reduce the local and even regional visibility. Dust suspended into higher atmospheres also can contribute towards global climate changes.

Dust particles are not as small as gas-phase aerosols, which are abundantly released into the upper atmosphere by thermodynamic and chemical interactions. They also are not as large as coarse-size particles, such as sand, which are commonly transported near the surface by aeolian saltation and deposition. However, dust particles are light-weighted solid material, which have the potential for prolonged suspension into the upper atmospheres similar to the nature of aerosols, yet also contribute to the changes in surface features by deposition similar the actions of course materials. By understanding the nature of aeolian dust, dust control mechanisms can be developed to minimize the effect of environmental dust hazards. Since a typical dust cloud can dissipate quickly into the atmosphere, it can be easily misconceived as merely a nuisance. In reality, most dust compositions pose to be environmental health hazards. For example, coal-mining dust is primarily known to cause "Black Lung Disease". Dust storms originating from Owen's Dry Lake, California have been suspected to transport health hazardous elements into the populated regions of Southern California. Since dust falls in the micron size-range, it can be easily inhaled and settled into sensitive regions of the human pulmonary system [Reible (1999)].

2.2 Aeolian Processes

Dynamic atmospheres are constantly supplied by a flux of surface dust. On Earth, airborne particles can originate not only from natural sources, such as sea spray, volcanic eruptions, or wind erosion, but also from anthropogenic activities, such as industrial combustion, vehicle transportation, or farming. In populated regions, ground sediments can be redistributed over the surface primarily by human activity such as vehicle travel, farming or industrial processes. Without the presence of man-made disturbances, one of the most effective sediment-transport processes in dry-desert regions is the landscaping effect of aeolian winds. The term "aeolian" originates from the name of the Greek god of the winds, *Aeoli*. Aeolian winds result from the interaction between atmospheric turbulent flow and variable surface features forming the atmospheric boundary layer. Dust naturally emitted into the atmosphere is categorized as an aeolian process.

Evidence of the presence of aeolian processes can appear in the form of various-types of eroded and deposited surface configurations, such as sand dunes. Aeolian-blown surface features are not only identified on Earth. From spacecraft images, evidence can also be found on Mars, Venus, Titan (one of the moons of Saturn) and Triton (a moon of Neptune). In particular, telescopic observations and spacecraft missions over Mars reveal that the even a planet, possessing a less active surface and atmosphere, is continuously present with aeolian-blown particles [McLaughlin (1954), Kuiper (1957), Sagan and Pollack (1969)].

In general, aeolian processes involve the natural abrasion, deflation, and entrainment of sediments due to the turbulent interaction between the ground and the wind. Abrasion and deflation generally involve the erosive release of sediments from

larger solid materials. Entrainment, on the other hand, is associated with the movement and transport of loose particles. In the course of an aeolian process, particles also can be redistributed over the surface by means saltation, coagulation or suspension. Saltation is the repeating process of a particle being lifted from the ground into a multi-trajectory path until it settles to a downstream location, while coagulation is the event when the traveling particle embeds itself into a surface at the impact from a trajectory. Suspension is the circumstance when the particle lifted from the ground is released into the atmosphere for an extensive duration. Regardless of the particle removal or transport method, the presence of dust in the atmosphere contributes towards the changes in not only visibility but also in the fluid and thermal interactions within the atmosphere. Such changes are of major factors towards global warming and to the health of the surface environment. Thus, there is a need to learn about the movement of dust.

Classical studies of sediment transport were introduced by Bagnold (1941) through the movement of sand. Sand-size grains are generally transported by saltation. As the particles impact the ground, other sediments are then ejected from the surface. If the dispersed grains resume the saltation process, a "saltation cloud" eventually develops within the surface boundary layer. A particle attains "true" saltation when its vertical velocity component becomes less effective against its forward trajectory forcing the particle to advance continuously in the same trajectory [Lancaster and Nickling (1994)]. Bagnold (1941) also defined fluid threshold as the wind speed at which "sand-size" particles initiate saltation and as the condition at which particle flux can be determined.

Dust-size grains, however, are much too small and light to fall into saltation trajectories. Instead, they pass directly into suspension, which has been observed in

terrestrial field observations and several preliminary experiments conducted at the NASA Ames Research Center Martian Surface Wind Tunnel (MARSWIT) facility. A particle becomes suspended when its terminal velocity becomes less than the upward turbulent-eddy velocity [Bagnold (1941)]. "True" suspension occurs when the particle remains in the atmosphere and travels to greater altitudes and distant locations. Accordingly, a suspension threshold is defined and measured, and "dust flux" is estimated based on the amount of material removed from the surface.

2.3 Dust Entrainment Mechanisms

There have been several studies pertaining to the primary mechanisms that release dust into atmospheric suspension. On Earth, several observations have indicated dust emissions are commonly induced by sand saltation impacts. On the other hand, wind tunnel investigations, simulating the surface of Mars, have revealed that dust entrainment occurs even at wind speeds below sand threshold [Greeley *et al*. (1980), Iversen and White (1982), Greeley and Iversen (1985), and White *et al*. (1997)]. Thus, dust emissions could be solely induced by mechanisms that enhance atmospheric turbulence near the surface. One such mechanism is the presence of an unstable boundary layer.

2.3.1 Dust Entrainment Due to Saltation Impacts

In most cases, impacts from saltating sand grains are required in order to remove dust particles from the surface. Over rough surfaces, large obstructions such as rocks or pebbles can shelter the exposed dust from aeolian transport or even restrain the dust material by surface cohesion. In order to release the constrained dust particles, the surface

must be disturbed by a bombardment of saltating sand. Dust also can be protected from the wind even over regions consisting of a combined soil mixture of dust and sand particles. Under a calm, dry atmosphere, gravity allows extremely small particles to sift between larger particles. As time goes by, the soil is divided so that a top layer of sand-size grains is exposed to the atmosphere sheltering the dust particles in the lower layers.

To release the dust, sand saltation must be first initiated so that the dust is readily exposed to particle collisions. Field observations indicate that surface impacts from the return trajectories not only eject other sand-size grains but also disperse dust particles beyond the boundaries of the saltation layer and into the atmosphere. Thus, over most terrestrial surface conditions, impacts from saltating particles are the primary mechanism for dust entrainment [Middleton (1997)]. One major condition that must exist in order to accept saltation impact as the primary dust-emission mechanism is that wind speeds must be strong enough to initiate sand saltation. In order for saltation to occur, highly turbulent winds are required in order to develop the necessary surface shear for lifting sand-size particles.

2.3.2 Dust Entrainment Due to Direct Wind Exposure

Loose ground sediments directly exposed to the atmosphere can be entrained simply by the aerodynamic forces caused by aeolian winds. Although all atmospheric particles vary in shape and size, the basic aerodynamics around a typical particle generally can be described based on the flow around a sphere. At rest, a surface particle feels only the force of gravity, the pressure force from the atmosphere, and a normal friction-force from the ground. When subjected to airflow, the particle induces

resistances against the force of the wind. First, a "surface-friction" drag is applied to resist a horizontal slip between the particle and the ground. Second, the particle's shape applies a "form" drag, directing the wind to flow around the particle surface. Finally, this flow diversion also generates a skin-friction drag between the wind flow and the particle's outer surface. Since the particle is initially at rest on the ground, the wind is restricted to flow above the particle generating a low-pressure region over the exposed curved upper-surface. Once a critical pressure differential between the particle's upper and surrounding surface is reached, a suction force or aerodynamic-lift force is produced to resist the hold of gravity and to eject the particle from the ground.

The critical wind speed at which a particle is lifted from the ground denotes its threshold for initial entrainment. Thus, threshold is defined as the velocity at which sediments are aeolian-entrained from the surface. Early sediment-transport publications defined particle threshold as the velocity at which "sand-size" particles begin to saltate. Since dust-size particles are driven immediately into suspension without the process of saltation, dust threshold is identified as the velocity at which dust is ejected from the surface. If the vertical velocities of the turbulent eddies in the atmosphere are greater than the settling speeds of the entrained media, smaller particles can potentially be driven directly into long-term air transport or "true suspension".

2.4 Observations of Dust Suspension

Spacecraft missions on Mars have shown that dust suspension can occur even in the absence of saltation impacts, suggesting that dust can be suspended solely by the aerodynamic lift generated as wind flows over a particle. In this case, dust movement is

highly dependent on surface terrain roughness and atmospheric conditions. From the first telescopic and spacecraft observations, aeolian processes have been known to be present on Mars including the occurrence of seasonal dust storms. Based on surface albedo changes imaged by the early *Mariner* series spacecraft missions, early researchers also estimated that the Martian atmosphere possesses extremely low pressures implying that the frictional drag between the Martian surface and the air is much lower than what is found on Earth [Arvidson, R.E. (1972), Arvidson, R.E. (1973), Sagan (1973)]. Accordingly, researchers suggested that extremely high wind speeds must occur on the surface of Mars in order to develop the aerodynamic lift necessary for sediment transport.

This theory of high winds later was refuted by the intricate analysis of the great Martian global dust storm captured by the *Mariner 9* spacecraft mission. *Mariner 9* not only provided the first regional photos of the surface of Mars, but it also performed orbital measurements of surface pressures, temperatures and wind speeds. Although slightly higher values were previously estimated, the spacecraft confirmed the presence of a low-pressure atmosphere over Mars. The most puzzling discovery was that wind speeds were measured to be much lower than what is expected for a low-pressure environment. Thus, new theories were suggested towards aeolian sediment entrainment over Mars. According to various field and wind tunnel studies, a greater amount of aeolian activity was found to initiate more quickly under conditions of high surface heating under a cool atmosphere, hence atmospheric instability.

Unstable atmospheric conditions are typically produced during the mid-daytime period and the near-surface, mid-latitude locations of Mars. Based on the results from the *Mars Pathfinder Lander (MPL)*, temperature fluctuations reached as high as *15-20°K*

during the afternoon where the surface was hotter than the atmosphere. Acquired data showed also that the mean surface pressure was found to be *6.75 mb*. Thus, simulations in MARSWIT were conducted at *10-mb* atmospheric pressure using air, which agrees with a dynamically similar environment of *6.5 mb* in a Mars carbon dioxide (CO_2) atmosphere. Unstable surface conditions were selected based on the negative temperature gradients recorded by *MPL* during the mid-afternoon to early evening Mars period. According to other missions, evidence of highly active dust suspension during this part of the Mars daytime hours was recorded. More recently, results from the analysis of the windsock instruments on *MPL* revealed that the landing site represents an aerodynamic roughness height of *3 cm* and friction speeds of *1 m/s* [Sullivan *et al.* (2000)]. In addition to wind and atmospheric measurements, MPL also captured a variety of aeolian activities along the surface including the presence of "dust devils" which were thought to be another mechanism for the suspension of dust. The current "dust devil" observations and measurements will later be investigated in future sediment transport projects.

2.5 Previous Experimental Studies on Particle Threshold

Experimental measurements of the threshold for various particles sizes were first pioneered by Bagnold (1941). A graph of the measured threshold as a function of particle size indicated that the required threshold decreases from the largest particles until reaching a minimum threshold value at an optimum particle size of approximately *80* μm. From this critical value, the required threshold speed sharply increases for smaller particle sizes. Later verified by other researchers, this initial trend in particle threshold

has proven to be fundamental standard. As the particle becomes exceptionally large, its mass increases, thus, higher threshold speeds are expected.

In regards to the increased threshold trend for extremely small particles, Bagnold suggested that it is driven by the change in surface roughness formed by the surface distribution of each particle size. With a uniform layer of fine-sized particles, the near-surface wind encounters an "aerodynamically smooth" surface, which induces a weaker skin-friction drag over the layer allowing the wind to slip much easier over the surface. Consequently, the chance of aerodynamic-lift generation between the wind and a single particle is reduced. In order to lift the fine-size particles, faster wind speeds are required to generate greater skin-friction drag. As the surface roughness increases with the increase in size, particles become much easily entrained signifying an "aerodynamically rough" surface.

Greeley *et al*. (1980) analyzed and compiled various MARSWIT test results and concluded that threshold velocities for saltating particles increase for lower ambient pressures and is further enhanced when the atmosphere becomes unstable (see Figure 2.1). From a recent wind tunnel study, White *et al*. (1997) determined that at neutral conditions under Mars-simulated pressure, dust particles pass directly and immediately into suspension without partaking in the process of saltation. In the presence of an unstable atmosphere where the surface air mass is warmer than the surrounding air, there is a greater potential for enhanced vertical turbulence mixing in the near-surface resulting in increased levels of surface stress. This increase in surface stress due solely to unstable conditions may provide the necessary mechanism to exceed dust threshold required under

neutral conditions. Thus, dust injection into the atmosphere can be attained at lower geostrophic speeds.

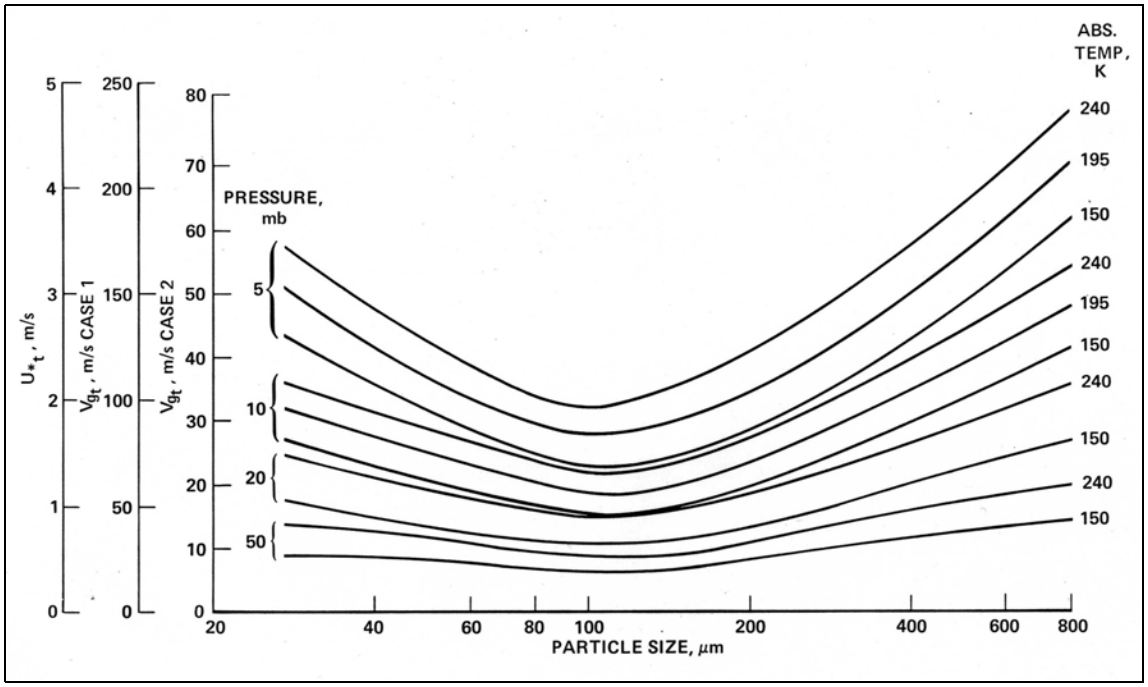

Figure 2.1: Compiled MARSWIT results of the threshold behavior for a range of particle sizes at various pressure and temperature conditions.

MARSWIT studies by White *et al.* (1997) suggested two general guidelines towards the improved methods in Mars Aeolian dust threshold simulations. Based on spectral and presumed aerodynamic properties, finely ground Carbondale Red Clay (CRC) material was identified as a suitable surrogate Mars dust for simulations of aeolian processes. White *et al.* (1997) also experimented with several methods of surface emplacement for the CRC dust (see Figure 2.2). By process of elimination, undisturbed aerodynamic settling of suspended dust generated the best simulation of an aeolian surface distribution of dust. Thus, CRC dust and the aerodynamic settling procedures were used during the dust threshold experiments presented in this report.

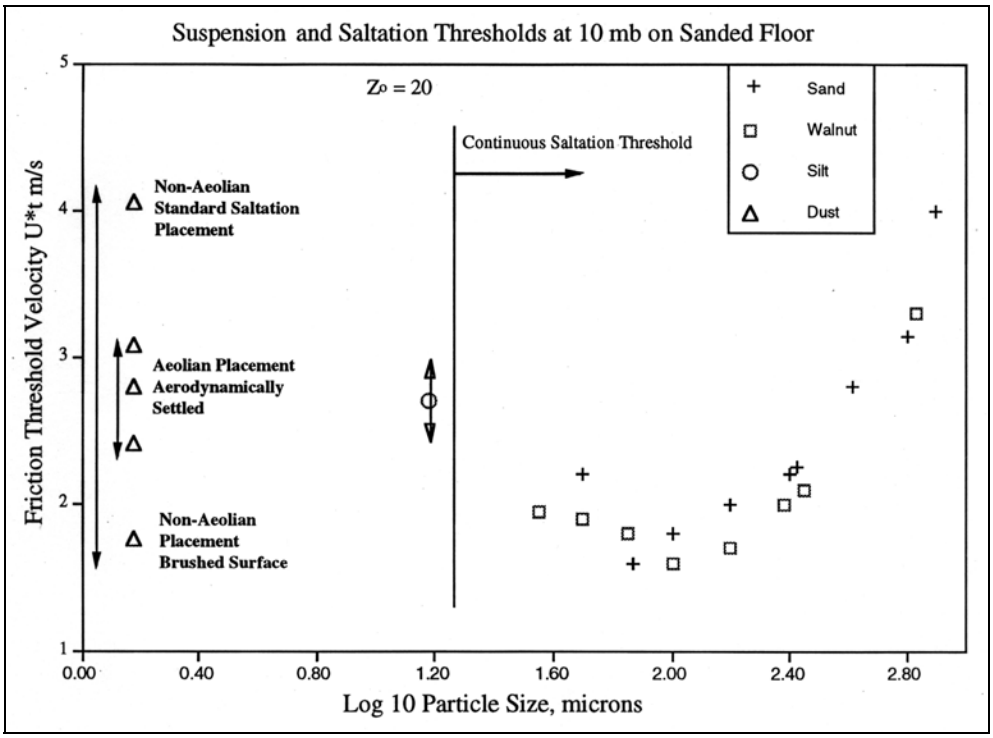

Figure 2.2: Comparison of measured threshold velocities for various dust emplacement methods from White *et al.* (1998).

2.6 Atmospheric Boundary-Layer Flow

In order to transport dust or any other solid particles from the surface, boundary layer turbulence must be generated in the atmosphere by aeolian winds. Length and time scales in the full-scale atmosphere accordingly characterize the existence of a fully turbulent, rough-wall, boundary layer flow. Thus, under neutrally stratified conditions, near surface wind profiles may be described by the classical "law-of-the-wall" solution, defined as follows [Prandtl (1925)].

$$U(z) = \frac{u^*}{k} ln\left(\frac{z}{z_0}\right) \tag{2.2.1}$$

Here, k is the Von Kármán constant, z is the local height above the surface, $U(z)$ is the corresponding local velocity at height z, z_o is the roughness height, and u^* is friction

velocity. Current near surface turbulent boundary layer solutions ("law-of-the-wall") are limited to identify parameters for only neutrally stratified wall-shear flows.

Under neutrally stratified, rough wall turbulence, z_o and u^* in the "law-of-the-wall" equation generally provide sufficient information in describing the turbulent conditions in which a particle reaches a threshold of movement. In wind tunnel studies, however, care must be noted in the setting of the surface roughness elements. Due to a short upwind fetch, particularly in MARSWIT, the facility used for the experiments in this study, there are possibilities that the boundary layer has not turbulently fully developed, or that a turbulent boundary layer did develop but is hydraulically smooth-wall flow and not rough wall flow. In MARSWIT, the only method of determining the configuration of roughness is by trial-and-error based on experiments previously conducted. In which case, a more advanced and in-depth boundary layer profile analysis is required.

2.7 Effects of Stability of Atmospheric Turbulence Flow

In addition to the effects of surface roughness, aeolian processes also are influenced by the stability of the atmosphere. A critical factor that determines the type of motion a particle exercises and invalidates the direct use of the "law-of-the-wall" solution is the stability of the atmosphere. Generally, stability is identified by the resulting lapse rates or temperature gradients developed by atmospheric heating during the daytime and cooling at night.

There are three main levels of atmospheric boundary-layer stability: neutral, stable, and unstable. Figure 2.3 displays a schematic of the local eddy configurations for

the three stability cases along with the respective range of the Richardson number, *Ri*, the turbulence parameter that defines the degree of stability. *Ri* represents the ratio of turbulence production due to buoyancy to turbulence production due to mechanical shear.

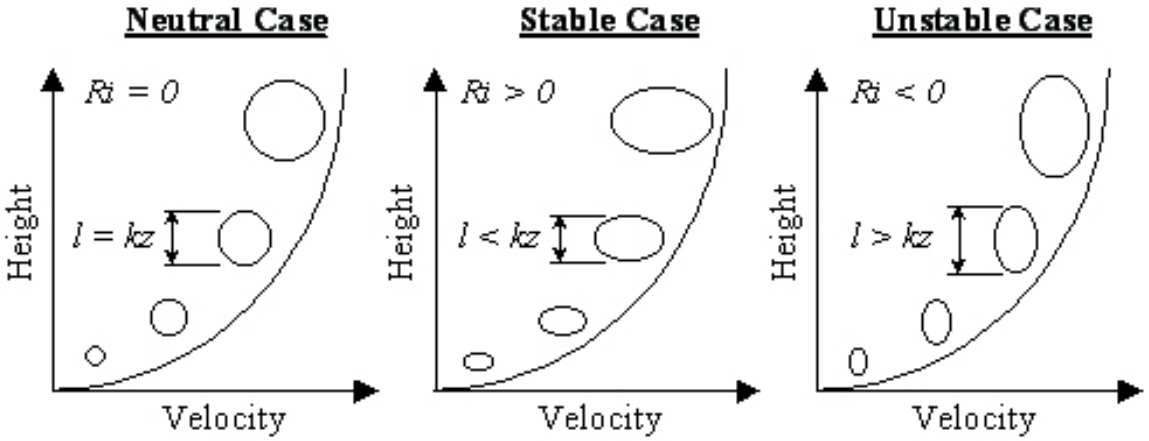

Figure 2.3: General schematic of boundary layer eddy configurations for neutral, stable, and unstable atmospheric conditions.

Neutral stability conditions are present when the temperature changes adiabatically with height within the atmospheric boundary layer. When there is no change in virtual potential temperature with height, density changes with height also are inexistent, thus there is no additional vertical fluid transfer, other than the vertical eddy circulation naturally occurring due to wall shear stress. In which case, the local eddy length scale follows the "mixing-length theory" and is equal to *kz'*, the Von Kármán constant times the local fluctuating velocity, and the velocity profiles and particle thresholds or particle take-off speeds can be associated directly with the "law-of-the-wall" solution.

Stable atmospheric conditions are generally present at night or during the early morning hours, in which time the surface becomes cooler than the air and the trend of the temperature profile increases with height. In this case, the cooler ground and the cooler air-parcels absorb the warmer air-parcels directly above, thereby suppressing the growth

of shear and buoyancy generated turbulence. Stable cases also are associated with lower levels of surface shear stress. Therefore, in a stable atmosphere particle threshold velocities are higher that those attained under neutral conditions.

When the surface temperature becomes higher than the air temperature, an unstable atmosphere exists. Here, a circulation of rising warm air and falling cool air vertically distorts the turbulent eddies so that vertical wind speeds are greater than lateral wind speeds creating a "lighter" or more buoyant atmosphere. Surface heating inherently causes buoyant stretching of turbulent eddies, thus developing an additional mechanism for turbulence distorting the measurements of the near-surface velocity gradient. In which case, due to the added vertical motions in the flow, buoyancy assumes the dominating force in turbulence production thus providing a greater potential for particle movement to occur at lower wind speeds. An unstable condition is generally evident between the mid-daytime to late afternoon hours when the ground in heated by solar radiation. Buoyancy enhances vertical turbulent mixing thus increasing the overall level of turbulence present in the flow as well as increasing turbulent shear stress. Thus, unstable conditions provide the necessary incremental increase in surface stress to exceed particle threshold developed under neutral conditions.

Wind profiles generated under stable and unstable conditions are typically distorted from the "law-of-the-wall" solution. In order to determine the critical parameters that describe the surface and flow conditions, z_o and u^*, when the only wind profile available is one that was collected at stability conditions other than neutral, an investigator would have to conduct a stability correction procedure, which incorporates an iterative process between the values of Ri and z_o and u^* [Golder (1972)]. Fortunately,

in wind tunnel studies, the experimenter physically sets the stability condition over a test bed. Thus, for any test surface configuration, boundary-layer analysis may be conducted under neutral conditions prior to conducting stable or unstable atmospheres. Thus, for the current wind-tunnel investigation of dust threshold, applying the stability correction procedures were not necessary.

Chapter 3: Experimental Facility and Setup

For the current study, unstable boundary layer experiments were conducted in the NASA Ames Research Center Martian Surface Wind Tunnel (MARSWIT), which is housed inside a sealed chamber capable of sustaining the near vacuum pressures characteristic of the surface of Mars. Due to uncontrollable facility constraints, all simulations could only be maintained at about 10-mb air under temperatures ranging *288-310 K*. From the ideal gas law, such conditions are equivalent to a CO_2-rich Martian atmosphere of about *4* to *5 mb* based on an average temperature of *210 K*. According to spacecraft data obtained from the *Viking Lander 1* and *Mars Pathfinder* sites, surface pressures averaged around *6 mb* ± *2* to *3 mb* [Hess et al. (1977), Sutton et al. (1978), Schofield *et al.* (1997), and Golombek *et al*. (1999a)]. Thus, the atmospheric simulations in MARSWIT are comparable to the conditions on the Martian surface. The only other variable that could not be duplicated is Mars gravity, which is *38%* that of Earth. In the next sections of this chapter, a description of the wind tunnel facility is provided followed by a detailed presentation of the experimental setup and conditions.

3.1 Martian Surface Wind Tunnel (MARSWIT) Facility

During the early 1960's, a low-pressure chamber was constructed at NASA Ames Research Center, Moffett Field, California. It was originally used for conducting acoustic and structural tests on rockets at simulated low pressures characterizing high altitude conditions. For such extreme conditions, the low-pressure chamber was designed pentagon-shaped with reinforced concrete walls ranging three to six feet in thickness.

Along the walls inside the chamber are ports of various types of instrumentation and plumbing pass-throughs that extend into an adjacent laboratory control room where tests can be monitored. To accommodate for the rockets, the chamber also was built *30-m* high with a *164-m^2* floor-space totaling to *4058 m^3* in volume. Using a five-stage steam-ejection system, the entire tower can be evacuated to a minimum *3.8-mb* pressure in approximately *45* minutes. Figure 3.1 presents an aerial photograph indicating the location the low-pressure chamber in Building N-242 and the close proximity of the steam-plant facility identified as Building N-234.

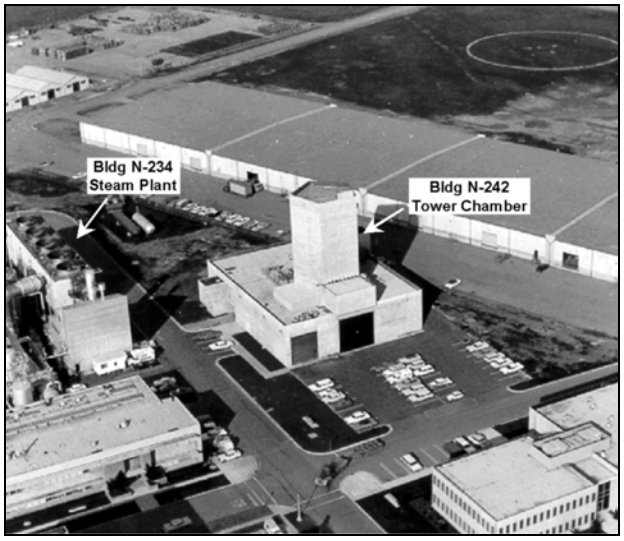

Figure 3.1: Aerial photo of NASA Ames Research Center low-pressure tower facility in Bldg N-242.

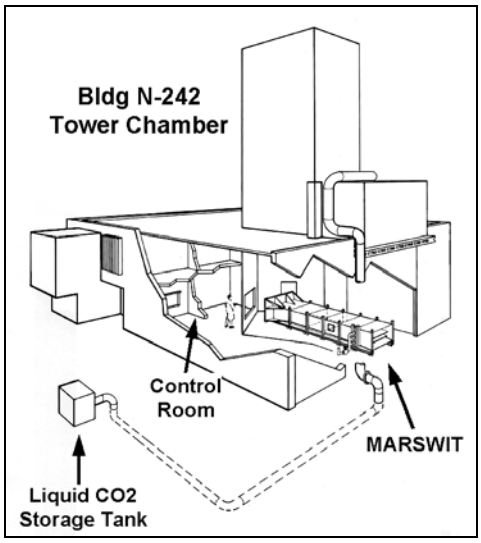

Figure 3.2: Internal schematic of Bldg N-242 tower chamber with MARSWIT facility.

Later, rocket testing was relocated to another facility, and the chamber was vacated. In 1974, the low-pressure chamber was then re-commissioned as the Planetary Aeolian Laboratory introduced with the installation of the Martian Surface Wind Tunnel (MARSWIT) facility. Figure 3.2 above shows a transparent schematic of the tower chamber with a view of how MARSWIT is situated inside. For a closer simulation of the Martian atmosphere, the tower was also outfitted to introduce carbon dioxide (CO_2) into the chamber. MARSWIT was placed at the center of the floor space with its entrance

section facing the window of the control room. Figure 3.3 displays a photograph of the access door leading into the low-pressure chamber with a view of the inlet section of the MARSWIT facility. This *7.6-m* by *7.9-m* access door conveniently permits large experimental apparatus to be placed inside the chamber.

Figure 3.3: View of MARSWIT entrance contraction through the low-pressure chamber access door.

Since the steam plant services several other laboratories, the MARSWIT tower is normally accommodated only three out of five stages of chamber air evacuation. At best, *5-mb* vacuum pressure can be attained. For a decent experimental time window, a sustainable atmosphere is generally limited to about *10-mb* pressure. CO_2 also could be supplied for experiments by first evacuating the existing chamber air to the lowest pressure obtainable. CO_2 then can be pumped into the system monitoring that its outside storage tank does not freeze. Once the chamber volume is filled and pressurized with the desired gas, it must be evacuated to the desired low-pressure condition. Unfortunately, steam plant time usage also was limited to accommodate the preparations for a CO_2 atmosphere for the current study. Thus, experiments in this investigation were restricted to simulated conditions of *10-mb* air.

MARSWIT is a *14-m* long, open-circuit, suction-type atmospheric boundary-layer wind tunnel with a *1.1-m*^{2} by *2.4-m* length test section. Flow in the wind tunnel is first drawn into the inlet contraction section and then through *10-cm* grid flow-straighteners. In order to develop turbulent boundary layer flow, a *5-m* long "fetch" of slightly increasing cross-sectional size with downstream distance is attached upstream from the test section. The frame of the tunnel was constructed out of steel I-beams and wood, while the inlet contraction and the diffuser downwind of the test-section was made from fiberglass. For easy viewing, the "fetch" and test section side and upper walls were installed with *2.4-cm-thick*, clear Plexiglas. Figure 3.4 presents a schematic diagram of the MARSWIT facility.

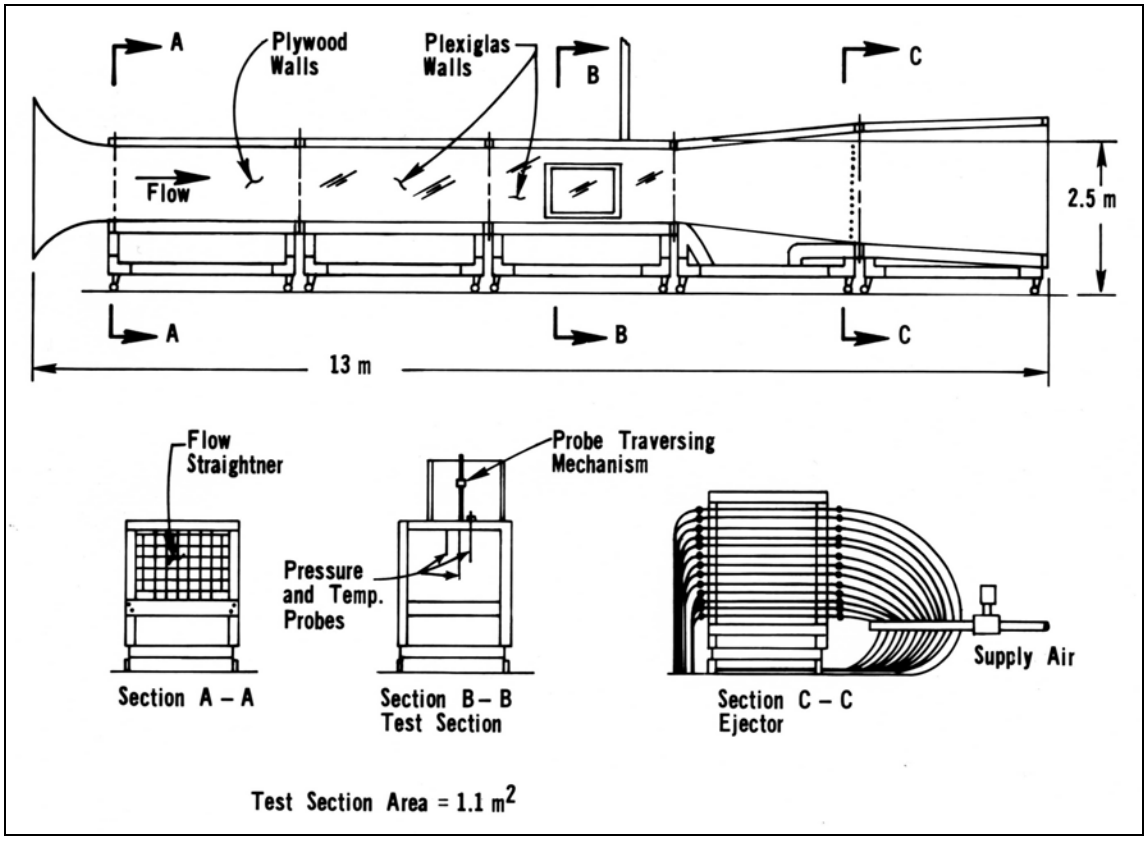

Figure 3.4: Schematic of Martian Surface Wind Tunnel (MARSWIT).

For experiments conducted under Earth conditions, the wind tunnel is operated with 6-blade fan system, which is capable of velocities of up to *12 m/s*. At low pressure, winds are driven by a network-ejector system placed at the diffuser section. This ejector system consists of *72* equally spaced *1.6-mm* nozzles. It releases high-pressure air or CO_2 into the diffuser section to induce a high-velocity, low-pressure region, thus, developing a form of suction through the tunnel. Using the network-ejector system at low pressure, MARSWIT is capable of attaining wind tunnel speeds of up to *180 m/s* at *5-mb* pressure.

Low-pressure tests are remotely monitored from the Planetary Aeolian Laboratory control room, located outside and adjacent to the chamber. Here, experimental data is acquired with a Microsoft Windows based National Instruments LabVIEW data-acquisition system. The system hardware consists of a National Instruments Model AT-MIO-16E-1 12-bit, 16-channel analog to digital (A/D) board. Its channel capabilities also are further expanded by a National Instruments Signal Conditioning Extension for Instrumentation (SCXI) chassis, which contains two multiplexer modules. The first module provides *32* thermocouple channels, while the second offers *16* double-ended or *32* single-ended voltage channels. The LabVIEW software allows the laboratory user freedom to custom design data acquisition programs known as virtual instruments (VIs), which can be as simple as acquiring highly-sampled analog voltage readings from instruments from one of more channels. Using the "block-averaging" technique, a VI also can be rendered to perform near-simultaneous acquisition, viewing, and analysis of experimental variables. In MARSWIT, parameters such as boundary-layer thermal profiles, wind profiles, atmospheric density, pressure, particle impact count, kinetic

energy of particles, concentration of fine particles, and wind velocity are commonly monitored and acquired simultaneously.

3.2 Test Bed Construction

In order simulate the surface heating on Mars, a test-section module was constructed and installed inside MARSWIT. The *2.4-m* length by *1.2-m* width module was built with four *0.4-m* wide and *4.76-mm* thick aluminum plates centered along the full length of the bed. These plates were individually heated by a *0.3-m* by *0.6-m* thin, flexible, silicone-rubber heater (Omega Model SRFG-1224/5). According to the manufacturer's specifications, the heaters were designed to sustain a maximum operating temperature of *232°C*. Each heater was individually controlled in order to maintain uniform heating as the wind flows over the test bed surface.

To ensure that the heat transfer was directed towards the test section atmosphere, two layers of *3.18-mm* thick fiberglass insulation and one layer of *4.76-mm* thick cork insulation were placed below the heaters. The test bed structure itself was built using three layers of *6.35-mm* thick masonite hardboard where the two top layers were segmented to embed the plates, heaters, and insulation into the floor. This construction allowed the aluminum plates to be flushed with the top surface of the Masonite boards. Figure 3.5 displays a top-view schematic diagram of the test-section module, while Figure 3.6 provides a photo of the test bed layers.

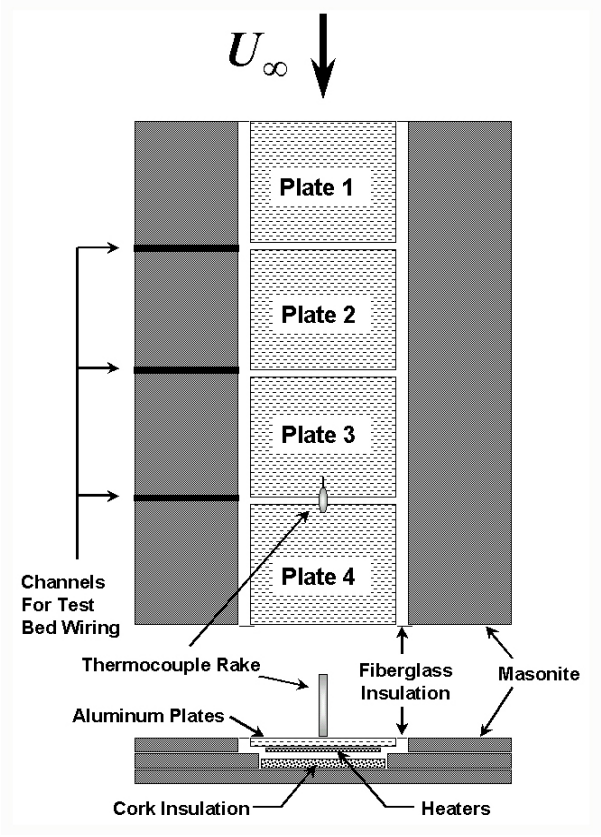

Figure 3.5: Top and end view schematic of the stability experiment test bed.

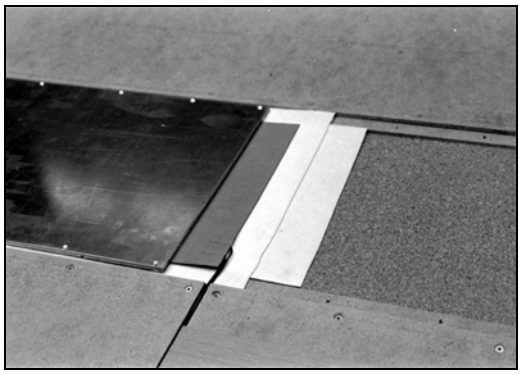

Figure 3.6: Photo of insulation, heater, and aluminum plate arrangement on test bed.

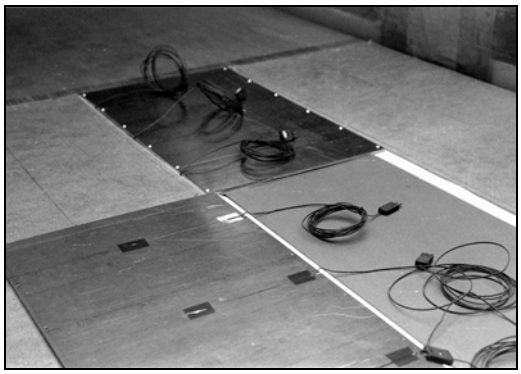

Figure 3.7: Photo of installation of aluminum plates with surface thermocouples.

As shown in Figure 3.7, twelve Type-T thermocouples were used to monitor surface and heater temperatures. In order for the aluminum plates to maintain full surface contact with the heaters, for maximum heating efficiency, channels were milled at the bottom of the plates to accommodate for the thermocouple wire thickness. The sensing end of the thermocouple was then positioned at the lowest surface of the plate and was secured with 3M-brand high-temperature tape. Figure 3.8 presents a schematic of the underside machining of the aluminum plates, and Figure 3.9 displays a photo of a surface thermocouple secured under an aluminum plate. A photo of the final installation of the heated plates with thermocouples beneath is shown in Figure 3.10.

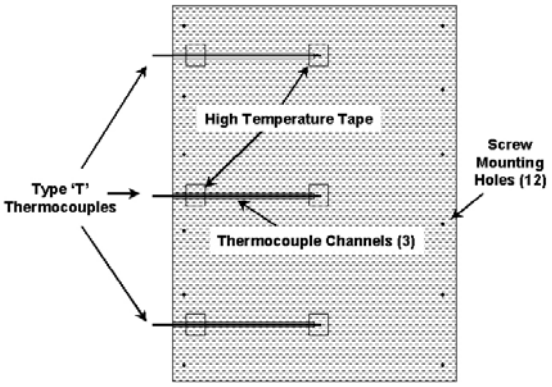

Figure 3.8: Bottom view schematic of thermocouple channels under aluminum plates.

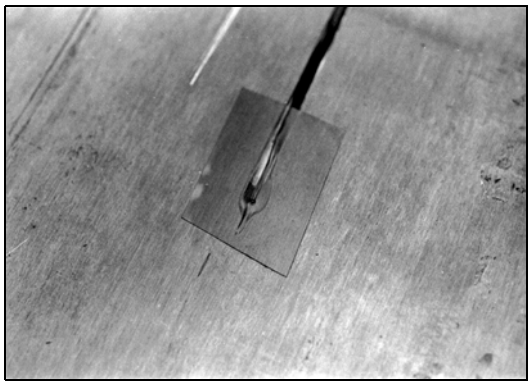

Figure 3.9: Photo of a thermocouple secured inside an aluminum plate channel with high-temperature tape.

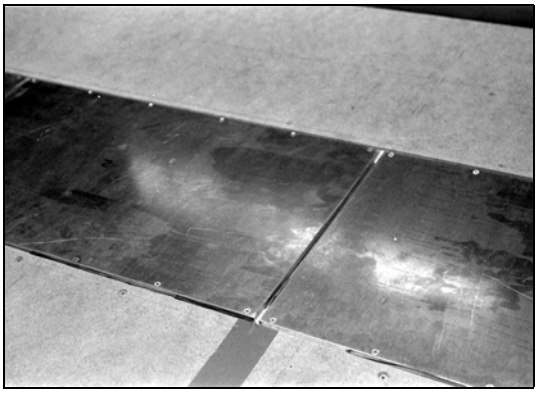

Figure 3.10: Photo of final installation of heated plates.

3.3 Boundary-Layer Fetch Preparation

A naturally turbulent boundary layer occurs inside the tunnel at terrestrial atmospheric pressures. However, at pressures corresponding to the range of Martian surface pressures, boundary-layer "trip" configuration is required at the inlet of the wind tunnel. This is to ensure that a fully developed turbulent boundary layer is developed in the test section. As an initial roughness effect, 3M-brand No. 36-grit sandpaper was flatly secured with heavy-duty double-stick tape along the floor of the entire tunnel, about seven meters long by one meter wide.

Sandpaper material used in the experiment contained tightly spaced synthetic aluminum oxide (Al_2O_3) granules adhered onto thick woven cloth material. According to

DeGarmo *et al.* (1988), the 36-grit classification denotes that the sandpaper roughness would pass though a screen with *36* openings per inch, giving a screen number, *S*, of *36*. The mean particle diameter of the sandpaper granules, D_s, in inches, may then be estimated as $D_s \cong 0.7/S$. Thus, for the 36-grit sandpaper used in the experiment, the mean diameter of a roughness particle is $550\ \mu m$.

Securing the 36-grit sandpaper to the heated plates was problematic and could only be successfully accomplished by using high temperature RTV, manufactured by Accumetric, Inc. Similar to the type used for sealing gaskets in automobile engines, this type of RTV allows the sandpaper to remain attached to the aluminum plates under severe heating conditions. The only drawback is that under low-pressure conditions, it has tendencies to outgas weakening its adhesive properties. By ensuring a clean and proper application of the RTV and roughening the surfaces to be bonded, the adhesive lifetime may be greatly extended. A photo of 36-grit sandpaper installed along the wind-tunnel floor is presented in Figure 3.11.

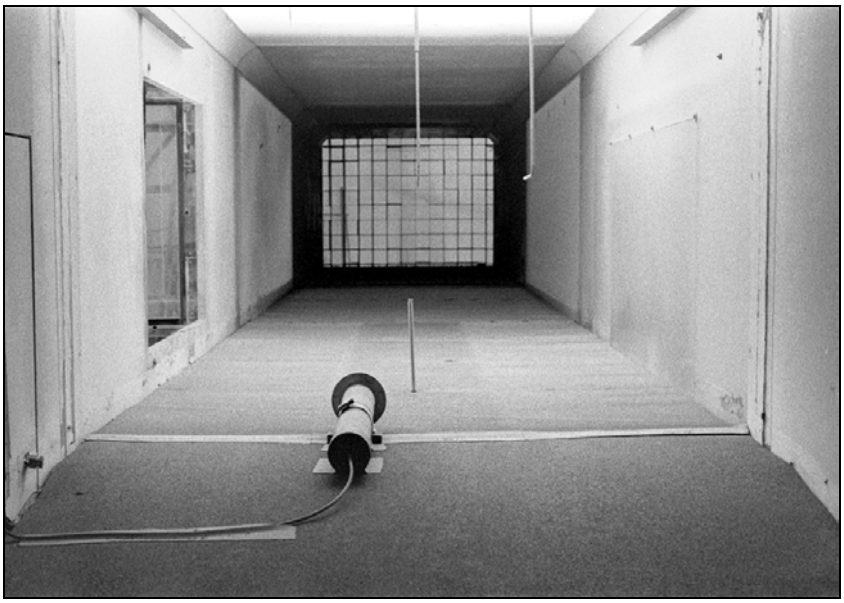

Figure 3.11: Upwind photo of MARSWIT with initial roughness of 36-grit sandpaper installed onto test section and boundary layer fetch surfaces.

Additional “trip” mechanisms were applied to act as surface vortex generators, which consist of small pebbles secured to the tunnel floor. The pebble bed extends approximately *1.2 m* downstream from the entrance section (see Figure 3.12). This technique results into a wind-tunnel boundary layer development that corresponds to a neutrally stratified atmosphere in which the Monin-Obukhov stability length is infinite [White (1981)]. Hence, the ratio of local surface roughness height to the stability length is zero. A finite value of the stability length is achieved in the tunnel by heating or cooling the tunnel floor for unstable or stable stratification, respectively.

Figure 3.12: Downwind photo of MARSWIT displaying pebble boundary-layer trip.

3.4 Instrumentation

For all experiments, Mars ambient pressure was measured using a Tavis pressure transducer, similar to the instrument used with the Viking lander missions. Ambient temperature was monitored using a Type-T thermocouple installed in the wind-tunnel

freestream. Measurements were made to obtain the velocity and temperature profiles at the same downstream location over the test bed. Velocity profiles were acquired using a traversing flattened-tipped Pitot tube connected with a Setra 239 differential-pressure transducer. Temperature profiles were obtained using a thermocouple rake that housed ten Type-T thermocouples logarithmically spaced above the surface to a height of *17 cm*. Figure 3.13 presents the schematic diagram of the thermocouple rake, while Figure 3.14 shows a photo of the rake installed onto the test bed.

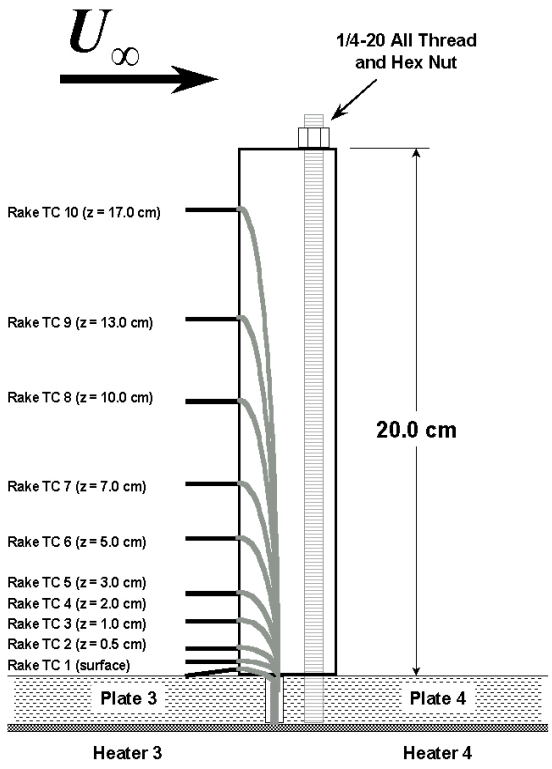

Figure 3.13: Side view schematic of thermocouple boundary layer rake.

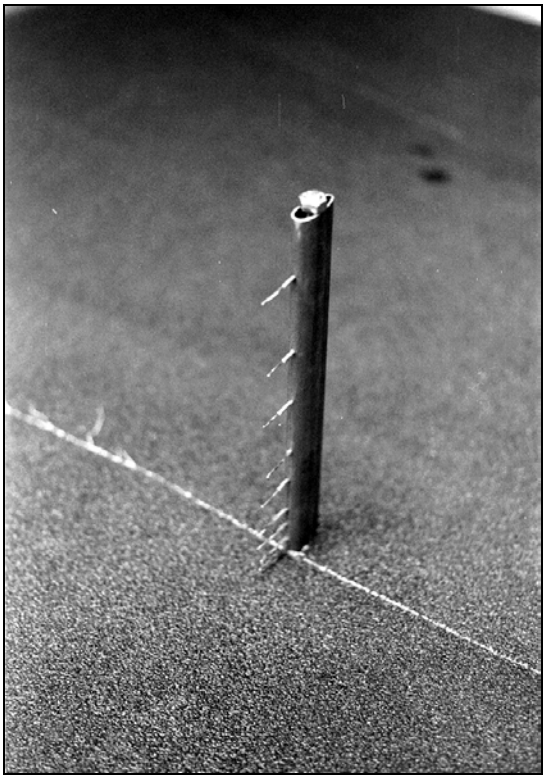

Figure 3.14: Photo of thermocouple rake installed onto test section bed.

To determine dust threshold, an electrostatic particle impact probe was installed at the end of the wind-tunnel test section (see Figure 3.15). This device was connected to a Keithley Instruments Electrometer Model 602 that indicated dust suspension by measuring the electrical charge developed around the face of the probe. The electrometer does not necessarily measure the strength of the impact, however with great sensitivity,

does detect the presence of dust in the air stream. This instrument provides accurate and repeatable dust-threshold measurements.

Figure 3.15: Photo of electrometer probe situated at the end of the test section and slightly offset from the thermocouple rake.

With a LabVIEW data-acquisition system simultaneously collecting and recording all measurement signals, the electrometer's readings can be matched with the velocities acquired from the Pitot-static tube. Thus, the time of dust threshold can be determined and traced to a corresponding threshold wind speed. For the boundary-layer profiles, data were collected from *21* instruments at a sampling rate of *150 Hz* for *120* seconds. Averaging *50* samples at a time from each measurement, this acquisition setup provided *360* averaged data sets of the different measurements. During the dust threshold tests, a sampling rate of *100 Hz* was applied while averaging *50* samples at a time for *600* seconds. Therefore, *1200* averaged data sets were collected containing information on dust threshold and for two separately measured velocity profiles, which were then averaged to produce a single profile. This profile then was used to measure the test bed condition. Figures 3.16 and 3.17 display a sample LabVIEW front panel from one of the experiments and a sample LabVIEW diagram, respectively.

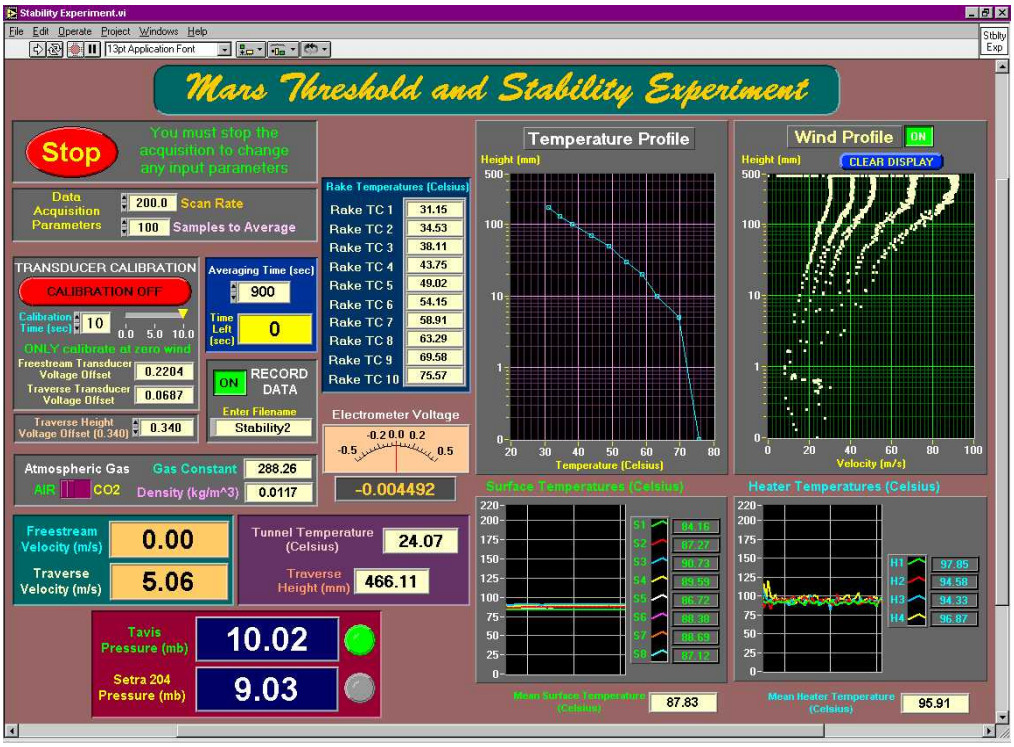

Figure 3.16: Sample LabVIEW front panel display from one experimental run.

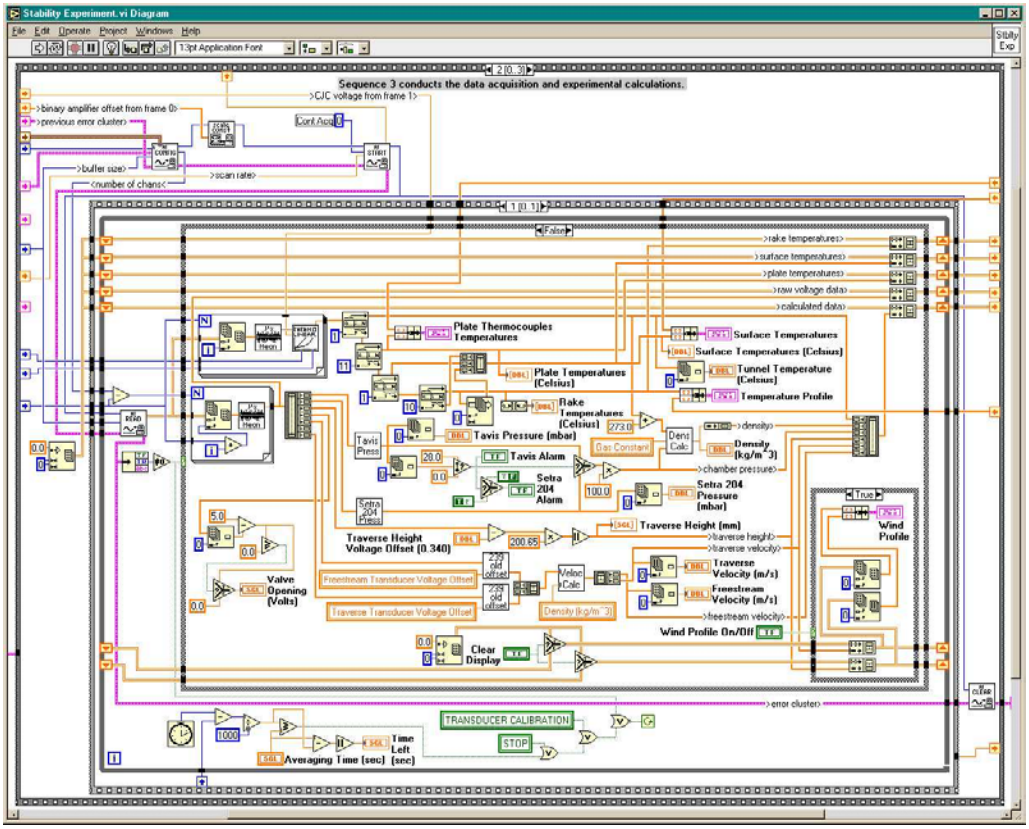

Figure 3.17: Sample LabVIEW wire diagram displaying steps of the data acquisition and near real-time calculations of wind tunnel measured variables.

3.5 Aerodynamic Dust Deposition

For the dust threshold experiments conducted in this study, a material commonly known as Carbondale Red Clay (CRC) dust was used as an accepted surrogate Martian dust [White *et al*. (1997)]. Carbondale Red Clay (Al_2O_3-$2SiO_2$) is a dark or light red colored man-made compound that falls under the alumina silicate chemical family. In dust form (*1* to *2* μm in diameter), it has a typical specific gravity of *2.35*. To create a dust-covered surface, an emplacement method of aerodynamic settling was developed following the method described in White *et al*. (1997). This ensured that CRC dust was applied uniformly over the test bed. It is critical that the method be able to imitate atmospheric particle deposition without imposing unnatural disturbances. In order to develop a continuous "fetch" of particle movement, CRC dust was settled not only over the test bed, but also over the full length of the wind-tunnel floor. This excludes the entrance boundary layer "trips" which covered one to two meters in length. The result from this procedure is a top layer of dust similar to that of a natural aeolian deposition process. This dust layer is presumed to occur on Mars after the settling of airborne particles.

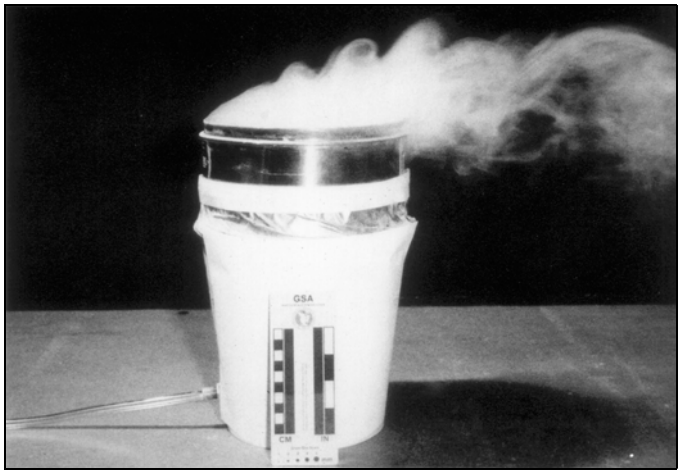

Figure 3.18: Photo of CRC dust being suspended into the air by being pneumatically agitated inside a filtered container.

Aerodynamic dust settling was performed at standard terrestrial atmospheric pressures. This process involves two *4-liter* containers each approximately holding a *1:5* mixture of CRC dust and sand particles, respectively. Figure 3.18 above shows a sample setup of dust suspension method. The containers were covered with a fine mesh screen and placed on top of the downstream section of the entrance boundary-layer trips. With Teflon tubing connected from a compressed air line and into the bottom of the containers, air was injected into the containers allowing the CRC dust to diffuse out of the screen. The larger and heavier sand particles combined with the dust were primarily used to loosen individual dust particles from cohesion and to mix and suspend dust before exiting the container. Initially, due to the weight of the sand, the air-injection tube would become obstructed. This was avoided by tilting the containers downwind and slightly rotating the air injection nozzle so that less weight is imposed onto the compressed-air tube. Therefore, dust and sand were easily circulated and mixed, thus developing a continuous diffusion of dust into the interior of the wind tunnel.

Figure 3.19: Photo of experimenter prepping the dust suspension system just at the end of the pebble-bed boundary layer trip.

As the dust travels by suspension into the air, the wind-tunnel fan system was engaged at a low speed (a few cm/s). Figure 3.19 above shows the wind tunnel preparation of the dust suspension system. This allowed the airborne dust to slowly travel

downstream and to simultaneously settle onto the wind-tunnel floor. After a minimum of four to eight hours of continuous air injection and dust suspension, most of the dust was expelled from the containers. The compressed air and the wind-tunnel fan were disengaged so that the remaining particles in the air are allowed to settle over the surface. Complete dust deposition took approximately *12* hours per test. As a result, this tedious process formed a uniformly distributed and relatively "thick" layer of dust onto the wind-tunnel floor (about *0.5-mm* thick). An additional advantage of this aerodynamic settling technique is that it also allows the dust to become negatively charged which is a common occurrence with terrestrial dust and presumably on Mars [Desch, S.J. and G.R. Wilson (1997)].

3.6 Test Conditions

All experiments were conducted at 10 mb air pressure, which is equivalent to *4* to *5* mb Mars surface atmospheric conditions. Stability levels were set according to amount of voltage that can be applied to each silicone heater, which ranged from *0* to *120* volts. Two roughness conditions were tested. The first consisted of just the base roughness used on the immediate upwind "fetch", which is the 36-grit sandpaper (see Figures 3.20 through 3.22).

The second test surface included an additional bed of a pre-determined pattern of one-half inch tall steel nuts placed on top of the "fetch" and test section sandpaper beds (see Figures 3.23 thru 3.25). Here, each downwind row of nuts were spaced approximately *9.5 cm* apart, where each nut was separated at about *9.5 cm* apart. Each row also was set staggered from the previous row (see Figure 3.26).

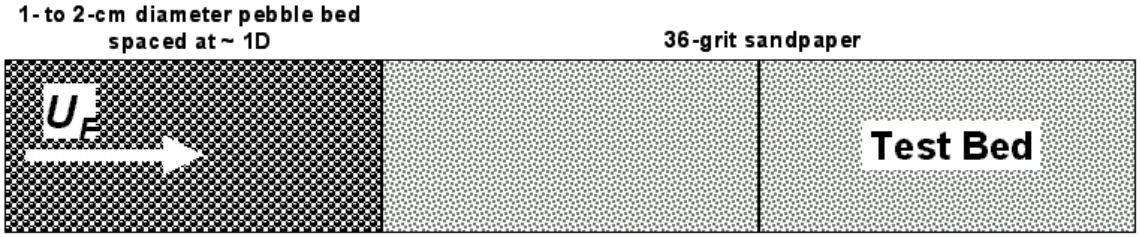

Figure 3.20: Top view schematic of first roughness configuration.

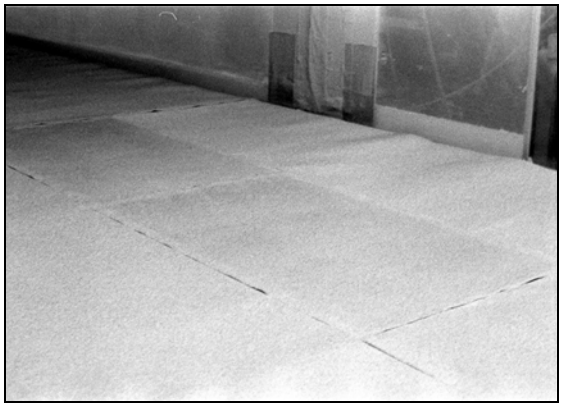

Figure 3.21: Upwind view of test bed and immediate upwind fetch for first roughness configuration.

Figure 3.22: Test section view of first roughness configuration.

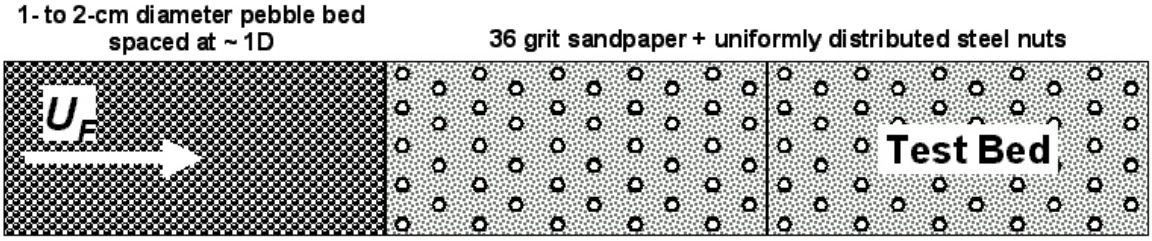

Figure 3.23: Top view schematic of second roughness configuration.

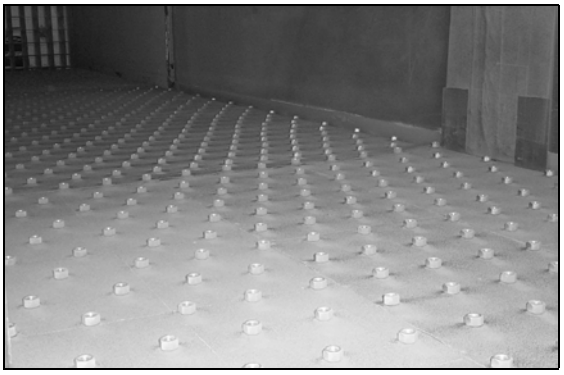

Figure 3.24: Upwind view of test bed and immediate fetch for second roughness condition.

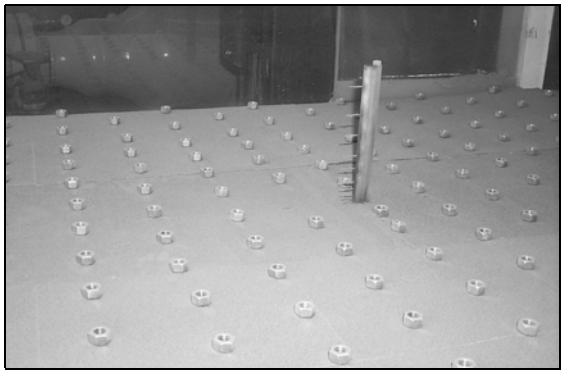

Figure 3.25: Test section view of second roughness configuration.

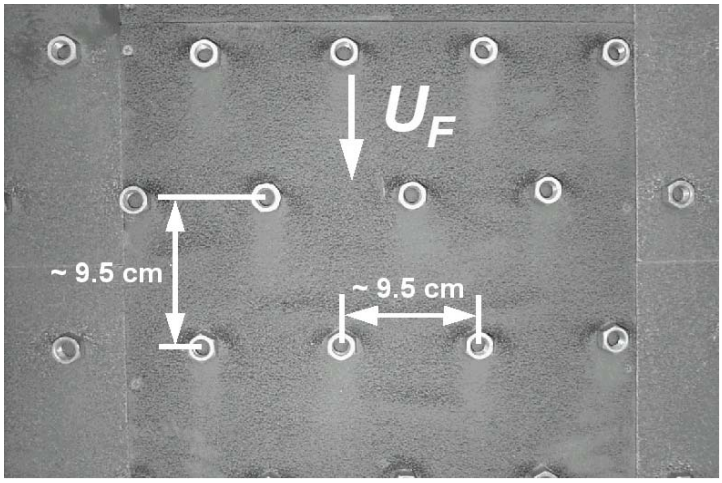

Figure 3.26: Top view of nuts pattern over sandpaper bed.

In the initial planning stage of the project, one sandpaper roughness condition was to be tested. The very first test bed constructed was generally used for preliminary determination of heating level capacity and low-pressure effects on the sandpaper RTV adhesive. After several low pressure and heating trials, the sandpaper began to delaminate and ripple over the heated plates resulting to another level of roughness. Due to a reconditioning of the sandpaper over the aluminum plates, a much smoother surface was achieved with the same sandpaper roughness. Therefore, the first test surface setup with just the layer of sandpaper was divided into two subsequent roughness cases. The rippled sandpaper bed was designated as Test Bed 1, while the smoother sandpaper bed was identified as Test bed 2. Thus, the rougher test surface with a patterned spread of steel nuts was identified as Test Bed 3 (see Table 3.1).

Table 3.1: Designations and descriptions of test-bed surface configurations.

Test Surface Designation	Description of test-bed surface configuration
Test Bed 1	32-grit sandpaper with heat-affected rippling
Test Bed 2	Smooth 32-grit sandpaper
Test Bed 3	Smooth 32-grit sandpaper with half-inch tall steel nuts

For the first sandpaper surface condition, Test Bed 1, boundary layer surveys were conducted both for an unheated case and for a 40V control setting on the four surface heaters. Such surveys included collection of both wind and temperature profiles at a range of freestream wind speeds. The purpose of these profiles is to characterize the turbulent flow condition over the test surface. Based on the captured trends from the unheated or neutral setting, one can provide reasonable estimates for dust threshold even for unstable cases. Although the results were preliminary and acquired under trial and error, dust threshold experiments over this test bed were accomplished for an unheated and for a *70V* heater control setting. Figure 3.27 presents an overall flowchart of the main types of experiments conducted over Test Bed 1.

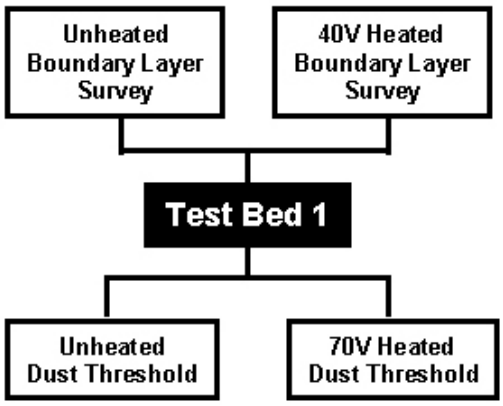

Figure 3.27: Flowchart of types of experiments conducted over Test Bed 1.

Experience from the first set of experiments allowed for improved planning for Test Bed 2, the second reconditioned sandpaper bed (see Figure 3.28 for experimental flowchart). A boundary-layer survey of velocity and temperature was first acquired for an unheated or neutral surface. Based on the range obtained at the Mars Pathfinder Lander site, one neutral and four unstable atmospheric conditions were simulated for dust threshold testing. For the four unstable cases, the Variac controls for the four silicone heaters were set for four experiments by varying the voltage i.e. surface temperature

(*50V*, *80V*, *60V-75V*, and *90V*). To study the effects of heating, velocity and temperature profiles were collected for each of the various heating levels at the same wind speed.

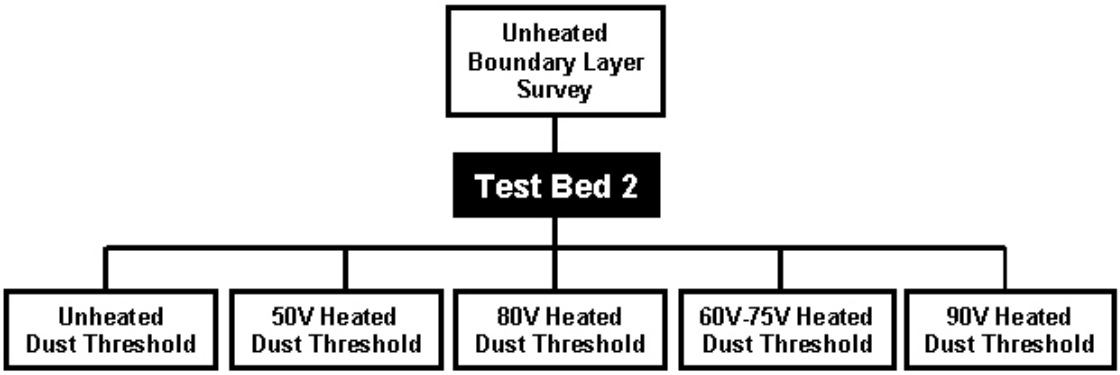

Figure 3.28: Flowchart of types of experiments conducted over Test Bed 2.

Experiments over the combined sandpaper and nuts test bed were unfortunately limited by the availability of the Steam Plant Facility. Nonetheless, three different stability conditions, one neutral and two unstable, were accomplished for three corresponding dust threshold cases. For the first unstable case, the Variac controls for the four heaters were each preset at *50V*, while for the second unstable case, the heater settings were at *90V*. For each of the heating levels, boundary layer surveys of velocity and temperature also were acquired (see Figure 3.29).

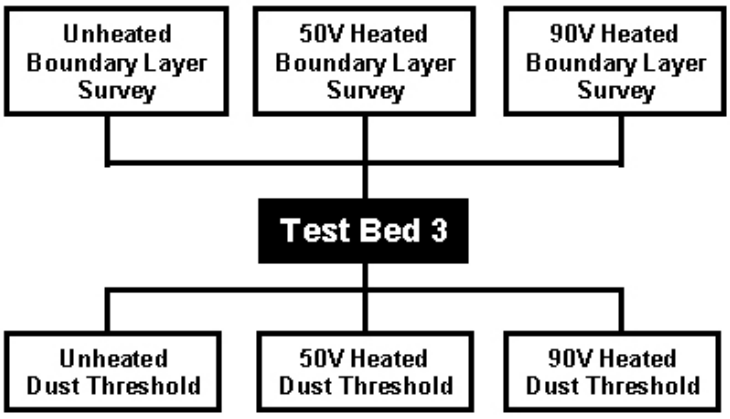

Figure 3.29: Flowchart of types of experiments conducted over Test Bed 3.

Chapter 4: Experiment Results

4.1 Instrument Calibration and Data Reduction

Several voltage measurements were taken during each experiment conducted. All temperature measurements were made using Omega Type-T thermocouples. Voltage readings from the thermocouples were first converted to microvolts and then converted to temperature in degree Celsius using calibration conversions given by the LabVIEW software. According to the software reference, the formulas originated from NIST Monograph 175 and are given as follows:

For a temperature range of *0 °C* to *400 °C*:

$$T = v(2.592800\times10^{-2} + v(-7.602961\times10^{-7} + v(4.637791\times10^{-11} + v(-2.165394\times10^{-15} + v(6.048144\times10^{-20} + v(-7.293422\times10^{-25}))))) \quad (4.1.1)$$

For a temperature range of *-200 °C* to *0 °C*:

$$T = v(2.5949192\times10^{-2} + v(-2.1316967\times10^{-7} + v(7.9018692\times10^{-10} + v(4.2527777\times10^{-13} + v(1.3304473\times10^{-16} + v(2.0241446\times10^{-20} + v(1.2668171\times10^{-24}))))))) \quad (4.1.2)$$

Boundary-layer height location from the traversing Pitot tube system was acquired from a voltage measurement given by a variable resistor geared to a traverse motor. When the traverse mechanism was moved to various heights, a specific voltage was assigned to that height. This voltage was calibrated against a precision steel scale where a voltage at some distance above the surface was assigned to a particular height given by the scale. Obtaining measurements at two heights, a slope conversion from voltage to millimeters was found to be *200.65 mm/volt*. Thus, the height of the Pitot tube can be determined as follows:

$$Height[mm] = [(Measured\,Voltage - Offset\,Voltage) \times 200.65\,mm/volt] + Pitot\,Tube\ Geometric\ Center[mm] \tag{4.1.3}$$

The traversing pitot tube was a flat-tipped, custom-type designed by United Sensor Corporation with tip end cross-section dimensions given in Figure 4.1. Here, the Pitot tube geometric center is given as half of its vertical outer dimension, *0.45 mm*.

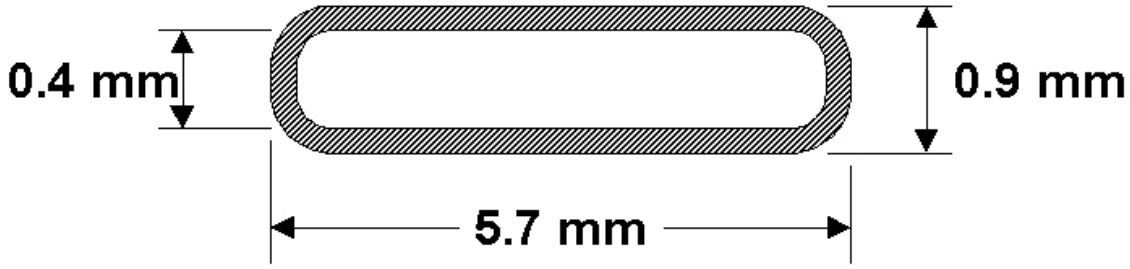

Figure 4.1: End cross-section schematic of United Sensor Corporation flattened Pitot tube.

Chamber pressure was measured at low pressure using a Tavis Corporation Model P-4AS total pressure transducer. It is capable of precision measurement of pressures ranging from *0* to *25 mb*. From a calibration of the instrument, the resulting conversion from voltage to pressure in millibars is given by:

$$P_C = 5.0372 * Tavis\ voltage(in\,volts) \tag{4.1.4}$$

Two different velocity-measuring instruments were used inside MARSWIT. One was a stationary Pitot-static tube placed at a height above the boundary layer where a freestream wind speed can be acquired. This Pitot-static tube was connected to a Setra Model 239 differential pressure transducer with serial number 42893, where its calibration conversion from voltage to differential pressure in Pascals is given by:

$$\Delta P = 27.402 * Setra\ 239\ voltage(in\,volts) \tag{4.1.5}$$

The second velocity-measuring instrument was a Pitot tube vertically traversed next to the stationary Pitot-static tube for generating boundary layer wind profiles. A reference static pressure was measured from a small orifice in the immediate wind-tunnel

ceiling wall, well above the wind-tunnel boundary layer. The static pressure was referenced from wall rather than from the Pitot tube to reduce angular flow effects and random changes due to turbulence generated from traversing the Pitot tube vertically [Owen and Pankhurst (1977)]. This Pitot tube and wall static port system was connected to a second Setra Model 239 differential pressure transducer with serial number 649464 and with a calibration equation given by:

$$\Delta P = 27.469 * Setra\ 239\ voltage(in volts) \tag{4.1.6}$$

Prior to each low-pressure experimental run, a mean voltage at zero velocity was measured from both Setra Model 239 differential pressure transducers and was first subtracted from the voltage measured during an experimental run. The Setra Model 239 differential pressure transducers consist of a metallic diaphragm, which is highly sensitive to local temperature. When the chamber is reduced to near vacuum pressure, the chamber temperature also decreases, thus an additional offset was required for the differential transducers at different pressures other than at one atmosphere. Details on the calibrations of all instruments used in the current experimental study are presented in Appendix A:. Other parameters that were calculated from the experiment are the dynamic and kinematic viscosities, which are explained in Appendix B:, and the mean free path in Appendix C:.

4.2 MARSWIT Temperature Readings

Atmospheric instability is fundamentally described by its negatively sloped vertical temperature profile, which is evident during daytime solar heating of the surface. Such a condition generates a local circulation where warm air parcels rise from the heated

surface, while cooler air parcels fall from above. At higher altitudes, rising air parcels expand due to lower pressures. Based on the ideal gas law, if the air parcel were rise adiabatically (i.e., no heat exchange with its surroundings), the only source for the expansion is through the change in temperature within the air parcel. Such readings are better represented in terms of the potential temperature, θ, the temperature an air parcel would have if it were adiabatically brought to the surface (see Equation 4.2.1).

$$\theta = T\left(\frac{P_T}{P_o}\right)^{-\frac{(\gamma-1)}{\gamma}} \tag{4.2.1}$$

Here, T is the measured temperature reading at a particular height, P_T is the pressure at the height of the temperature reading, P_o is the surface pressure, and γ is the specific heat ratio.

Potential temperature at a particular height essentially provides a more appropriate comparison to the surface temperature since the effects of pressure altitude in the temperature measurements is removed. However, in MARSWIT, the measured vertical temperatures can be considered potential temperatures since all measurements were essentially made near sea level. In this facility, moisture actually contributes a more predominant effect towards the temperature readings. Due to a lower density, water vapor is more buoyant than dry air at the same temperature, thus increasing vertical turbulence in the atmospheric boundary layer. To account for the effects of moisture, potential temperature readings must be converted to virtual potential temperatures, θ_v, which is defined as the temperature a dry air-parcel must have in order to meet the same density of a moist air-parcel. Virtual potential temperature for unsaturated air is calculated by using following equation.

$$\theta_v = \theta\left(1 + 0.61r\right) \tag{4.2.2}$$

Here, *r* is the potential mixing ratio of the current water vapor mass to the mass of dry air, otherwise known as the humidity ratio. According to psychrometrics or the properties of moist air, the moisture holding capabilities of air is a function of temperature. From a psychrometric chart, the humidity ratio increases nearly exponentially with increasing temperature. Thus, referring to Equation 4.2.2, any measured temperature corresponds to a higher value of potential temperature. This is particularly critical for the unstable temperature profiles collected near the surface of the heated MARSWIT test-section surface.

Water vapor content in MARSWIT can be determined by knowing the humidity inside the low-pressure chamber. A humidity reader was not available for use for the time of the current study. Although for later experiments not pertaining to the current study, a Vaisala Model DMP248 humidity reader with a range of *0* to *100%* relative humidity was added to the standard measurement capabilities of MARSWIT. Figure 4.2 presents a set of relative humidity readings conducted during a later but similar experimental test as those herein. Note that once the pressure falls below *16 mb*, the relative humidity is less than *18.5%*. Using a psychrometric chart, if at the experimental chamber-pressure setting of *10 mb* maintains at *18.5%* relative humidity, a temperature reading of *20 °C* correlates to a humidity ratio of *0.47*. According to Equation 4.2.2, such a mixing ratio results to a *29%* higher value of its corresponding virtual potential temperature. For higher temperatures, the difference between the measured and virtual temperatures does increase due to the inherently exponential increase in humidity ratio with temperature.

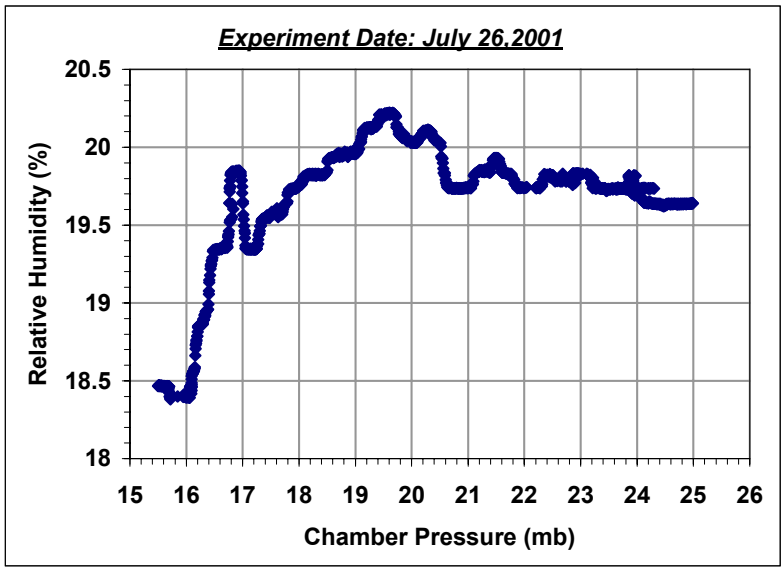

Figure 4.2: Relative humidity readings at a range of low-pressure conditions in the chamber.

For the particular day given in Figure 4.2, the humidity readings showed a significant effect against temperature due to humidity. However, there could be instances were the chamber humidity is low enough that it may be ignored. Such low humidity conditions could arise when the chamber is sustained at near vacuum pressures for a great amount of time. For longer times under vacuum or even pressures lower than those at the Earth's surface, there is a greater possibility that the moisture in the chamber is evaporated.

During the experiments discussed in this report, the standard procedures for evacuating the chamber began with an initial pump-down session in the early morning and then a final pump-down session to the desired low-pressure condition later in the morning. Some pre-final pump-downs also were sometimes conducted when available. In the periods when pressures were maintained much lower than Earth sea level atmosphere, thermodynamic conditions may provide greater possibilities to remove moisture in the chamber. Thus, since a humidity reader or hygrometer was unavailable during the time of the experiments made for this project, it was assumed that the temperature readings

collected do not require corrections due to moisture. However, for future experiments, it is recommended that the humidity is measured at the desired chamber pressure condition when measuring boundary layer temperatures.

4.3 Corrections for Traversing Flattened Pitot-Tube

Since the traversing Pitot tube travels through the wind tunnel boundary layer, it is subjected to a few effects that may alter the velocity readings. Thus, corrections may be required due to the effects of turbulence, the presence of a velocity-gradient, viscosity and wall proximity. Turbulent velocity fluctuations may cause pressure changes at Pitot-static tube orifices. Since in the present experimental setup, the static pressure is measured from a wall orifice where turbulence corrections are known to be small, where the effect of turbulence against the flattened Pitot tube are negligible. When the static port opening is essentially maintained at zero degrees angle or parallel with the flow, only up to *1%* errors generate for even angle fluctuations as large as *20 degrees* [Owen and Pankhurst (1977)]. Since the probe is a thin-walled, square-ended type, it is also insensitive to yaw.

Corrections are also necessary for conditions where the Pitot tube is placed within a velocity gradient. When a flattened Pitot tube is being used for measurements within a boundary layer, it senses a velocity-gradient just in front of the mouth of its opening, where a higher velocity forms at the top of the opening than that at the bottom (see Figure 4.3). A Δp associated with this velocity difference essentially causes a "shear displacement" shifting the effective center of the Pitot tube from its geometric center towards the region of higher velocity.

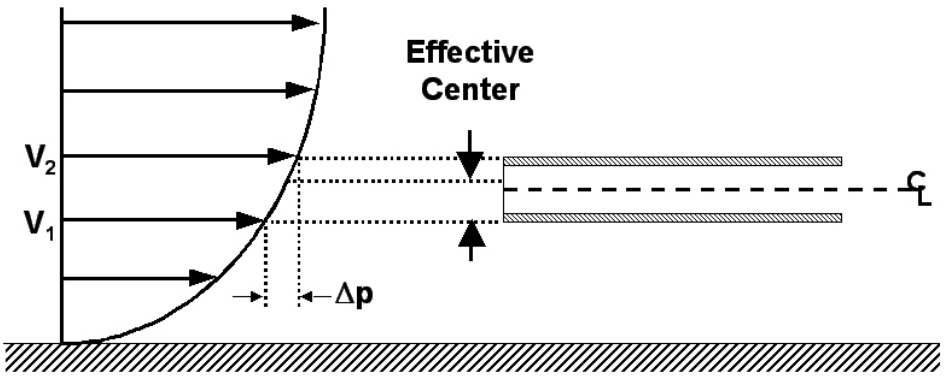

Figure 4.3: Effective center of a flattened Pitot tube when placed within a velocity gradient.

According to Young and Maas (1936), the additive correction, C_z, for the measurement height, z, of the Pitot tube can be corrected according to the following equation.

$$\frac{C_z}{D} = 0.13 + 0.08\frac{d}{D} \tag{4.3.1}$$

Here, d is the inner height of the Pitot tube, while D is its outer height. From Figure 4.1, the flattened pitot tube used for the current study has the dimensions, $d = 0.4\ mm$ and $D = 0.9\ mm$. Thus, for $d/D = 0.444$, $C_z/D = 0.17$ or the additive correction to the measurement height is $0.17D$. In a later study, MacMillan (1956) showed that the above result for C_z/D is high by 0.02. Therefore, for the current study the height measurement was increased by $0.15D$.

Viscosity at low-Reynolds-number flows also generates corrections to the velocity readings. Due to an extremely slow response rate, "small" pitot-tubes are generally subject to viscosity effects, in particular, at low speeds inherent inside a boundary layer. According to MacMillan (1954), the steps in adjusting the velocity reading requires an application of a Pitot tube coefficient of pressure, C_p, correction. First calculate the local velocity, U, using the measured differential pressure, ΔP, and assuming $C_p = 1$.

$$C_p = \frac{\Delta P}{\frac{1}{2}\rho U^2} = 1 \qquad \Rightarrow \qquad U = \sqrt{\frac{2\Delta P}{\rho}} \quad \text{where: } \rho \text{ is the chamber density} \tag{4.3.2}$$

The next step is to calculate the Pitot tube opening Reynolds number.

$$Re_d = \frac{Ud}{\nu} \quad \text{where: } d = \text{the Pitot tube inner height and } \nu = \text{kinematic viscosity} \tag{4.3.3}$$

Given the above Reynolds number calculation, the correction C_p can be calculated as follows.

$$\text{For } 0 \le Re_d \le 13.6,\ C_p = -0.06795274 \log_e[Re_d] + 1.16136140 \tag{4.3.4}$$

$$\text{For } 13.6 \le Re_d \le 1000,\ C_p = 0.003722934 \log_e[Re_d] + 0.974282884 \tag{4.3.5}$$

$$\text{For } Re_d > 1000,\ C_p = 1. \tag{4.3.6}$$

Finally, calculate the corrected velocity, U_c, using the appropriate correction C_p.

$$U_c = \frac{1}{\sqrt{C_p}} \sqrt{\frac{2\Delta P}{\rho}} \tag{4.3.7}$$

A final correction to the flattened Pitot tube velocity reading must be applied due to wall proximity. As the distance between the Pitot tube and the surface closes, the flow between the two boundaries increases, thus decreasing the flow into the Pitot tube. According to experimental data presented in MacMillan (1956), a percent correction to the measured differential pressure can be found for a particular Pitot tube size and distance from the surface.

Overall, three types of corrections were applied to the velocity readings from the traverse flattened Pitot tube: 1) velocity gradient correction, 2) viscosity correction, and 3) wall proximity correction. The specifics in the procedures taken in applying these corrections to the experiments can be viewed in detail in Appendix D.

4.4 Generation and Characteristics of Wind Profiles

All wind profiles were generated from an average of two consecutive vertical traverses of the flattened Pitot tube that spanned the boundary layer within *30* to *40* seconds at a single downstream location in the wind-tunnel test section. One profile was obtained by traversing the Pitot tube down to the near surface and the other was obtained by traversing back up to the original test-section centerline position. An average wind profile was generated by averaging the wind speeds measured at a matching height of within *5%* to *10%* difference, giving an average difference in velocity between the two traverses of no more that *10%* for heights normally located at the "Law-of-the-wall" region. This averaging technique is best viewed by plotting the up-traverse, down-traverse, and average wind profiles on the same plot of logarithm of height, *z*, versus local wind speed, *U* (see Figure 4.4).

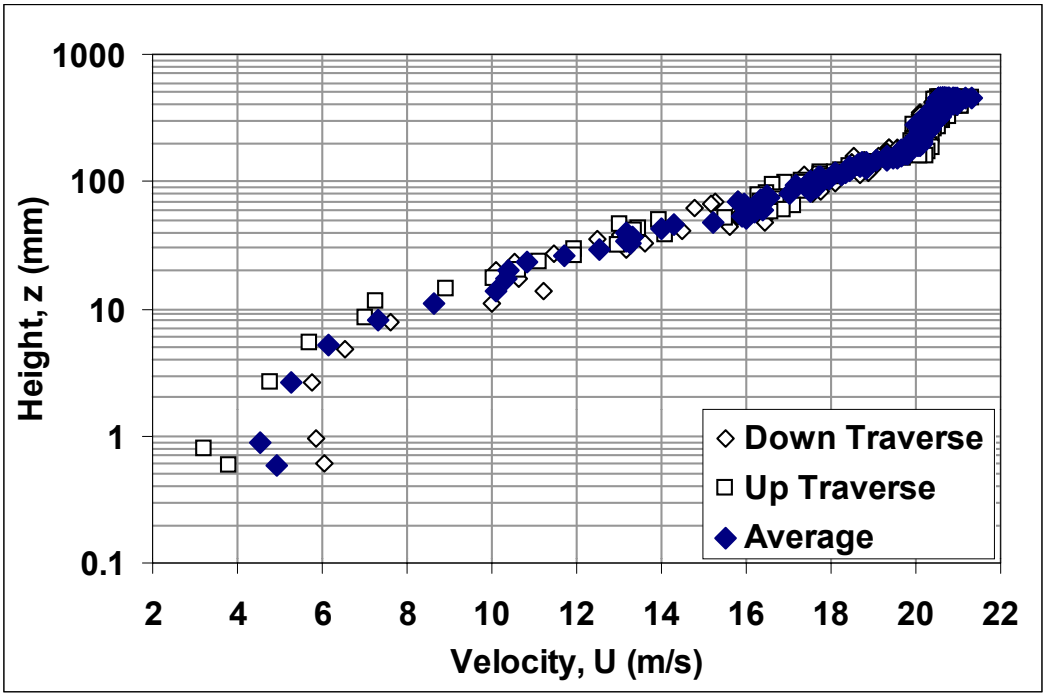

Figure 4.4: Sample plot of down-traverse, up-traverse, and averaged wind profiles from one experimental run.

Note that velocity measurements above two centimeters are remarkably similar between the up-traverse and down-traverse profiles. However, in the near-surface region, a slight variation occurs. This hysteresis-type variation is due to the limited speed that the Pitot tube is being traversed through the boundary layer and to the higher degree of turbulence that is inherent of the near surface region. The single-speed traverse motor allows the Pitot tube to collect data though the boundary layer moving at about a *cm/sec*. However, for future boundary-layer experiments, the traverse speed near the surface should be reduced so that a slow-response Pitot tube is able to capture the necessary velocity data that accurately quantifies the shape of the wind profile. Since the traverse Pitot tube was limited to move at a speed, which varied the data near the surface, two wind profiles were collected to obtain an average.

General parameters that were calculated from the wind profiles were the freestream velocity, U_F, the test section Reynolds number, Re_x, the displacement height, δ^*, the momentum-deficit height, θ, and the momentum-deficit Reynolds number, Re_θ.. The only parameter estimated from the profiles was the boundary-layer height, δ.

Boundary-layer height, δ, was estimated from the semi-logarithmic wind profile and also from the linear plot of velocity as a function of height similar to the one shown in Figure 4.5. Such an estimate was verified by a graph of the corresponding non-dimensional velocity, U/U_F, as a function of non-dimensional height, z/δ (see Figure 4.6). Plotted along with the non-dimensional profile in Figure 4.6 is the profile for laminar flow [Shames (1982)], which was used to verify that the measured wind profile is in a simulated atmospheric turbulent flow. The equations used to generate the dimensionless laminar wind profile are provided in Appendix E:.

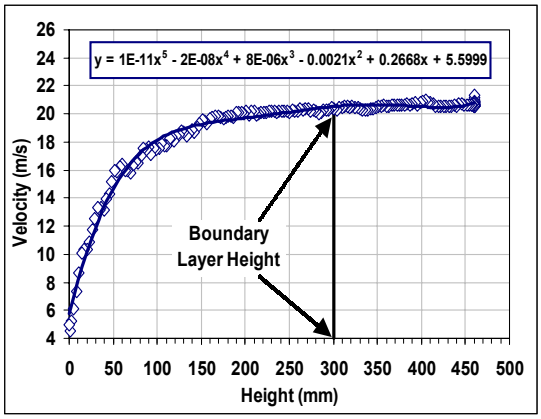

Figure 4.5: Sample plot of velocity as a function of height both on linear scales.

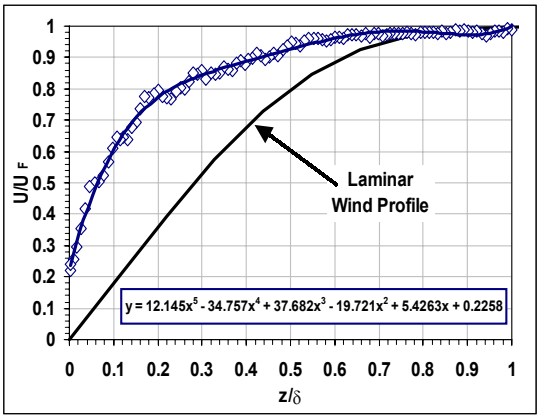

Figure 4.6: Sample plot of non-dimensional velocity as a function of non-dimensional height.

A stationary Pitot-static tube was installed to measure a continuous freestream reading during an experimental run. However, an alternative source was used as the reference freestream velocity value. The freestream velocity, U_F, was determined by averaging the velocities measured above the boundary-layer height by the traversing Pitot tube. This procedure for designating U_F was done for consistency with the shape of the wind profile plots. Since the traverse Pitot tube static port was located in the ceiling, where it was undisturbed by the turbulent boundary layer, the traverse Pitot tube was able to provide a static pressure reading without the effects of flow angularities. The stationary Pitot-static tube reading was mainly used as a near real-time monitor of the wind-tunnel speed during an experimental run.

Using the value for the mean freestream velocity, U_F, the test section Reynolds number can be determined using the following equation:

$$Re_x = \frac{U_F x}{\nu} \tag{4.4.1}$$

Here, ν is the average kinematic viscosity and x is 6.71 m, which is the distance from the leading edge of the fetch to the downstream position of the traversing Pitot tube.

Displacement height, δ^*, momentum-deficit height, θ, and momentum-deficit Reynolds number, Re_θ, were calculated based on equations found in White (1981). Here, the displacement height and momentum-deficit height are respectively defined as follows:

$$\delta^* = \int_0^\delta \left(1 - \frac{U}{U_F}\right) dz = \sum_{n=1}^{n_\delta} \left(1 - \frac{U}{U_F}\right)\left(z_{n+1} - z_n\right) \tag{4.4.2}$$

$$\theta = \int_0^\delta \frac{U}{U_F}\left(1 - \frac{U}{U_F}\right) dz = \sum_{n=1}^{n_\delta} \left(\frac{U}{U_F}\right)\left(1 - \frac{U}{U_F}\right)\left(z_{n+1} - z_n\right) \tag{4.4.3}$$

where: for $n = 1 \Rightarrow z$ = lowest height

for $n = n_\delta \Rightarrow z = \delta$

The momentum-deficit Reynolds number was then calculated as follows:

$$Re_\theta = \frac{U_F \theta}{\nu} \tag{4.4.4}$$

Using Re_θ, the value of the Von Kármán constant, k, which will later be used for boundary layer analysis sections, may be determined. According to Patel (1965), k was experimentally estimated as 0.418. White (1981) later showed that such an estimate is valid for $Re_\theta \geq 600$; however, for $425 < Re_\theta < 600$, k becomes a function of Re_θ and of the wind profile shape factor according to the following equation:

$$k = 0.0013 R_\theta - 0.362 \tag{4.4.5}$$

For conditions where $Re_\theta \leq 425$, the boundary layer is considered to be in transitional flow. The Von Kármán constant is essentially a parameter analogous to turbulent boundary layers only. Thus, for wall-shear flows in transition, the Von Kármán constant

is generally inapplicable, and the corresponding wind profile is excluded from turbulent boundary layer analysis.

4.5 Test Conditions during MARSWIT Boundary-Layer Surveys

Three surface configurations were built and tested. The initial test bed consisted of smoothly layered 36-grit sandpaper similar in type to the immediate upwind fetch. However, over the center section of heated plates, the sandpaper delaminated and formed ripples due to extensive pre-experimental surface heating resulting to a rougher surface. A second test bed configuration was considered after re-adhering the sandpaper over the aluminum plates forming a much smoother surface. The third and final test bed included the same sandpaper layer used in the first two surface plus pre-patterned rows of half-inch tall hexagonal nuts arranged over the test bed and over the immediate upwind fetch. Thus, in all, three roughness conditions were simulated for the current study and were designated as follows in Table 4.1.

Table 4.1: Designations and descriptions of test-bed surface configurations.

Test Surface Designation	Description of test-bed surface configuration
Test Bed 1	32-grit sandpaper with heat-affected rippling.
Test Bed 2	Reconditioned Test Bed 1 forming a smooth 32-grit sandpaper surface.
Test Bed 3	Smooth 32-grit sandpaper with a pattern of half-inch tall steel nuts distributed over the sandpaper surface.

Surveys of wind and temperature profiles were collected over the three test-surface conditions, subjected under various heating levels. Table 4.2 displays a list of the sub-surface heater settings attempted over each test-bed configuration, along with the

corresponding mean surface temperatures. Note that for the heated cases, an equivalent voltage, as given in Table 4.2, was applied to all four surface heaters for one particular test-bed stability case.

Table 4.2: Surface-heating settings for boundary layer profiles conducted over the three test bed surfaces.

Test Surface Designation	Voltage Setting for Surface Heaters	Mean Surface Temperature (°C)
Test Bed 1	Unheated	15.75
	40V Heated	65.63
Test Bed 2	Unheated	19.15
Test Bed 3	Unheated	20.48
	50V Heated	83.83
	90V Heated	201.41

The main goal was to try to maintain a constant surface temperature during one boundary layer profile run, in particular, for the higher wind-tunnel speeds. Normally at higher speeds, the leading heated-surface cools to a lower temperature than the proceeding heated surfaces. As the heat released from the lead test-bed surface travels downwind, the latter surfaces become even much hotter leading to axial conduction. Later, results will show that the surface temperatures nearly were constant for any wind speed even when each heater was preset to the same voltage level reducing axial conduction.

Wind tunnel and chamber conditions for the unheated or neutral boundary-layer surveys, of which one set of wind and temperature profiles was collected from each of the three test-bed surface configurations, are summarized in Tables 4.3, 4.4, and 4.5. Here, each of the values presented is an average reading during a particular boundary-layer profile experiment. Note that the chamber pressure was maintained at approximate average of *10 mb* during each profile.

Table 4.3: Experimental conditions from the unheated boundary-layer surveys over Test Bed 1.

Wind Speed (m/s)	Wind Tunnel Temperature (° C)	Chamber Pressure (mb)	Chamber Density (kg/m^3)	Dynamic Viscosity (kg/m s)	Kinematic Viscosity (m^2/s)	Mean Free Path (μm)	Surface Temperature (° C)
19.91	17.46	9.73	0.01167	1.8012E-05	0.00154	10.05	15.80
30.03	18.67	9.98	0.01191	1.8071E-05	0.00152	9.85	15.87
39.27	18.66	10.03	0.01198	1.8071E-05	0.00151	9.80	15.84
49.81	18.28	10.16	0.01215	1.8049E-05	0.00149	9.66	15.88
60.04	18.09	10.09	0.01207	1.8042E-05	0.00149	9.72	15.84
68.97	18.20	9.96	0.01191	1.8045E-05	0.00151	9.85	15.84
85.70	14.32	9.56	0.01159	1.7865E-05	0.00154	10.09	15.15

Table 4.4: Experimental conditions from the unheated boundary-layer surveys over Test Bed 2.

Wind Speed (m/s)	Wind Tunnel Temperature (° C)	Chamber Pressure (mb)	Chamber Density (kg/m^3)	Dynamic Viscosity (kg/m s)	Kinematic Viscosity (m^2/s)	Mean Free Path (μm)	Surface Temperature (° C)
22.96	22.30	10.08	0.01188	1.824E-05	0.00154	9.91	19.45
30.56	22.30	10.06	0.01187	1.824E-05	0.00154	9.92	19.40
42.58	22.08	10.05	0.01186	1.823E-05	0.00154	9.93	19.37
50.18	21.07	10.09	0.01195	1.818E-05	0.00152	9.85	18.94
60.13	21.33	10.12	0.01197	1.819E-05	0.00152	9.83	18.96
70.64	20.46	10.08	0.01196	1.815E-05	0.00152	9.83	18.98
85.53	20.20	9.99	0.01187	1.814E-05	0.00153	9.91	18.98

Table 4.5: Experimental conditions from the unheated boundary-layer surveys over Test Bed 3.

Wind Speed (m/s)	Wind Tunnel Temperature (° C)	Chamber Pressure (mb)	Chamber Density (kg/m^3)	Dynamic Viscosity (kg/m s)	Kinematic Viscosity (m^2/s)	Mean Free Path (μm)	Surface Temperature (° C)
38.47	22.62	10.48	0.01235	1.826E-05	0.00148	9.54	20.46
50.88	22.33	10.47	0.01235	1.824E-05	0.00148	9.54	20.46
61.97	22.34	10.47	0.01234	1.824E-05	0.00148	9.54	20.45
75.50	21.93	10.48	0.01238	1.822E-05	0.00147	9.51	20.47
88.98	21.28	10.53	0.01246	1.819E-05	0.00146	9.44	20.54

Corresponding wind profile characteristics of the unheated or neutral cases for the three test surfaces are provided in Tables 4.6, 4.7, and 4.8. Note that the calculated momentum-deficit Reynolds number, Re_θ, for the first wind speed case of Test Bed 1, is less than 425 (see Table 4.6). Such condition indicates that the test section flow is still in

transition. Thus, any boundary layer profile with $Re_\theta \leq 425$ was excluded from any further turbulence analysis.

Table 4.6: Wind profile characteristics from the unheated boundary-layer surveys over Test Bed 1.

Wind Speed (m/s)	Test Section Reynolds Number	Boundary Layer Height (mm)	Displacement Height (mm)	Momentum Height (mm)	Momentum Reynolds Number	Von Kármán Constant
19.91	86490	299.56	38.46	26.52	**342**	N/A
30.03	132781	300.69	38.53	27.55	545	0.347
39.27	174537	300.45	36.00	26.55	691	0.418
49.81	224817	300.56	38.93	29.08	975	0.418
60.04	269385	298.41	41.56	30.86	1240	0.418
68.97	305304	300.17	42.60	31.87	1451	0.418
85.70	372708	300.75	40.77	30.84	1714	0.418

Table 4.7: Wind profile characteristics from the unheated boundary-layer surveys over Test Bed 2.

Wind Speed (m/s)	Test Section Reynolds Number	Boundary Layer Height (mm)	Displacement Height (mm)	Momentum Height (mm)	Momentum Reynolds Number	Von Kármán Constant
22.96	100293	300.35	39.92	28.89	432	0.200
30.56	133314	300.06	43.59	31.59	628	0.418
42.58	185707	300.31	45.74	33.78	935	0.418
50.18	221101	299.94	43.38	32.38	1068	0.418
60.13	265333	300.52	45.38	33.69	1333	0.418
70.64	311994	300.90	46.53	34.75	1617	0.418
85.53	375126	299.07	48.90	36.20	2025	0.418

Table 4.8: Wind profile characteristics from the unheated boundary-layer surveys over Test Bed 3.

Wind Speed (m/s)	Test Section Reynolds Number	Boundary Layer Height (mm)	Displacement Height (mm)	Momentum Height (mm)	Momentum Reynolds Number	Von Kármán Constant
38.47	174523	349.75	36.80	26.25	683	0.418
50.88	230976	348.35	41.03	28.95	997	0.418
61.97	281155	350.84	44.53	31.03	1301	0.418
75.50	343977	348.65	47.00	32.91	1688	0.418
88.98	408744	350.00	47.63	33.76	2058	0.418

Unstable or heated boundary-layer surveys also were collected over Test Bed 1 and Test Bed 3. Only one set of heated profiles was collected over Test Bed 1, while two

were tested over Test Bed 3. Unfortunately, due to facility constraints, unstable profiles could not be obtained for Test Bed 2. Tables 4.9, 4.10, and 4.11 show the wind tunnel and chamber conditions from the heated surveys, while Tables 4.12, 4.13, and 4.14 present the corresponding wind-profile characteristics. For the lowest wind speed case over Test Bed 1, $Re_\theta \leq 425$ (see Table 4.12), thus the corresponding wind profile was excluded from further analysis.

Table 4.9: Wind tunnel and chamber conditions from the boundary-layer surveys over Test Bed 1 heated under 40V heater settings.

Wind Speed (m/s)	Wind Tunnel Temperature (° C)	Chamber Pressure (mb)	Chamber Density (kg/m^3)	Dynamic Viscosity (kg/m s)	Kinematic Viscosity (m^2/s)	Mean Free Path (μm)	Mean Surface Temperature (° C)
20.63	18.66	9.14	0.01091	1.807E-05	0.00166	10.76	63.10
33.35	18.28	8.95	0.01069	1.805E-05	0.00169	10.97	70.53
46.55	18.09	9.56	0.01143	1.804E-05	0.00158	10.26	63.97
59.05	18.20	10.16	0.01215	1.805E-05	0.00148	9.65	56.79
83.07	14.32	9.70	0.01175	1.787E-05	0.00152	9.95	73.76

Table 4.10: Wind tunnel and chamber conditions from the boundary-layer surveys over Test Bed 3 heated under 50V heater settings.

Wind Speed (m/s)	Wind Tunnel Temperature (° C)	Chamber Pressure (mb)	Chamber Density (kg/m^3)	Dynamic Viscosity (kg/m s)	Kinematic Viscosity (m^2/s)	Mean Free Path (μm)	Mean Surface Temperature (° C)
28.79	22.89	10.51	0.01237	1.827E-05	0.00148	9.53	85.24
39.63	22.93	10.51	0.01237	1.827E-05	0.00148	9.53	85.95
50.04	22.60	10.55	0.01243	1.825E-05	0.00147	9.48	83.67
69.42	22.23	10.54	0.01243	1.824E-05	0.00147	9.47	82.58
88.33	21.81	10.70	0.01264	1.822E-05	0.00144	9.32	81.69

Table 4.11: Wind tunnel and chamber conditions from the boundary-layer surveys over Test Bed 3 heated under 90V heater settings.

Wind Speed (m/s)	Wind Tunnel Temperature (° C)	Chamber Pressure (mb)	Chamber Density (kg/m^3)	Dynamic Viscosity (kg/m s)	Kinematic Viscosity (m^2/s)	Mean Free Path (μm)	Mean Surface Temperature (° C)
35.88	26.22	10.43	0.01214	1.843E-05	0.00152	9.73	201.60
47.65	26.10	10.49	0.01221	1.842E-05	0.00151	9.68	201.18
64.82	25.11	10.48	0.01224	1.837E-05	0.00150	9.65	200.99
88.91	26.50	10.56	0.01228	1.844E-05	0.00150	9.63	201.68

Table 4.12: Wind profile characteristics from the boundary-layer surveys over Test Bed 1 heated under constant 40V surface heater settings.

Wind Speed (m/s)	Test Section Reynolds Number	Boundary Layer Height (mm)	Displacement Height (mm)	Momentum Height (mm)	Momentum Reynolds Number	Von Kármán Constant
20.63	83502	300.75	40.93	27.56	343	N/A
33.35	132501	299.92	40.55	28.35	560	0.366
46.55	197741	300.36	40.94	27.23	803	0.418
59.05	266669	301.30	40.94	27.23	1083	0.418
83.07	366404	300.67	41.00	27.30	1491	0.418

Table 4.13: Wind profile characteristics from the boundary-layer surveys over Test Bed 3 heated under constant 50V surface heater settings.

Wind Speed (m/s)	Test Section Reynolds Number	Boundary Layer Height (mm)	Displacement Height (mm)	Momentum Height (mm)	Momentum Reynolds Number	Von Kármán Constant
28.79	130707	323.67	37.48	25.74	502	0.290
39.63	179843	324.12	40.18	27.94	749	0.418
50.04	228452	322.72	43.19	30.17	1028	0.418
69.42	317224	323.37	46.41	32.56	1540	0.418
88.33	410747	322.21	45.17	31.60	1935	0.418

Table 4.14: Wind profile characteristics from the boundary-layer surveys over Test Bed 3 heated under constant 90V surface heater settings.

Wind Speed (m/s)	Test Section Reynolds Number	Boundary Layer Height (mm)	Displacement Height (mm)	Momentum Height (mm)	Momentum Reynolds Number	Von Kármán Constant
35.88	158575	301.32	45.02	30.50	721	0.418
47.65	211801	299.40	47.35	32.07	1013	0.418
64.82	289491	302.06	49.69	33.46	1445	0.418
88.91	396951	301.38	50.18	33.99	2012	0.418

4.6 Estimation of Aerodynamic Roughness Height from Wind Profiles

Aerodynamic roughness height, z_o, is defined as the height above the ground where the wind speed is zero, not necessarily the height of an individual surface element. Variations in roughness height occur not only for changes in surface elements height, but also for different surface coverage and assortment of the roughness. Thus, aerodynamic roughness is primarily a function of a particular surface configuration and is independent of wind speed, atmospheric stability, or shear stress. Roughness height may be

approximated if the individual roughness element heights are known along a particular length of fetch [Stull (1988)]. However, for conditions where there are step changes in roughness, z_o can best be determined from a neutrally stratified boundary-layer wind profile measured above that surface.

In order to achieve neutrally stratified turbulent boundary layer in the wind tunnel, an infinite value for the Monin-Obukhov stability length must exist. Stability length is essentially a function of the three-dimensional fluctuating turbulent velocities, which only can be measured by fast-response sensors not available for the current study. Since the stability length is difficult to measure, neutral stratification can be determined through a set of temperature and velocity profiles at various freestream wind speeds. A boundary layer is neutrally stratified when the temperature is constant with height and when a common roughness height, z_o, can be extrapolated from the near-surface wind profiles.

From the near-surface wind profile, a logarithmic-linear regression curve-fit can be developed revealing the coefficients A_U and B_U in the following expression:

$$z = A_U e^{B_U U(z)} \tag{4.6.1}$$

where z is the height from the surface and $U(z)$ is local velocity at height z. Rearranging this equation in terms of U as a function of z, the logarithmic-linear profile in the near-surface region can be compared to the equation for fully developed turbulent flow over a rough-wall surface.

Rearranged equation: $$U(z) = \frac{1}{B_U} ln\left(\frac{z}{A_U}\right) \tag{4.6.2}$$

Rough-wall equation: $$U(z) = \frac{u^*}{k} ln\left(\frac{z}{z_0}\right) \tag{4.6.3}$$

Here, coefficient A_U corresponds directly to the roughness height, z_o; while the slope of the line, $1/B_U$, is equivalent to u^*/k, where k is the Von Kármán constant. Due to low-pressure or low-density effects, the near-surface wind profile, where $y^+ < 5$ to 7, essentially corresponds to the viscous sublayer.

In a systematic manner, a logarithmic-linear regression line equation was generated for each of the individual near-surface wind profile generated from one velocity run, such as the sample shown in Figure 4.7. Once a close match of coefficient A_U was achieved, an average coefficient A_U was calculated and was designated as the test surface roughness height, z_o. With this average z_o, the logarithmic-linear regression lines can be adjusted to the same average z_o giving the final form of the regression line equation for each individual wind profile. Figure 4.8 presents the adjusted logarithmic-linear regression equations originally formed from Figure 4.7. Note that there is little change between the figures. This suggests that a relatively accurate determination of z_o has been achieved. Wind profiles generated from the neutral cases are presented in Figures 4.9, 4.11, and 4.13 along with their corresponding temperature profiles in Figures 4.10, 4.12, and 4.14, respectively, and their estimated roughness heights.

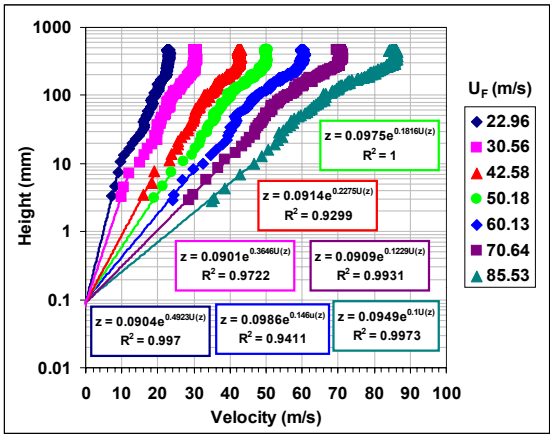

Figure 4.7: Initial step in roughness height estimation.

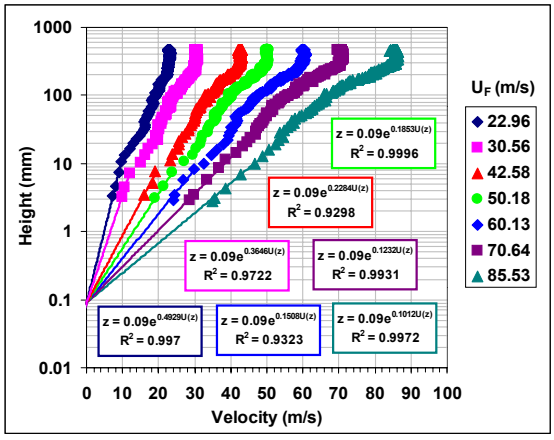

Figure 4.8: Final step in roughness height estimation.

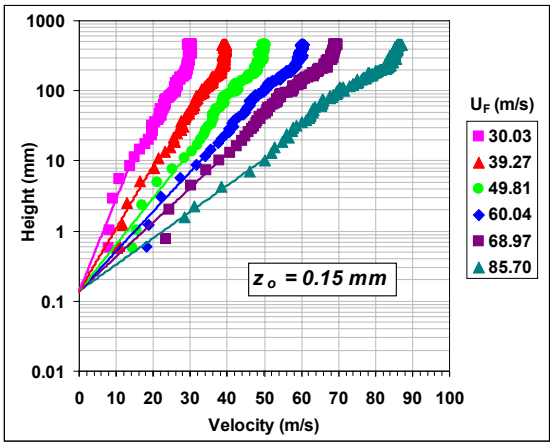

Figure 4.9: Roughness height estimate from unheated wind profiles over Test Bed 1.

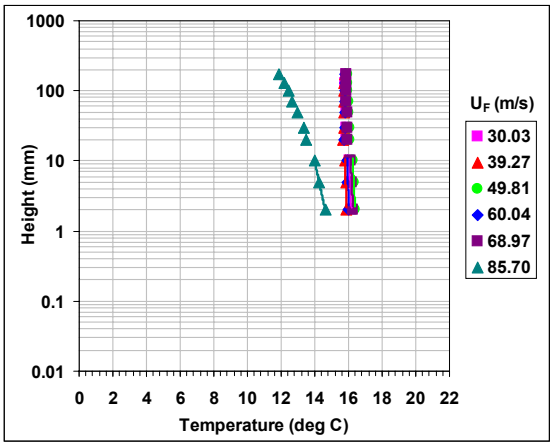

Figure 4.10: Temperature profiles from unheated boundary layer survey over Test Bed 1.

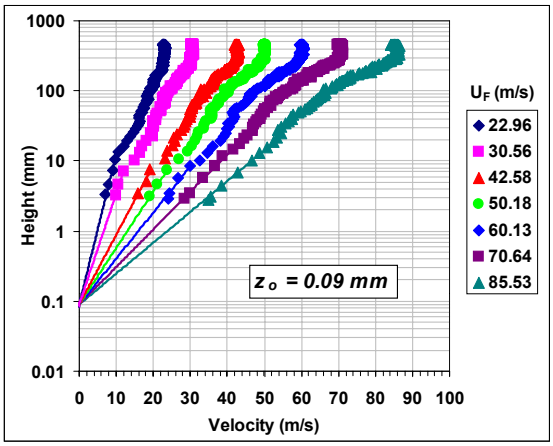

Figure 4.11: Roughness height estimate from unheated wind profiles over Test Bed 2.

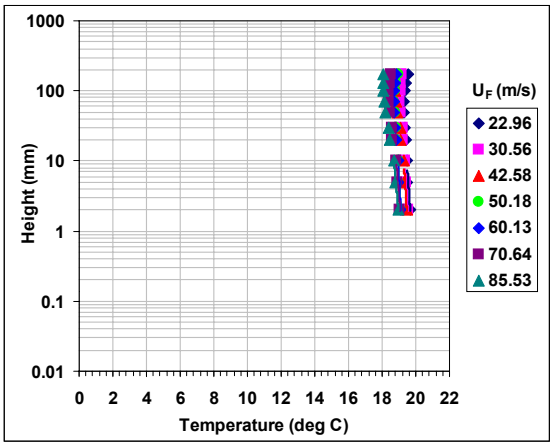

Figure 4.12: Temperature profiles from unheated boundary layer survey over Test Bed 2.

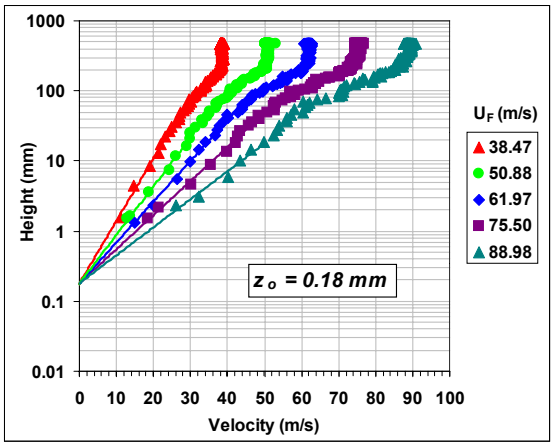

Figure 4.13: Roughness height estimate from unheated wind profiles over Test Bed 3.

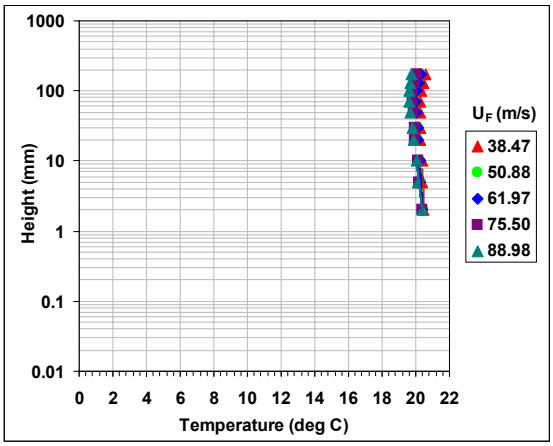

Figure 4.14: Temperature profiles from unheated boundary layer survey over Test Bed 3.

Boundary-layer surveys also were collected under unstable atmospheric conditions for the configurations given in Test Bed 1 and Test Bed 3. These measurements not only show the distortional effects of heating, but also show whether instabilities generated upon initial heating of the bed dissipate into fully turbulent flow. One set of wind and temperature profiles were obtained over Test Bed 1 with the heater voltages set constantly at about 40V, while two sets of unstable profiles were collected over Test Bed 3 respectively at 50V and 90V constant heater voltages.

Although values of aerodynamic roughness are best estimated and represented by neutrally stratified wind-profiles, apparent roughness heights were estimated from the unstable cases using the same previously-defined extrapolation technique. Since heating alters the shape of the near-surface wind profiles, the resulting roughness height value from an unstable case will not be a true representative of the particular surface configuration but rather an artifact of the surface stability condition. Table 4.15 displays the resulting mean roughness heights estimated from the unstable near-surface profiles over Test 1 and Test Bed 3. The unstable wind profile over Test Bed 1 is plotted in Figure 4.15, while the two generated over Test Bed 3 are graphed in Figures 4.17 and 4.19. Corresponding unstable temperature profiles also are respectively shown in Figures 4.16, 4.18, and 4.20. A comparison of the mean roughness heights from the matching unheated and heated boundary-layer wind profiles over Test Bed 1 and Test Bed 3 is also tabulated in Table 4.16.

Table 4.15: Roughness height results from heated or unstable boundary-layer profiles.

Test Surface	Heater Voltage	Mean Surface Temp (°C)	Roughness Height (mm)
Test Bed 1	40V	65.63	0.35
Test Bed 3	50V	83.83	0.32
Test Bed 3	90V	201.36	0.44

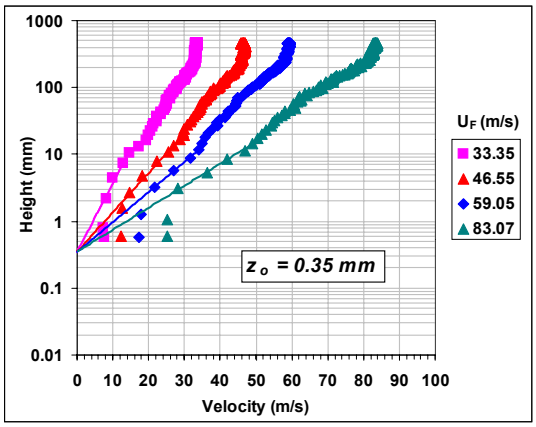

Figure 4.15: Roughness height estimate from wind profiles over Test Bed 1 for 40V heater setting.

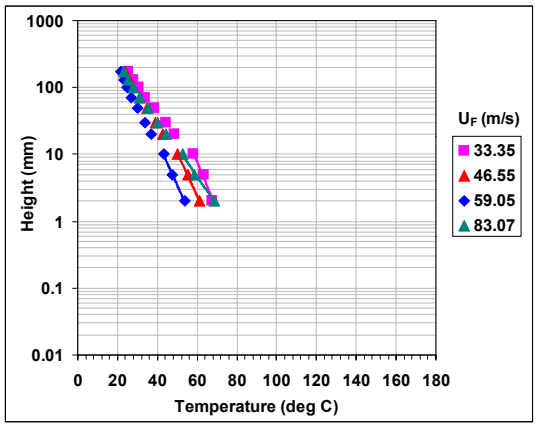

Figure 4.16: Temperature profiles from boundary layer survey over Test Bed 1 for 40V heater setting.

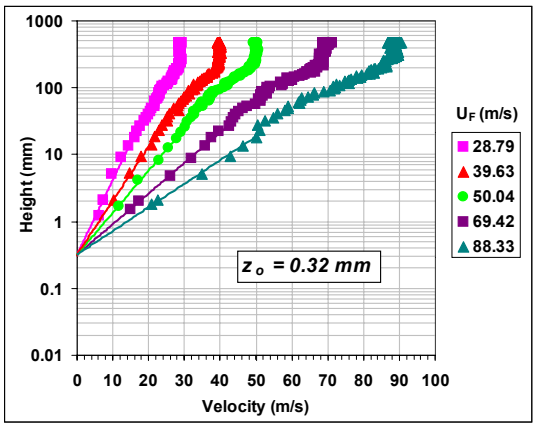

Figure 4.17: Roughness height estimate from wind profiles over Test Bed 3 for 50V heater setting.

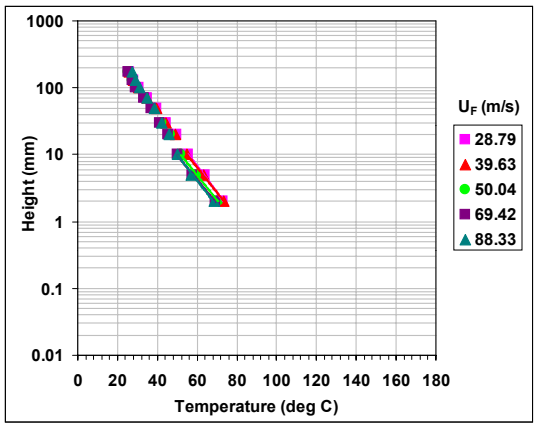

Figure 4.18: Temperature profiles from boundary layer survey over Test Bed 3 for 50V heater setting.

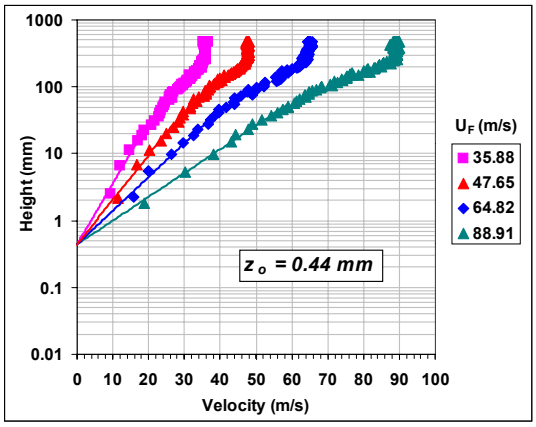

Figure 4.19: Roughness height estimate from wind profiles over Test Bed 3 for 90V heater setting.

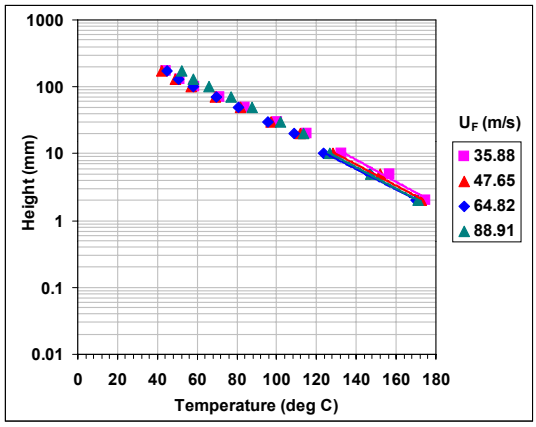

Figure 4.20: Temperature profiles from boundary layer survey over Test Bed 3 for 90V heater setting.

Table 4.16: Comparison of roughness heights between unheated and heated boundary layer surveys performed over Test Bed 1 and Test Bed 3.

	Unheated or Neutral Cases		Heated or Unstable Cases	
Test Surface Designation	Mean Surface Temperature (°C)	Estimated Roughness Height (mm)	Mean Surface Temperature (°C)	Estimated Roughness Height (mm)
Test Bed 1	15.75	0.15	65.63	0.35
Test Bed 3	20.48	0.18	83.83	0.32
			201.36	0.44

For the unstable condition generated over Test Bed 1, an apparent roughness height of 0.35 mm was estimated (see Figure 4.15), a 60% increase from its corresponding unheated case as shown in Table 4.16. A similar trend was noted between the unheated case and the heated cases of Test Bed 3. Such increases in z_o for the unstable cases are generally characteristic of the distortional effects of heating or surface stability. The convergence of roughness height from the unstable wind profiles suggests that instabilities generated by buoyant convections were immediately dissipated in the wind tunnel flow.

Alteration of the roughness height estimate was further illustrated from a set of boundary layer surveys over Test Bed 2 maintained at the same about the same wind, but varied in surface temperatures. Five profiles were collected at the surface temperature distributions given in the following Figure 4.21, which generated the vertical wind and temperature profiles at a test bed downstream distance of *245 cm* shown in Figures 4.22 and 4.23. Note the upward shift for a predicted z_o in the near-surface wind profiles as the surface temperature is increased for greater instability. Such conditions denote that an additive vertical component of velocity is present when the boundary layer is more buoyant.

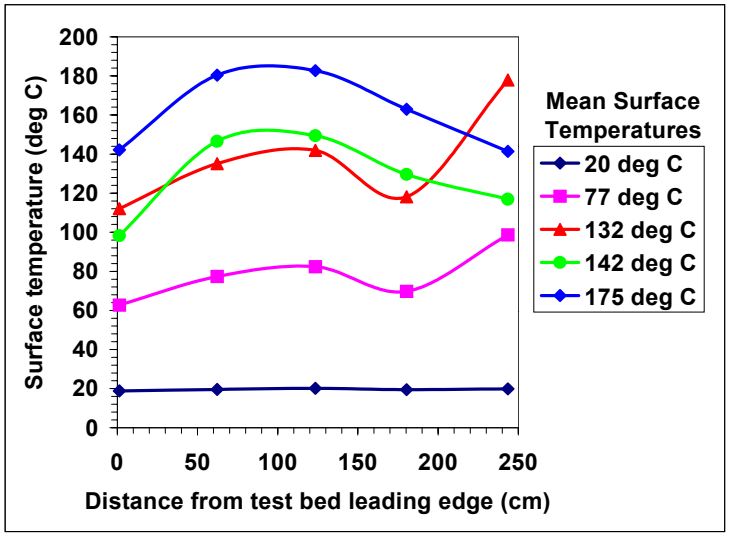

Figure 4.21: Surface temperature distributions for five sets of boundary layer profiles over Test Bed 2 maintained at the same freestream wind speed of about 85 m/s.

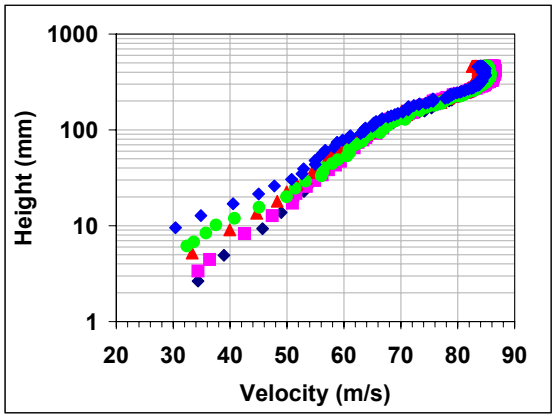

Figure 4.22: Resulting vertical wind profiles for a range of surface temperature conditions over Test Bed 2 at the same wind speed of approximately 85 m/s.

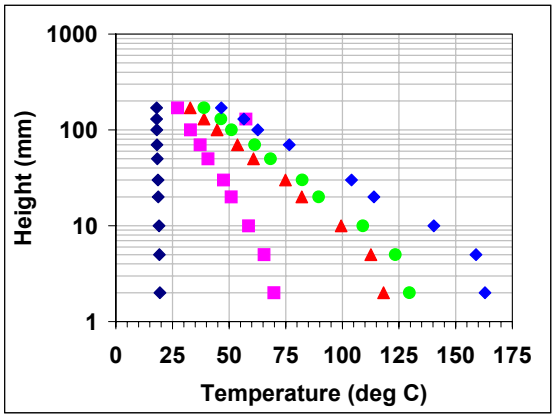

Figure 4.23: Resulting vertical temperature profiles for a range of surface temperature conditions over Test Bed 2 at the same wind speed of approxiamtely 85 m/s.

4.7 Friction Speed and Skin-friction Coefficient Analysis

To identify dust threshold with a corresponding surface-to-wind condition, one must first decipher whether the physically simulated test bed configurations fall into an aerodynamically rough-wall or hydraulically smooth-wall turbulence or whether the resulting flow is still in transition. Such analysis will decide the appropriate method to

determine the two critical parameters in boundary-layer flow, friction speed, u^*, and local skin-friction coefficient, C_f' [Schlichting (1979)]. There were two different methods used to attempt to find these unknown variables. The first technique was to analyze the wind profiles over rough-wall flow. A second method involved analysis over smooth-wall flow. For this latter case, the profiles were analyzed using the so-called "Clauser Method" (1954).

Since unstable conditions generally overestimate the value for the roughness height, showing that the near-surface profiles are offset, friction speed and local skin friction coefficient estimates were only estimated from the unheated or neutral boundary-layer velocity profiles. These estimates later will be used to determine dust threshold conditions for both neutral and unstable atmospheric simulations.

4.7.1 Rough-Wall Analysis of Neutral Wind Profiles

In the process of estimating the roughness height, which was previously described in Chapter 4.6, a logarithmic-linear regression line of the points associated with the near-surface wind profile was generated giving a result in the form of Equation 4.6.1. Two coefficients, A_U and B_U, were found to define the specific profile. Rearranging this equation in the form shown in Equation 4.6.2, a comparison was made to the rough-wall "law-of-the-wall" formula given in Equation 4.6.3. Here, coefficient A_U was analogous to the roughness height, z_o, and the coefficient B_U to k/u^*, where k is the Von Kármán constant and u^* is the friction velocity. Therefore, based on a rough-wall estimation, the local skin-friction coefficient, C_f', may be determined as follows:

$$\text{By definition, } u^* = U_F \sqrt{\frac{C_f'}{2}} \tag{4.7.1}$$

$$\text{or, } C_f' = 2\left(\frac{u^*}{U_F}\right)^2 \tag{4.7.2}$$

Figures 4.24, 4.25, and 4.26 present the rough-wall estimates of friction speeds and skin-friction coefficients for Test Bed 1, Test Bed 2, and Test Bed 3, respectively, plotted as a function of the corresponding freestream wind speeds along with linear trendlines for the u^* values and polynomial fits for the C_f' values. Such results also are tabulated in Tables 4.17, 4.18, and 4.19 along with the corresponding roughness Reynolds numbers. Here, the roughness Reynolds number is defined as follows:

$$Re_{z_o} = \frac{u^* z_o}{\nu} \tag{4.7.3}$$

where u^* is the rough-wall estimated friction speed, z_o is the mean roughness height over the test bed configuration, and ν is the average kinematic viscosity calculated for the particular boundary-layer profile run.

Note that for Test Bed 1 and Test Bed 2, the rough-wall estimated C_f' values decrease as a function of decreasing wind speeds. These observed trends are incorrect since, by definition, surface drag, hence skin-friction, must increase for lower Reynolds numbers. Thus, rough-wall estimates of u^* and C_f' over Test Bed 1 and Test Bed 2 are invalid. However, the plots of rough-wall estimated skin-friction coefficient versus mean wind speed of Test Bed 3, the rougher surface configuration, reveals a closer agreement for rough-wall turbulence than Test Bed 1 or Test Bed 2.

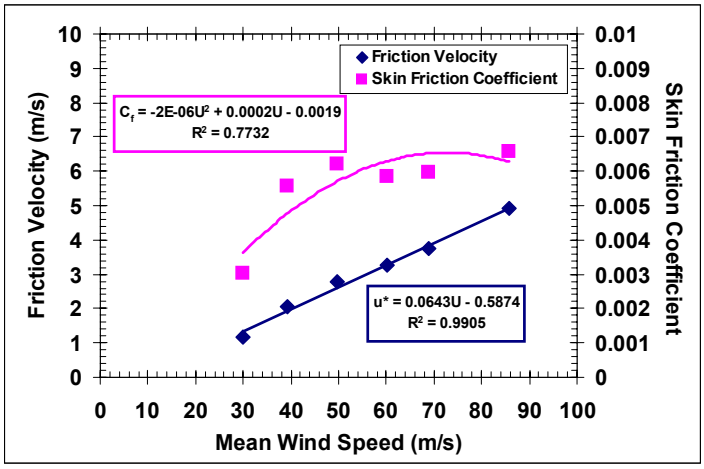

Figure 4.24: Friction speed and skin friction coefficients estimated from boundary-layer surveys over Test Bed 1 based on rough-wall analysis.

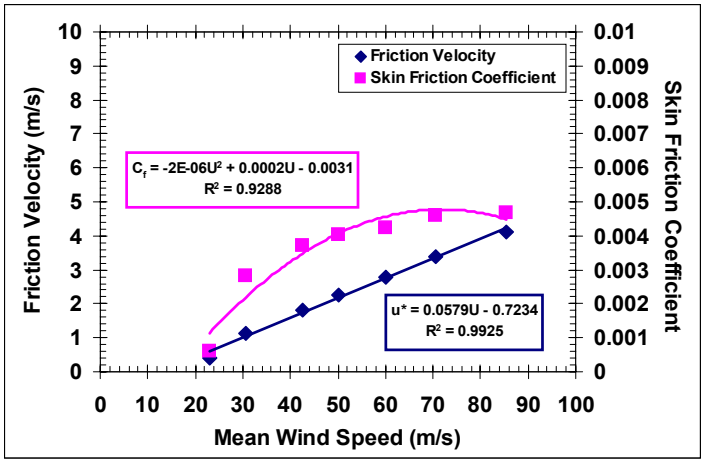

Figure 4.25: Friction speed and skin friction coefficients estimated from boundary-layer surveys over Test Bed 2 based on rough-wall analysis.

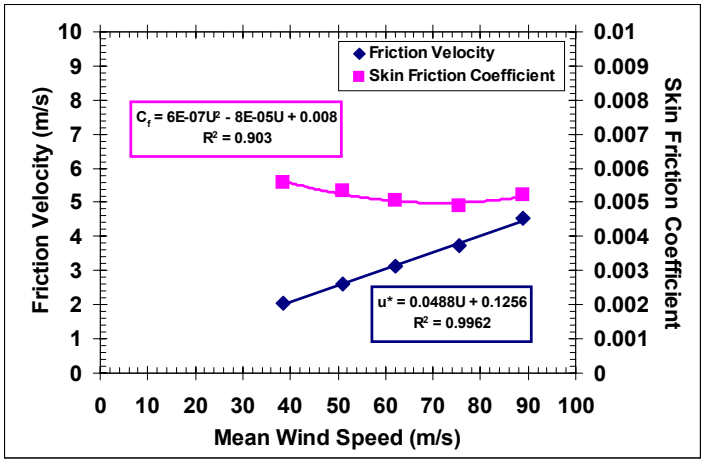

Figure 4.26: Friction speed and skin friction coefficients estimated from boundary layer surveys over Test Bed 3 based on rough-wall analysis.

Table 4.17: Calculated friction speeds, skin friction coefficients, and roughness Reynolds number for the unheated wind profiles over Test Bed 1 based on rough-wall analysis.

Wind Tunnel Speed (m/s)	Friction Speed (m/s)	Skin Friction Coefficient	Roughness Reynolds Number
30.03	1.17	0.00303	0.11
39.27	2.07	0.00555	0.20
49.81	2.78	0.00623	0.27
60.04	3.25	0.00585	0.32
68.97	3.77	0.00597	0.37
85.70	4.92	0.00659	0.47

Table 4.18: Calculated friction speeds, skin friction coefficients, and roughness Reynolds number for the unheated wind profiles over Test Bed 2 based on rough-wall analysis.

Wind Tunnel Speed (m/s)	Friction Speed (m/s)	Skin Friction Coefficient	Roughness Reynolds Number
22.96	0.41	0.00062	0.02
30.56	1.15	0.00281	0.07
42.58	1.83	0.00369	0.11
50.18	2.26	0.00404	0.14
60.13	2.77	0.00425	0.17
70.64	3.39	0.00461	0.21
85.53	4.13	0.00466	0.25

Table 4.19: Calculated friction speeds, skin friction coefficients, and roughness Reynolds number for the unheated wind profiles over Test Bed 3 based on rough-wall analysis.

Wind Tunnel Speed (m/s)	Friction Speed (m/s)	Skin Friction Coefficient	Roughness Reynolds Number
38.47	2.03	0.00558	0.24
50.88	2.63	0.00534	0.31
61.97	3.11	0.00505	0.37
75.50	3.73	0.00489	0.45
88.98	4.54	0.00521	0.55

Although C_f' and u^* of Test Bed 3 seem to correspond to a rough-wall regime, the unusually low values of roughness Reynolds number prove otherwise. Based on the resulting values of u^* from the rough-wall analysis, plots were generated to show the non-dimensional velocity, u^+, as a function of the logarithm of the local Reynolds

number, $log_{10}\ y^+$, for each of the wind profiles collected over the three test bed configurations (see Figures 4.27, 4.28, and 4.29). By definition, u^+ and $log_{10}\ y^+$ are calculated as follows:

$$u^+ = \frac{U}{u*} \tag{4.7.4}$$

$$log_{10}\ y^+ = log_{10}\frac{u*z}{\nu} \tag{4.7.5}$$

Here, U is the local velocity measured at the corresponding local height, z. On the same graph, the experimental non-dimensional plots are compared to the boundaries for a hydraulically smooth-wall flow, the upper dashed line, and completely rough-wall flow, the lower dashed line. Equations for generating these boundaries were obtained from Schlichting (1979) for boundary layer flow.

Non-dimensional plots for Test Bed 1 and Test Bed 2, Figures 4.27 and 4.28 respectively, additionally support the previous deduction that flows over such surfaces are not aerodynamically rough-wall turbulence flow. Note that plots for some of the higher Reynolds number settings fall between the boundaries for smooth and rough-wall flow, while the lowest speeds predict profiles above the smooth-wall boundary. According to Schlichting (1979), such profiles do not exist beyond the smooth-wall boundary. Ideally, if the wind-tunnel conditions generate smooth-wall flow, the profiles from all Reynolds number conditions should fall onto the smooth-wall boundary. Though the skin-friction trends over Test Bed 3 presumed a trend for a rough-wall regime, Figure 4.29 shows that the neutral wind profiles are in transition from smooth to rough.

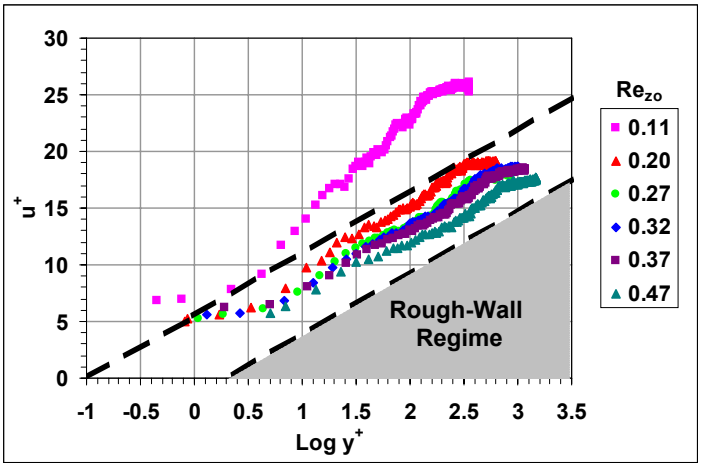

Figure 4.27: Non-dimensional velocity as a function of the log of local Reynolds number from the rough-wall analysis of the neutral wind profiles conducted over Test Bed 1.

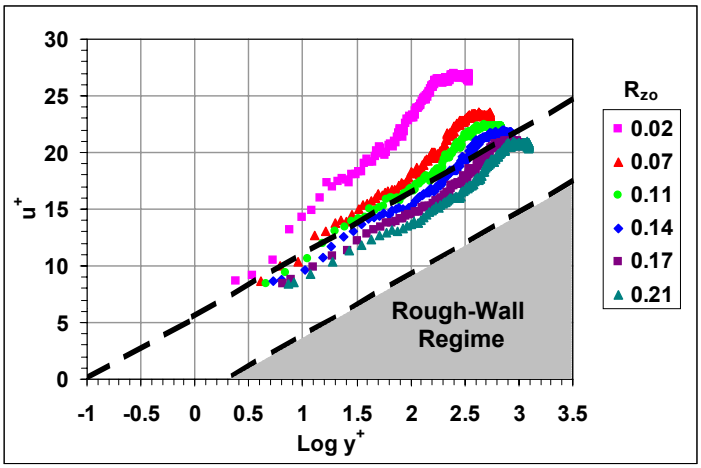

Figure 4.28: Non-dimensional velocity as a function of the log of local Reynolds number from the rough-wall analysis of the neutral wind profiles conducted over Test Bed 2.

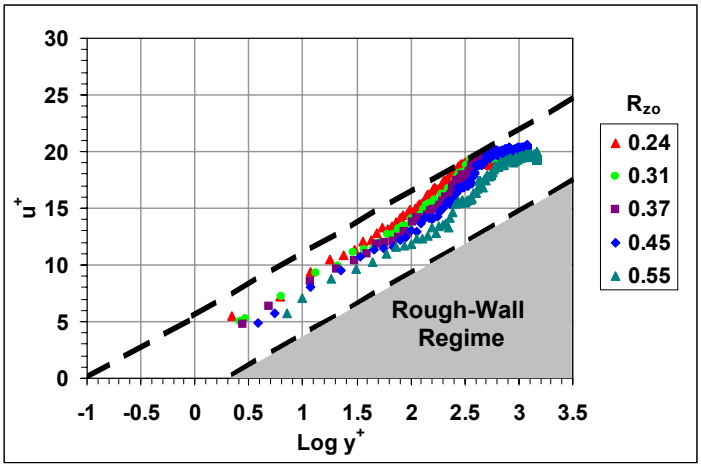

Figure 4.29: Non-dimensional velocity as a function of the log of local Reynolds number from the rough-wall analysis of the neutral wind profiles conducted over Test Bed 3.

4.7.2 Smooth-Wall Analysis of Neutral Wind Profiles

Smooth-wall analysis of the neutral wind-profiles was based on a technique defined by Clauser (1954). Instead of initially calculating for the friction velocity, the skin friction coefficient is iterated graphically until the wind profiles non-dimensionally portray hydraulically smooth flow. In order to accomplish such a task, an initial guess of C_f for each wind profile was first made so that u^* can be calculated as follows:

$$u^* = U_F \sqrt{\frac{C_f}{2}} \tag{4.7.7}$$

With this friction speed, the corresponding plot of non-dimensional velocity profile, u^+, as a function of local Reynolds number, y^+, on a linear-to-logarithm scale was generated for each wind profile. The data plotted in solid red triangles in Figure 4.30 shows a sample profile corresponding with the left and lower axis scales. It is then compared to Schlichting's equation for a smooth profile, which is shown as the dashed black line, and to Spalding's equation for smooth wall, displayed as a solid black line. Additionally plotted in Figure 4.30 is U/U_F versus $U_F z/\nu$, represented in hollow red triangles and compared to a solid red line of the initial guess for a constant C_f. Both of these graphs correspond to the upper and right axis scales. These are essentially the plots pertaining to the Clauser smooth-wall method. Derived in Appendix F, the key equations used for this technique are as follows:

$$\frac{U}{U_F} = \sqrt{\frac{C_f}{2}} \left[\frac{1}{k} \left(\frac{ln_e 2}{log_{10} 2} \right) log_{10} \left(\frac{U_F z}{\nu} \sqrt{\frac{C_f}{2}} \right) + 5.45 \right] \tag{4.7.8}$$

$$\frac{U_F z}{\nu} = log_{10}^{-1} \left[k \left(\frac{log_{10} 2}{ln_e 2} \right) \left(\frac{U/U_F}{\sqrt{C_f/2}} - 5.45 \right) - log_{10} \sqrt{\frac{C_F}{2}} \right] \tag{4.7.9}$$

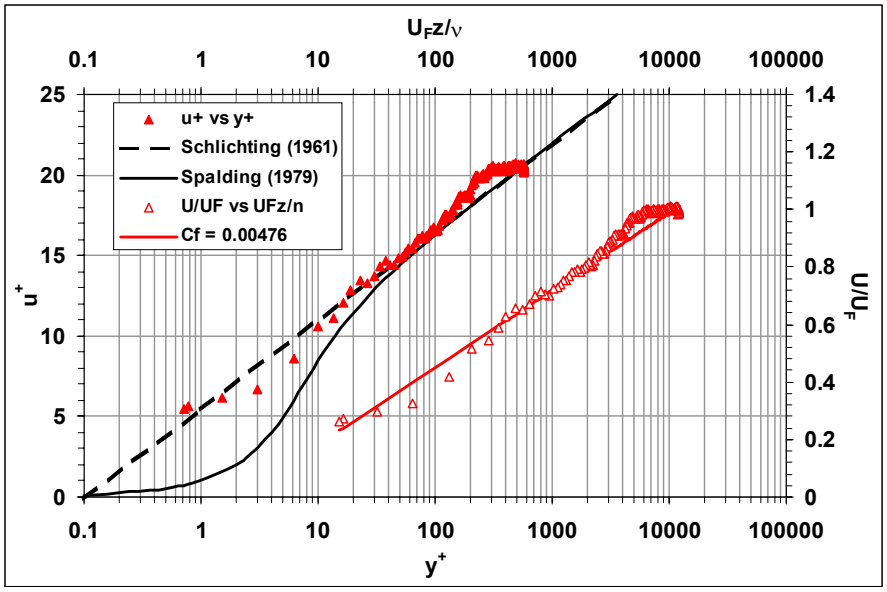

Figure 4.30: Sample plot of non-dimensional velocities as a function of local Reynolds numbers over Test Bed 1 for the Clauser smooth-wall boundary layer analysis.

In general, the goal of the smooth-wall analysis technique is to iterate for C_f until the experimental non-dimensional data in a plot such as Figure 4.30 converges to the Schlichting and Spalding representations for smooth-wall flow. Spalding's smooth-wall curve equation was obtained from White, F.M. (1991). At the same time a certain portion of the Clauser data in Figure 4.30 should also converges logarithmic-linearly to the line of constant C_f. Upon final iteration, the plot of u^+ versus $log_{10}\, y^+$ from each wind profile should converge onto the boundary for smooth-wall flow (see Figures 4.31, 4.32, and 4.33).

Thus, the smooth-wall results of friction speeds and the iterated skin-friction coefficients for the three surface configurations are plotted as a function of the corresponding mean wind speed in Figures 4.34, 4.35, and 4.36. These results are tabulated in Tables 4.20, 4.21, and 4.22 with the corresponding roughness Reynolds number values. The figures also provide the linear and polynomial regression line equations for the friction speed and skin-friction coefficients plots, respectively.

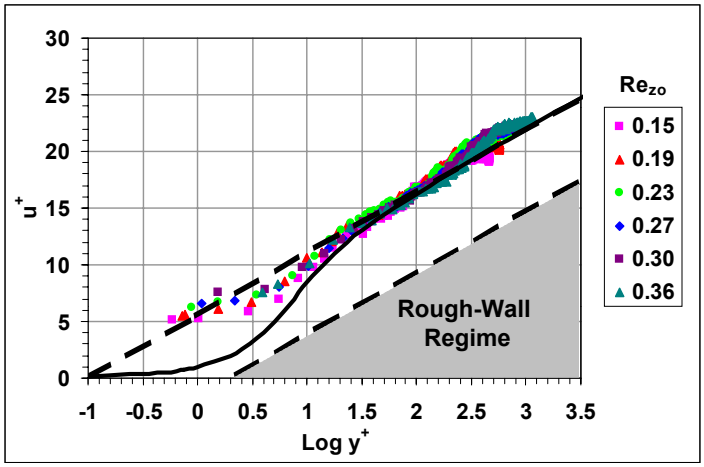

Figure 4.31: Non-dimensional velocity as a function of the log of local Reynolds number from the smooth-wall analysis of the neutral wind profiles conducted over Test Bed 1.

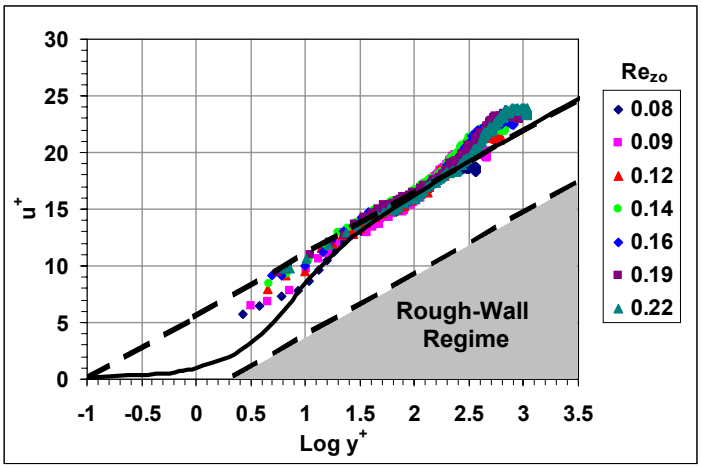

Figure 4.32: Non-dimensional velocity as a function of the log of local Reynolds number from the smooth-wall analysis of the neutral wind profiles conducted over Test Bed 2.

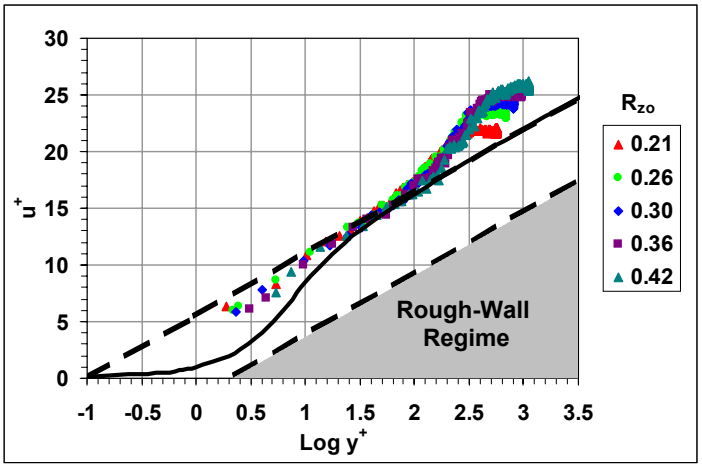

Figure 4.33: Non-dimensional velocity as a function of the log of local Reynolds number from the smooth-wall analysis of the neutral wind profiles conducted over Test Bed 3.

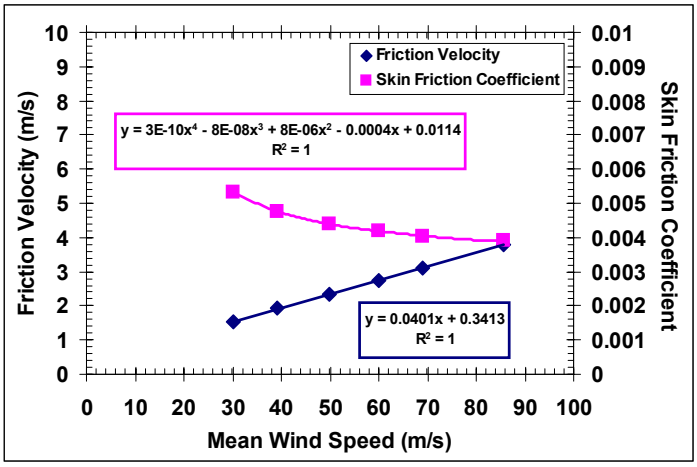

Figure 4.34: Friction speeds and skin friction coefficients estimated from boundary-layer surveys over Test Bed 1 based on smooth-wall analysis.

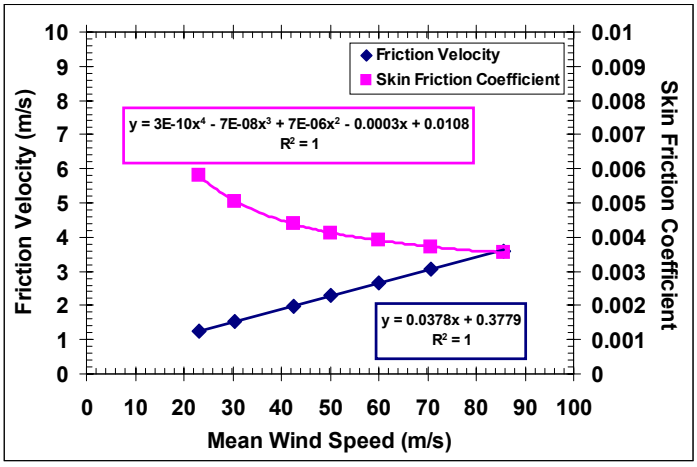

Figure 4.35: Friction speeds and skin friction coefficients estimated from boundary-layer surveys over Test Bed 2 based on smooth-wall analysis.

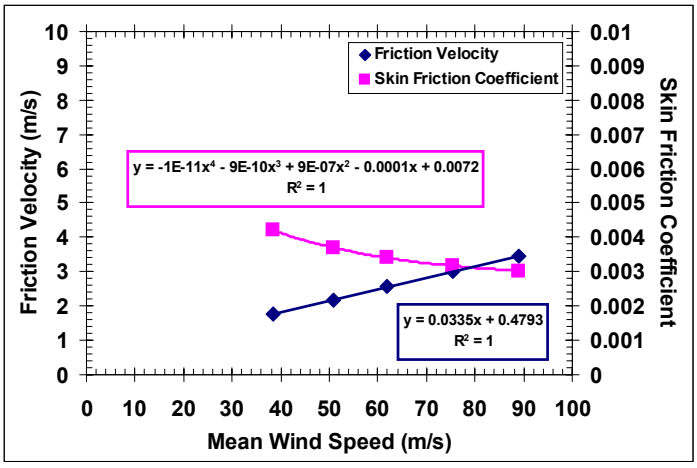

Figure 4.36: Friction speeds and skin friction coefficients estimated from boundary-layer surveys over Test Bed 3 based on smooth-wall analysis.

Table 4.20: Calculated friction speeds, skin friction coefficients, and roughness Reynolds number for the unheated wind profiles over Test Bed 1 based on smooth-wall analysis.

Wind Tunnel Speed (m/s)	Skin Friction Coefficient	Friction Speed (m/s)	Roughness Reynolds Number	Wind Tunnel Reynolds Number
30.03	0.00534	1.55	0.15	132781
39.27	0.00476	1.92	0.19	174537
49.81	0.00439	2.33	0.23	224817
60.04	0.00419	2.75	0.27	269385
68.97	0.00405	3.10	0.30	305304
85.70	0.00390	3.78	0.36	372708

Table 4.21: Calculated friction speeds, skin friction coefficients, and roughness Reynolds number for the unheated wind profiles over Test Bed 2 based on smooth-wall analysis.

Wind Tunnel Speed (m/s)	Skin Friction Coefficient	Friction Speed (m/s)	Roughness Reynolds Number	Wind Tunnel Reynolds Number
22.96	0.00580	1.24	0.08	100293
30.56	0.00506	1.54	0.09	133314
42.58	0.00438	1.99	0.12	185707
50.18	0.00413	2.28	0.14	221101
60.13	0.00390	2.66	0.16	265333
70.64	0.00372	3.05	0.19	311994
85.53	0.00356	3.61	0.22	375126

Table 4.22: Calculated friction speeds, skin friction coefficients, and roughness Reynolds number for the unheated wind profiles over Test Bed 3 based on smooth-wall analysis.

Wind Tunnel Speed (m/s)	Skin Friction Coefficient	Friction Speed (m/s)	Roughness Reynolds Number	Wind Tunnel Reynolds Number
38.47	0.00420	1.76	0.21	174523
50.88	0.00370	2.19	0.26	230976
61.97	0.00340	2.56	0.30	281155
75.50	0.00317	3.01	0.36	343977
88.98	0.00302	3.46	0.42	408744

In the following section, analysis will show that for Test Bed 3, the calculated skin friction coefficients based on "Clauser's technique" fall below the accepted smooth wall curve (Schlichting, 1979) for the range of wind tunnel Reynolds numbers. Thus, the surface condition results from the smooth-wall analysis of Test Bed 3 are not correct.

4.7.3 Comparison between Rough-Wall and Smooth-Wall Analysis

Based on the rough-wall analysis, only results from Test Bed 3 revealed a reasonable decreasing trend of C_f as a function of mean wind speed. According to the smooth-wall analysis, all three test-bed configurations generated valid trends of C_f with wind speed. In order to determine which method appropriately predicts the surface shear stress over each of the test bed settings, the estimated values of C_f from the two analytical methods were compared to the smooth-wall and rough-wall bounds, according to Figure 4.37, obtained from Schlichting (1979). In this plot, values of skin-friction do not exist below the smooth-wall curve.

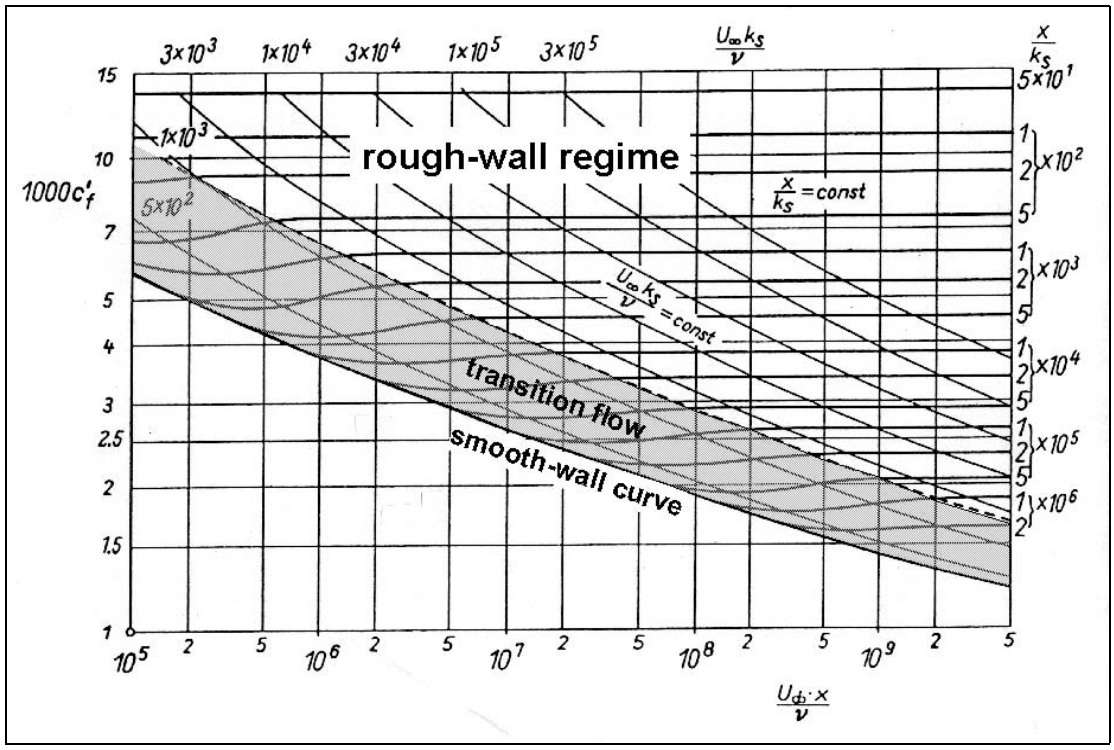

Figure 4.37: Graph of skin-friction coefficient as a function of downstream Reynolds number obtained from Schlichting (1979).

Figures 4.38, 4.39, and 4.40 present a comparison of the rough-wall and smooth-wall C_f estimates as a function of the test section Reynolds number, Re_x, along with Schlichting's smooth-wall curve and the boundary for the rough-wall regime.

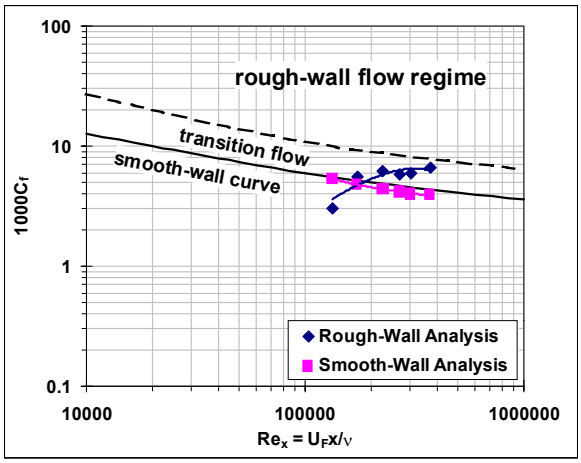

Figure 4.38: Comparison of skin friction trends for a range of wind tunnel Reynolds numbers from the rough-wall and smooth-wall analysis techniques for Test Bed 1.

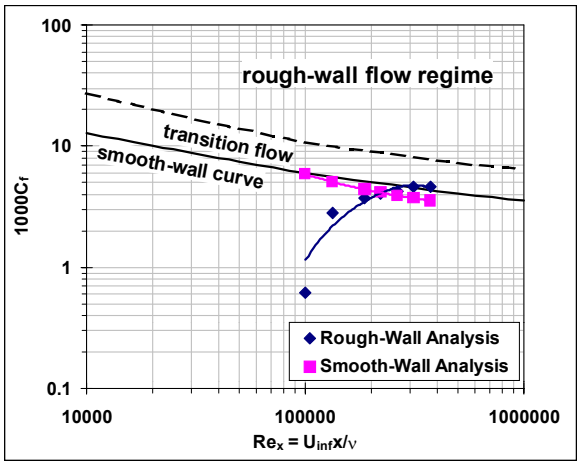

Figure 4.39: Comparison of skin friction trends for a range of wind tunnel Reynolds numbers from the rough-wall and smooth-wall analysis techniques for Test Bed 2.

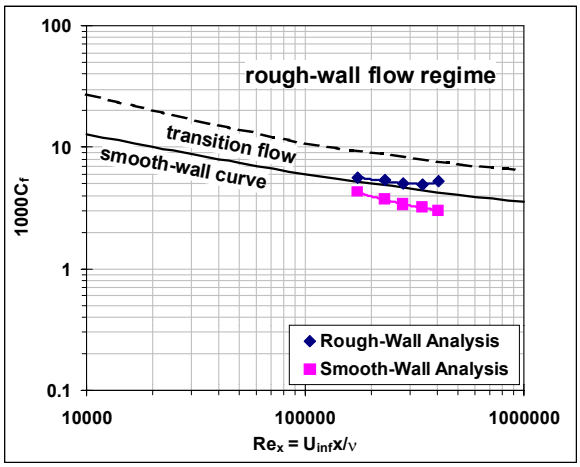

Figure 4.40: Comparison of skin friction trends for a range of wind tunnel Reynolds numbers from the rough-wall and smooth-wall analysis techniques for Test Bed 3.

According to Figures 4.38 and 4.39, flow over Test Bed 1 and Test Bed 2 fall just below, although generally agree, with the smooth-wall curve. Thus, for within uncertainty in the measurements, threshold conditions over these surface configurations may be estimated using Schlichting's smooth-wall curve since threshold values should not be less than the smooth-wall curve. Flow over Test Bed 3, however, is not a smooth-wall situation. It appears to be in the transitional flow region of the Schlichting chart. Here, neither smooth nor rough-wall estimates would be strictly valid. However, the rough-wall estimates are probably close to the actual value since in transitional flow, the flow trends tend to look more like rough-wall flow than smooth-wall flow. Therefore, C_f' values were estimated from the "law-of-the-wall" equation of the near surface profiles.

4.8 MARSWIT Stability Conditions

Stability conditions are designated by the value of the Richardson number, *Ri*. Based on the measurements conducted during the experiments, values of the bulk Richardson number were determined for the boundary-layer surveys and for threshold. The version of the bulk Richardson number applied was that defined in Golder (1972), although a slight wind tunnel variation was made.

There are several forms of the Richardson number, *Ri*. The most fundamental form is the flux Richardson number, Ri_f. A general equation for Ri_f can be found in Stull (1988). However, assuming planar homogeneity, no subsidence (i.e., the mean vertical velocity is zero), and the mean wind, $\overline{U}$, dominates the flow, the flux Richardson number in boundary-layer wind tunnel flows is defined as follows.

$$Ri_f = \frac{\frac{g}{\overline{\theta_v}}\left(\overline{w'\theta_v'}\right)}{\left(\overline{u'w'}\right)\frac{\delta \overline{U}}{\delta z}} \tag{4.8.1}$$

Unfortunately, Ri_f is a difficult stability parameter to calculate since it requires a multitude of simultaneous measurements at high sampling rates of the fluctuating horizontal velocity, u', the vertical velocity, w', and the fluctuating temperature, θ_v'. Even if the opportunity were to arise that such fluctuating parameters can be measured, the value of Ri_f will merely inform whether laminar flow will evolve, but not necessarily, turbulent flow will arise. This is primarily due to the inclusion of turbulent correlations in the Ri_f equation.

A second and more useful form of Ri is the gradient Richardson number, Ri_g. In this form, the mean correlation of vertical velocity and temperature fluctuations, $\overline{w'\theta_v'}$, is estimated as a vertical temperature gradient, $\partial\overline{\theta_v}/\partial z$, while the Reynolds stress, $\overline{u'w'}$, is given as the vertical velocity gradient, $\partial\overline{U}/\partial z$. Again assuming wind-tunnel conditions, Ri_g is defined according to the following equation (Stull, 1988).

$$Ri_g = \frac{g}{\overline{\theta_v}} \cdot \frac{\partial\overline{\theta_v}/\partial z}{\left(\partial\overline{U}/\partial z\right)^2} \tag{4.8.2}$$

A final form of the stability parameter is the bulk Richardson number, Ri_B. In this case, the gradients in the gradient Richardson number equation are estimated as differentials. Thus, in the wind tunnel, Ri_B is defined as follows (Stull, 1988).

$$Ri_B = \frac{g}{\overline{\theta_v}} \cdot \frac{\Delta\overline{\theta_v}\Delta z}{\left(\Delta\overline{U}\right)^2} \tag{4.8.3}$$

The most critical step in calculating Ri_B is that the differentials are calculated over the same particular finite layer, where $\overline{\theta_v}$ the mean potential temperature within the layer in question. Ri_B is essentially a general description of stability for a thin finite difference layer.

There are several forms of the bulk *Ri*. One is given as the surface-layer bulk *Ri* (Zoumakis and Kelessis, 1991), and defined as:

$$Ri_{B_S} = \frac{g}{\overline{\theta_{v_o}}} \cdot \frac{\left(\overline{\theta_{v_2}} - \overline{\theta_{v_o}}\right)\left(z_2 - z_o\right)}{\overline{U_2}} \tag{4.8.4}$$

In this version, the virtual potential temperature at the roughness height, z_o, is required. Another version of the bulk *Ri* is the low-lying bulk *Ri*, presented by Wang (1981), and is given as:

$$Ri_{B_L} = \frac{g}{\overline{\theta_{v_2}}} \cdot \frac{z_2}{\overline{U_2}^2} \cdot \left(\overline{\theta_{v_2}} - \overline{\theta_{v_1}}\right) \tag{4.8.5}$$

Finally, a third variation of the bulk *Ri*, obtained from Golder (1972), appears to be the crudest estimate for a thick layer. This bulk Ri is given as follows.

$$B = \frac{g}{\overline{\theta_{v_{\bar{z}}}}} \cdot \frac{\left(\overline{\theta_{v_2}} - \overline{\theta_{v_1}}\right) / \left(z_2 - z_1\right)}{\overline{U_{\bar{z}}}^2} \cdot \bar{z}^2 \tag{4.8.6}$$

$$\text{where: } \bar{z} = \sqrt{z_1 z_2} \tag{4.8.7}$$

Here, the mean virtual potential temperature and the mean dominant velocity are taken from the mean geometric height $\bar{z}$.

Stability conditions for the experiments in this study were described by a modified version of the bulk Richardson number given by Golder (1972). Instead of using the mean geometric height, the bulk *Ri* was calculated for the height range between

some near surface height, z_1, and the height of the boundary layer, δ. Accordingly, the pertinent mean wind speed and mean virtual potential temperature also were taken from the corresponding height range. Figure 4.41 presents the modified version of the bulk Richardson number calculated in this study along with an illustration of where certain parameters were taken.

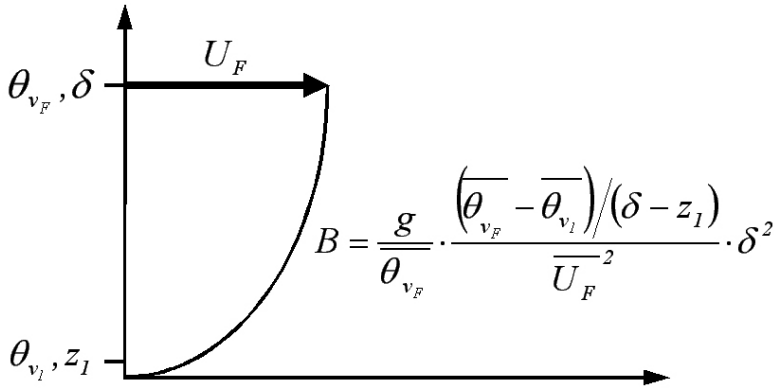

$$B = \frac{g}{\overline{\theta_{v_F}}} \cdot \frac{\left(\overline{\theta_{v_F}} - \overline{\theta_{v_l}}\right) / \left(\delta - z_1\right)}{\overline{U_F}^2} \cdot \delta^2 \qquad (4.8.8)$$

Figure 4.41: Bulk Richardson number version used for experiments in current study.

Recall the boundary-layer profiles (Figures 4.22 and 4.23) for the given surface temperature distributions in Figure 4.21 conducted over Test Bed 2 at about *85 m/s*. The following Figure 4.42 presents the corresponding values of stability based on four versions of the bulk Richardson number. As expected, bulk *Ri* decreases with increasing surface temperature. Note that the finite-difference layer bulk Ri calculation given by Stull (1988) denotes an upturn at approximately *142 °C*. The low-lying bulk *Ri* values given by Wang (1981) also indicate a slight upturn at the same mean surface temperature reading. Such trends typically show that the bulk Ri is sensitive to the thickness of layer in which it is calculated. Values of the bulk *Ri* given by Golder (1972) and its modified version given in Equation 4.8.8 does not capture the specific stability condition for a particular layer, but it does show a steady decreasing linear variation with increasing temperature. Thus, calculation of the bulk Ri based on a thicker layer gives a reasonable

valid representation of stability. In particular, for the wind tunnel experiments, use of Equation 4.8.8 can result to a representative value of stability for the entire test section boundary layer.

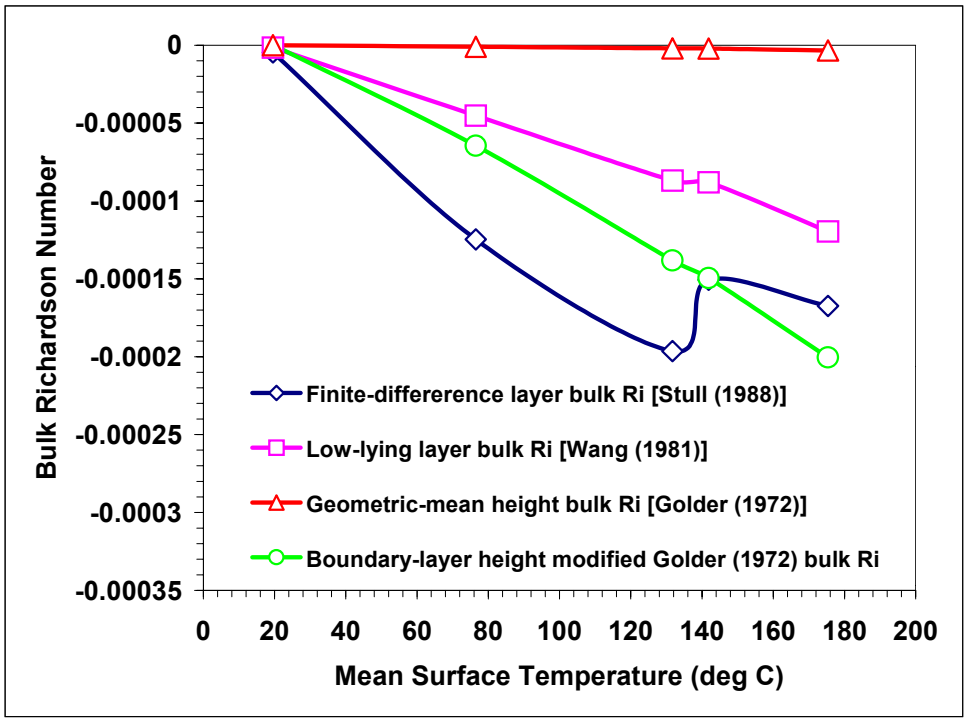

Figure 4.42: Corresponding calculations of the various versions of the bulk Richardson number for boundary layer profiles collected at about 85 m/s for a range of surface temperature distributions over Test Bed 2.

While Figure 4.42 shows the variation of the bulk *Ri* for constant wind and changing surface temperature, Figure 4.43 presents the resulting bulk *Ri* values for constant surface temperatures and varying freestream wind speeds. For neutral stability conditions in MARSWIT, the bulk Richardson number expectedly converges to an "ideally neutral stability" value for all wind tunnel freestream speeds. However, once the surface is heated, the bulk *Ri* value negatively increases non-linearly with decreasing freestream wind speed. As the wind speed is increased, the bulk Ri approaches the "ideally neutral stability" condition. Thus, in MARSWIT, buoyant boundary-layer flow can be suppressed by increasing wind shear.

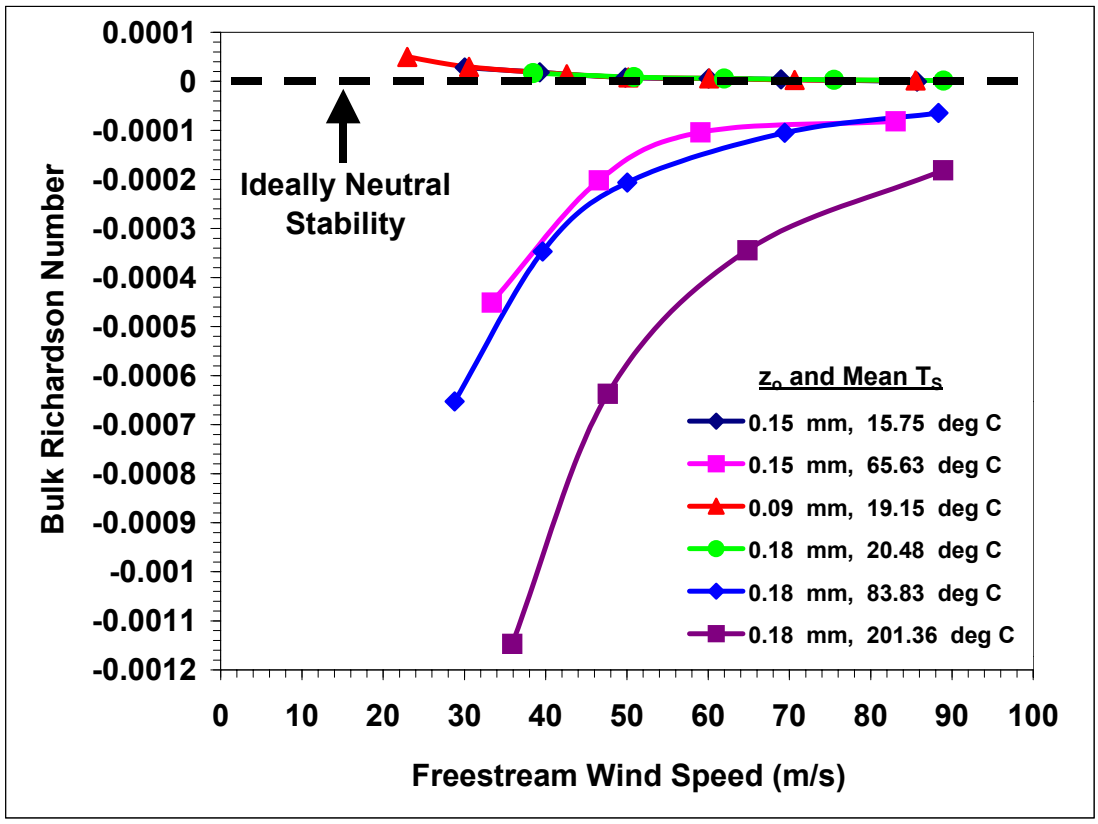

Figure 4.43: Corresponding bulk Richardson number for a range of freestream wind speeds at various surface-heating levels over the three test surface configurations.

4.9 MARSWIT Dust Threshold

Dust threshold was determined from the signals given by the electrometer particle impaction probe. Upon indication of dust movement, corresponding values of the wind tunnel freestream velocity and rake and surface temperatures were determined. Figure 4.44 through Figure 4.53 display the experimental time indication of dust threshold (i.e., the vertical line represents threshold condition in each graph) and the corresponding freestream wind speed determined for each dust threshold run over the three test surface configurations. The corresponding wind-tunnel conditions at the time of threshold for the three test bed configurations are given in the following Table 4.23.

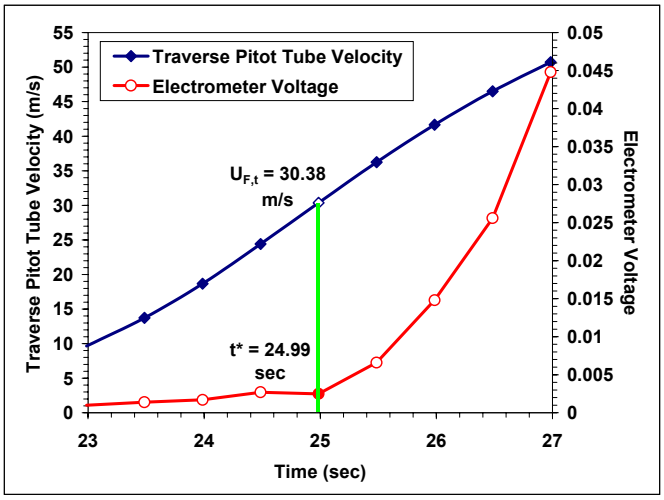

Figure 4.44: Dust threshold indication over Test Bed 1 at 20.30 °C mean surface temperature.

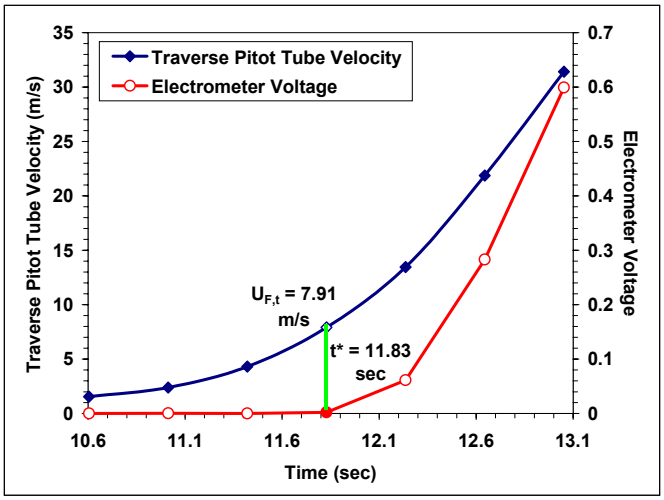

Figure 4.45: Dust threshold indication over Test Bed 1 at 117.56 °C mean surface temperature.

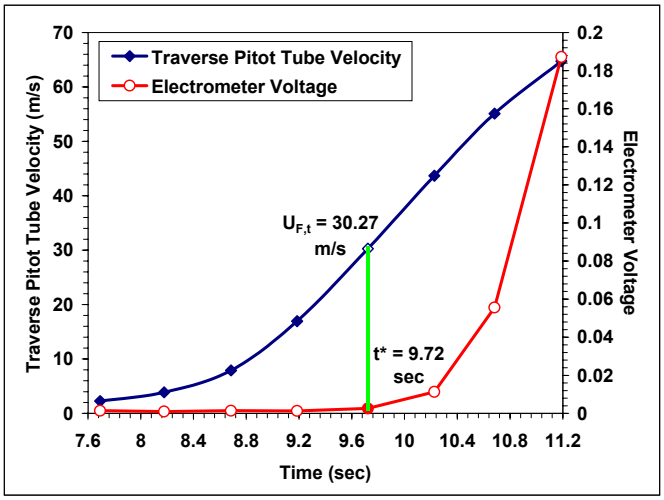

Figure 4.46: Dust threshold indication over Test Bed 2 at 20.05 °C mean surface temperature.

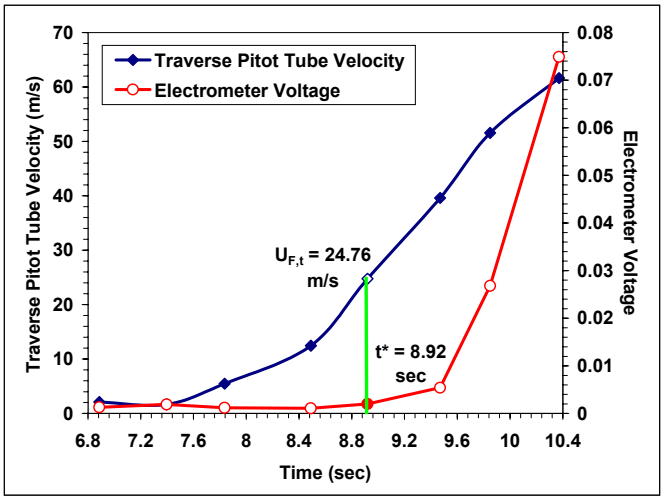

Figure 4.47: Dust threshold indication over Test Bed 2 at 76.92 °C mean surface temperature.

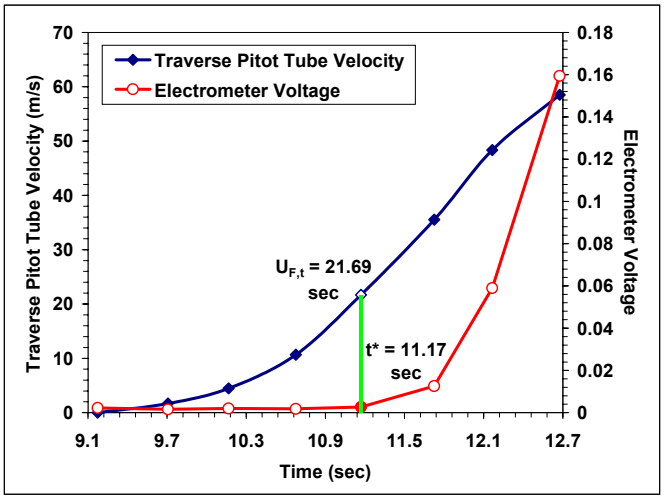

Figure 4.48: Dust threshold indication over Test Bed 2 at 125.35 °C mean surface temperature.

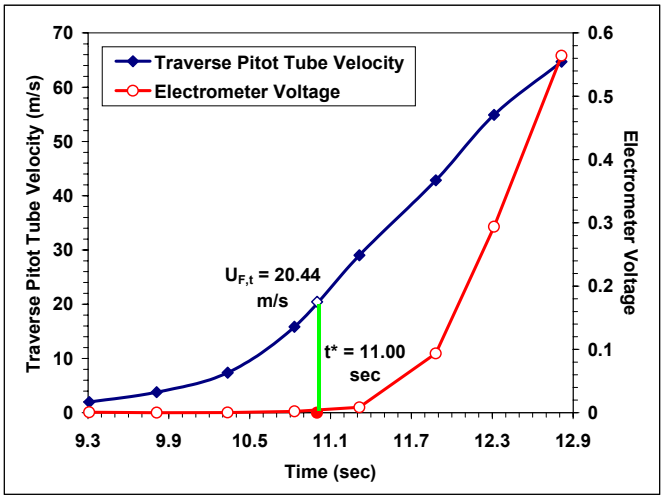

Figure 4.49: Dust threshold indication over Test Bed 2 at 150.27 °C mean surface temperature.

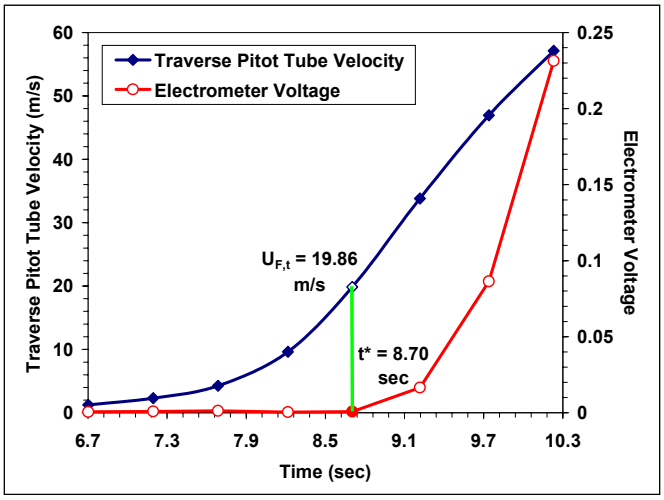

Figure 4.50: Dust threshold indication over Test Bed 2 at 174.97 °C mean surface temperature.

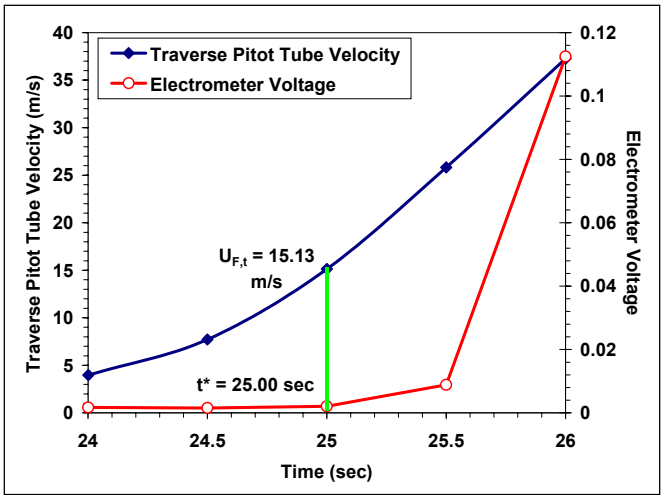

Figure 4.51: Dust threshold indication over Test Bed 3 at 20.67 °C mean surface temperature.

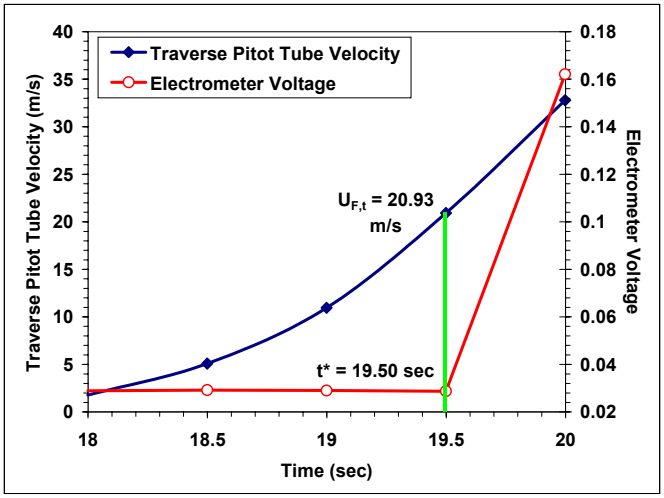

Figure 4.52: Dust threshold indication over Test Bed 3 at 83.54 °C mean surface temperature.

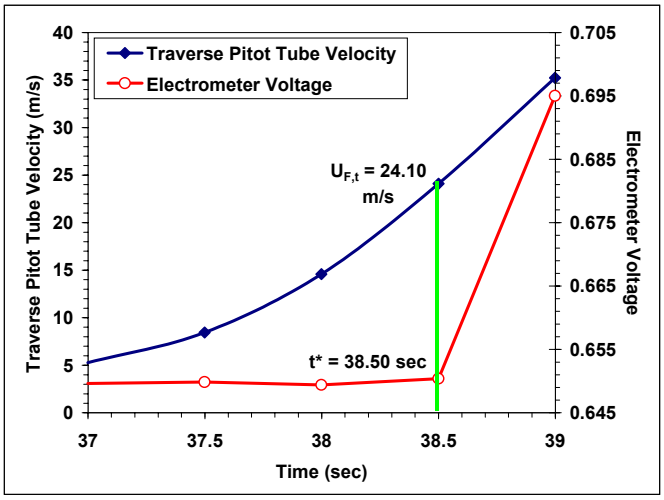

Figure 4.53: Dust threshold indication over Test Bed 3 at 200.96 °C mean surface temperature.

Table 4.23: Corresponding boundary-layer conditions at the time of threshold for particular stability conditions over the three test bed configurations.

Test Surface Designation	Roughness Height (mm)	Mean Surface Temperature (°C)	Bulk Richardson Number	Threshold Freestream Speed (m/s)	Threshold Friction Speed (m/s)	Threshold Skin Friction Coefficient
Test Bed 1	0.15	20.30	≈ 0	30.38	1.63	0.0057
		117.56	-0.0137	7.91		0.0846
Test Bed 2	0.09	20.05	≈ 0	30.27	1.61	0.0057
		76.92	-0.0009	24.76		0.0085
		125.35	-0.0019	21.69		0.0111
		150.27	-0.0025	20.44		0.0125
		174.97	-0.0034	19.86		0.0132
Test Bed 3	0.18	20.67	≈ 0	15.13	0.77	0.0051
		83.54	-0.0012	20.93		0.0027
		200.96	-0.0024	24.10		0.0020

As the optimum result of the study, Table 4.23 presents the wind-tunnel freestream speed at dust threshold for each boundary layer stability condition in terms of the bulk *Ri* calculated for the threshold experiments conducted over the three test surface conditions. Recall that the z_o values of 0.15 mm, 0.09 mm, and 0.18 mm represent Test Bed 1, Test Bed 2, and Test Bed 3, respectively. Based on boundary-layer analysis over each of the test surfaces, dust threshold friction speeds over Test Bed 1 and Test Bed 2 were found using the smooth-wall bound given by Schlichting (1979) in Figure 4.37 and using the threshold freestream speed at neutral conditions. Threshold friction speeds over

Test Bed 3 were determined directly from the "law-of-the-wall" Equation 4.7.1 and again with the corresponding threshold freestream speed for that particular roughness condition at neutral stability conditions. Accordingly, the resulting skin-friction values for each threshold experiment then were calculated using Equation 4.7.2. Figure 4.54 displays the resulting threshold freestream wind speeds and the corresponding skin friction coefficients for each dust threshold test over the three test bed roughness configurations.

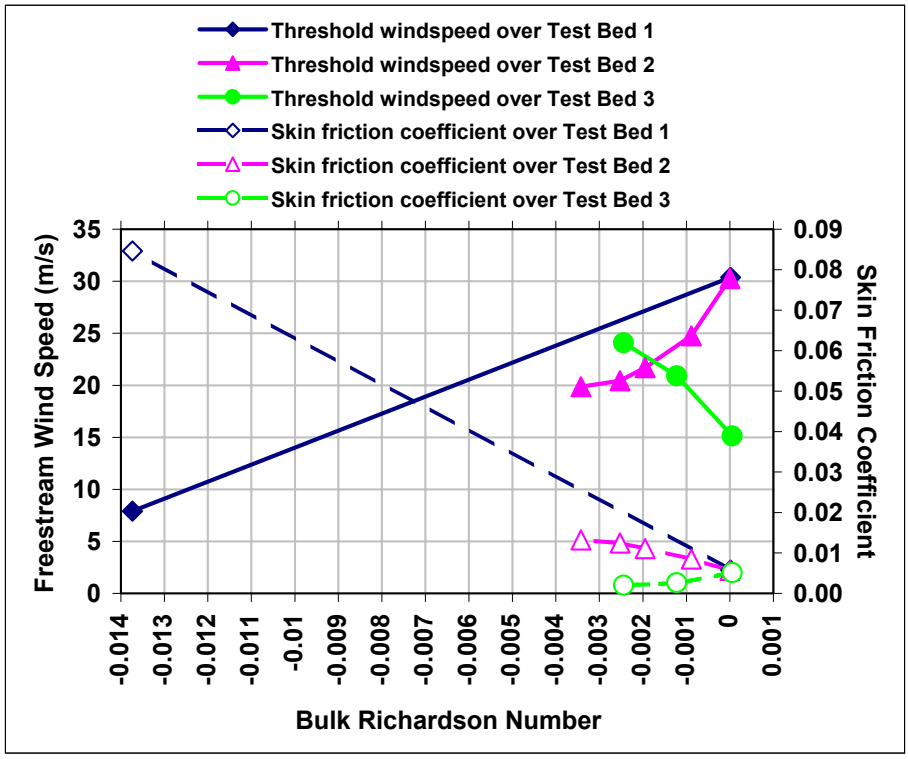

Figure 4.54: Estimated freestream wind speeds and corresponding skin friction coefficients at dust threshold for a range of stability conditions over the three test surface configurations.

According to Figure 4.54, results at neutral stability, where bulk $Ri \approx 0$, indicate that dust threshold occurs at a lower wind speed for rougher surfaces. Such is a valid outcome since increased roughness generates greater turbulence to instigate initial particle movement. Also, note that at neutral stability, dust threshold occurs at approximately the same skin-friction coefficient value. Thus, based on fundamental aerodynamics of particle lift [Bagnold (1954), Fuchs (1964), Saffman (1965), White

(1986), Pye (1987), and Seinfeld And Pandis (1998)], threshold for CRC dust of *1* to *2* μm in diameter range, occurs at about a C_f' value of *0.0057* (see Table 4.23).

As theorized, Figure 4.54 also shows that dust suspension may be initiated at threshold speeds lower than that at neutral stability when subjected to an unstable boundary layer condition, but only for aerodynamically smooth surfaces over Test Bed 1 and Test Bed 2. Alternatively, the rougher condition over Test Bed 3 revealed an opposite effect. Even though the roughness heights over Test Bed 1 (the surface with the rippled sandpaper) and Test Bed 3 (the surface with the steel nuts) are nearly similar, Test Bed 1 generated the predicted trend, while the threshold wind speed conversely increased over Test Bed 3. Thus, for transitional or rough-wall flow, threshold increases with surface heating. This is an unexpected result, which may be due to an alteration of interparticle forces by the surface conductivity of the steel nuts.

Figures 4.55, 4.56, and 4.57 are photos of the test section surfaces over Test Bed 3 after dust threshold experiments conducted at bulk $Ri \approx 0$, *-0.0012*, and *–0.0024*, respectively. Comparison of these photos generally show that a greater amount of dust material was removed from the surface under the most unstable boundary layer condition, thus implying that dust threshold should have occurred at a lower wind speed for increased instability. Based on the opposite threshold trend from the nearly similar roughness condition over Test Bed 1, dust threshold may have been delayed over Test Bed 3 due to some type of a cohesive interaction caused by the heated steel nuts initially suppressing dust entrainment. Once movement of the top dust layer initiated due to the increased vertical turbulence, instabilities from convective heating along with other secondary mechanisms allowed the underlying dust to be easily entrained.

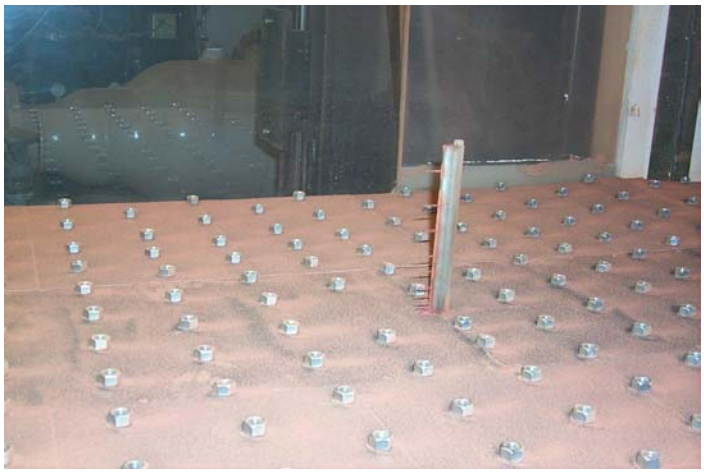

Figure 4.55: Photo of Test Bed 3 after a dust threshold experiment at bulk *Ri* ≈ *0* neutral boundary layer conditions.

Figure 4.56: Photo of Test Bed 3 after a dust threshold experiment at bulk *Ri* ≈ *-0.0012* unstable boundary layer conditions.

Figure 4.57: Photo of Test Bed 3 after a dust threshold experiment at bulk *Ri* ≈ *-0.0024* unstable boundary layer conditions.

Delayed dust threshold with increased surface heating over the roughest simulated surface of Test Bed 3 could possibly be due to increased electrostatic phenomena caused by the heating of the steel nuts (i.e., increases interparticle forces delaying threshold). The 32-grit sandpaper, used as the initial surface roughness, and the Carbondale Red Clay dust, used as the Martian surrogate particle-suspension media, were essentially composed of similar insulation type material. Recall, that the chemical names are respectively Al_2O_3 (aluminum oxide) and Al_2O_3-$2SiO_2$ (alumina silicate), thus implying that the heat capacities are essentially similar. The steel nuts, however, are of a conductive material, thus, when heated, its "free electrons" are excited, and with the wind-tunnel flow, "frictional charge" generates around the steel nuts, which becomes an attractive force against the surface dust [Zimon (1969), Ohanian, H.C. (1989)]. Such a condition essentially occurred for only a matter of seconds, since according to the photos in Figures 4.55, 4.56, and 4.57, a greater amount of dust material was removed from the higher heating cases. It seems that once dust threshold was reached, buoyancy effects generally dominated particle entrainment.

Chapter 5: Conclusion

Dust threshold measurements were performed over three sets of surface roughness conditions, $z_o = 0.015\ mm$, $0.09\ mm$, and $0.018\ mm$, respectively designated as Test Bed 1, Test Bed 2, and Test Bed 3. From boundary layer analysis of the velocity profiles under neutral conditions, it was determined that wind shear turbulence over the first two test surfaces corresponded to hydraulically smooth-wall flow, while the third roughness condition suggested that the boundary-layer flow was in transition from smooth to rough. Thus, using wind profiles collected at neutral conditions, corresponding dust threshold friction speeds for Test Bed 1 and Test Bed 2 were determined based on the smooth-wall curve given by Schlichting (1979). Although the flow was transitional, dust threshold friction speed over Test Bed 3 was determined according to the "law-of-the-wall" rough-wall solution [Prandtl (1925)]. Table 5.1 presents the dust threshold results over the three test bed configurations at various stability conditions. According to results from the neutral stability settings (bulk $Ri \approx 0$), two general outcomes were: 1) that dust threshold may be achieved at lower wind speeds for rougher surfaces under neutral stability and 2) that dust threshold occurs at a skin friction coefficient of approximately 0.0057.

Including the neutral cases, two stability conditions were simulated for dust threshold over Test Bed 1, five settings for Test Bed 2, while three for Test Bed 3. Particle impaction measurements indicated that dust threshold over Test Bed 1, $z_o = 0.015\ mm$, and Test Bed 2, $z_o = 0.09\ mm$, was achieved at lower wind speeds for increased surface instability. However, over Test Bed 3, $z_o = 0.018\ mm$, dust threshold under unstable conditions was reached at wind speeds higher than that at neutral stability.

Due to the application of heated steel nuts as roughness elements, such an opposite threshold trend over Test Bed 3 may have been caused by some type of cohesive interaction with the steel nuts, initially delaying the movement of dust. Such a cohesive force from the steel nuts may have been enhancement of electrostatic attraction due to surface heating.

Table 5.1: Overall dust threshold results from the experimental conditions simulated at MARSWIT.

Test Surface Designation	Surface Description	Roughness Height (mm)	Mean Surface Temperature (°C)	Bulk Richardson Number	Threshold Freestream Speed (m/s)	Threshold Friction Speed (m/s)	Threshold Skin Friction Coefficient
Test Bed 1	Rippled 32-grit sandpaper	0.15	20.30	≈ 0	30.38	1.63	0.0057
			117.56	-0.0137	7.91		0.0846
Test Bed 2	Smooth 32-grit sandpaper	0.09	20.05	≈ 0	30.27	1.61	0.0057
			76.92	-0.0009	24.76		0.0085
			125.35	-0.0019	21.69		0.0111
			150.27	-0.0025	20.44		0.0125
			174.97	-0.0034	19.86		0.0132
Test Bed 3	Smooth 32-grit sandpaper w/ steel nuts	0.18	20.67	≈ 0	15.13	0.77	0.0051
			83.54	-0.0012	20.93		0.0027
			200.96	-0.0024	24.10		0.0020

Although dust entrainment under unstable conditions over Test Bed 3 was achieved at higher friction speeds than that at neutral conditions, photos of the test surface after the threshold test did visually indicate that dust flux from the surface was greater as the boundary layer instability is increased. Upon initial movement of loose particles due to increased vertical turbulence, the underlying layers of dust were presumably emitted from the surface by secondary entrainment mechanisms. Such suspension methods could include particle impaction or even localized vortical motions initiated by convection and enhanced by roughness elements. Thus, implying that over rough-dry terrains such as that on Mars, buoyancy can play a large part in the suspension of dust in that it enhances vertical turbulence at the lowest wind speeds and that it is a major mechanism in developing particle-entraining vortical motions [Metzger *et al*. (1999), Metzger *et al*. (2000), Edgett and Malin (2000)].

References

Arvidson, R.E. (1972) Aeolian processes on Mars: erosive velocities, settling velocities, and yellow clouds. *Geol. Soc. of America Bul.*, *83*, 1503-1508.

Arvidson, R.E. (1973) Aeolian processes on Mars: erosive velocities, settling velocities, and yellow clouds: reply. *Geol. Soc. of America Bul.*, *84*, 349-350.

Arvidson, R.E. E.A. Guinness, H.J. Moore, J. Tillman, and S.D. Wall (1983) Three Mars years: Viking Lander 1 imaging observations. *Science*, *22*, 463-468.

Bagnold, R.A. (1941) *The Physics of Blown Sand and Desert Dunes*. Chapman and Hall, London, 265 pp.

Bagnold, R.A. (1954) Experiments on a gravity-free dispersion of large solid spheres in a Newtonian fluid under shear.

Bird, R.B., W.E. Stewart, and E.N. Lightfoot (1966) *Transport Phenomena*. John Wiley & Sons, New York, 780 pp.

Clauser, F.H. (1954) Turbulent boundary layers in adverse pressure gradients. *J. Atmos. Sci.*, *21*, 91-108.

Coleman, H.W. and W.G. Steele, Jr. (1989) *Experimentation and Uncertainty Analysis For Engineers*. John Wiley & Sons, New York, 205 pp.

Coquilla, R.V. and B.R. White (1999) Mars Aeolian dust threshold: a wind tunnel study for unstable atmospheric conditions. AGU 1999 Fall Meeting Poster, P31A-11.

DeGarmo, E.P., J.T. Temple, and R.A. Kohser (1988) *Materials and Processes in Manufacturing, 7th ed*. MacMillan Publishing Company, New York, 1172 pp.

Delory, G.T., W.M. Farrell, and M.D. Desch (2001) A global electric circuit on Mars. 32nd LPSC, No. 2150.

Desch, S.J. and G.R. Wilson (1997) Electrostatic charging of saltating particles. 28th LPSC, No. 1173.

Fuchs, N.A. (1964) *The Mechanics of Aerosols*. Pergamon Press, New York, 408 pp.

Golder, D. (1972) Relations among stability parameters in the surface layer. *Boundary-Layer Meteor.*, *3*, 47-58.

Golombek, M.P. (1998) The Mars Pathfinder mission and science results. 29th LPSC, No. 1186.

Golombek, M.P., R.C. Anderson, J.R. Barnes, J.F. Bell III, N.T. Bridges, D.T. Britt, J. Brückner, R.A. Cook, D. Crisp, J.A. Crisp, T. Economou, W.M. Folkner, R. Greeley, R.M. Haberle, R.B. Hargraves, J.A. Harris, A.F.C. Haldermann, K.E. Herkenhoff, S.F. Hviid, R. Jaumann, J.R. Johnson, P.H. Kallemeyn, H.U. Keller, R.L. Kirk, J.M. Knudsen, S. Larsen, M.T. Lemmon, M.B. Madsen, J.A. Magalhães, J.N. Maki, M.C. Malin, R.M. Manning, J. Matijevic, H.Y. McSween, Jr., H.J. Moore, S.L. Murchie, J.R. Murphy, T.J. Parker, R. Reider, T.P. Rivellini, J.T. Schofield, A. Seiff, R.B. Singer, P.H. Smith, L.A. Soderblom, D.A. Spencer, C.R. Stoker, R. Sullivan, N. Thomas, S.W. Thurman, M.G. Tomasko, R.M. Vaughan, H. Wänke, A.W.Ward, and G.R. Wilson (1999a) Overview of the Mars Pathfinder Mission: Launch through landing, surface operations, data sets, and science results. *J. Geophys. Res.*, *104*, 8585-8594.

Greeley, R., J.D. Iversen, J.B. Pollack, N. Udovich, and B.R. White (1974) Wind tunnel studies of Martian aeolian processes. *Proc. R. Soc. Lond. A.*, *341*, 331-360.

Greeley, R., R.N. Leach, B.R. White, J.D. Iversen, and J.B. Pollack (1980) Threshold wind speeds for sand on Mars: wind tunnel simulations. *Geophys. Res. Lett.*, *7*, 2: 121-124.

Greeley, R. and J.D. Iversen (1985) *Wind as a Geological Process on Earth, Mars, Venus and Titan*. Cambridge University Press, Cambridge, 333 pp.

Greeley, R., A. Dobrovolskis, L.R. Gaddis, J.D. Iversen, N. Lancaster, R.N. Leach, K.R. Rasmussen, R.S. Saunders, J.J. van Zyl, S. Wall, B.R. White, and H.A. Zebker (1991) Radar-aeolian roughness project. *NASA CR-4378*, 124 pp.

Greeley, R., N. Lancaster, S. Lee, and P. Thomas (1992) Martian aeolian processes, sediments, and features. In H.H. Kieffer, B.M. Jakosky, C.W. Snyder, and M.S. Matthews (eds.), *Mars*, University of Arizona Press, Tucson, pp. 730-766.

Greeley, R., M. Kraft, R. Sullivan, G. Wilson, N. Bridges, K. Herkenhoff, R.O. Kuzmin, M. Malin, and W. Ward (1999) Aeolian features and processes at the Mars Pathfinder landing sites. *J. Geophys. Res.*, *104*, 8573-8584.

Greeley, R., R. Coquilla, G. Wilson, B. White, R. Haberle, J.F. Soriano, and C. Bratton (1999) Mars dust: laboratory experiments of flux as a function og surface roughness. 30th LPSC, No. 1189.

Hess, S.L., R.M. Henry, C.B. Leovy, J.A. Ryan, and J.E. Tillman (1977) Meteorological results from the surface of Mars: Viking 1 and 2, *J. Geophys. Res.*, *82*, 4559-4574.

Iversen, J.D. and B.R. White (1982) Saltation threshold on Earth, Mars, and Venus. *Sedimentology*, *29*, 111-119.

Lacchia, B.M. (1994) The behavior of dust in a simulated Martian environment. M.S. dissertation. University of California, Davis, 134 pp.

Lancaster, N. and W.G. Nickling (1994) Aeolian sediment transport. In A.D. Abrahams and A.J. Parsons (eds.), *Geomorphology of Desert Environments*, Chapman and Hall, London, 447-473.

MacMillan, F.A. (1954) Viscous effects on flattened Pitot tubes at low speeds. *Journal of the Royal Aeronautical Society*, *58*.

MacMillan, F.A. (1956) Experiments on Pitot tubes in shear flow. *R & M*, *3028*.

Middleton, N. (1997) Desert dust. in D.S.G. Thomas (ed.), *Arid Zone Geomorphology: Process, Form, and Change in Drylands, 2nd ed*., John Wiley & Sons, Chichester, 413-436.

Murphy, J.R., G.W. Wilson, A. Seiff, J.T. Schofield, J. Magalhaes, S. Larsen, R.M. Haberle, D. Crisp, and J. Barnes (1998) Meteorological results from the Mars Pathfinder lander: An overview. 29th LPSC, No. 1824.

Ohanian, H.C. (1989) *Physics, 2nd ed., expanded*. W.W. Norton & Company, New York.

Owen, E. and R.C. Pankhurst (1977) *Measurement of Airflow*.

Prandtl, L. (1925) Uber die ausgebildete Turbulenz, *ZAMM*, *5*, 136-139; cited in Schlichting, H., *Boundary Layer Theory, 7th ed*., pp. 578-595, McGraw-Hill, New York, 1979.

Priestly, C.H.B. (1959) *Turbulent Transfer in the Lower Atmosphere*. University of Chicago Press.

Pye, K. (1987) *Aeolian Dust and Dust Deposits*. Academic Press, London, 334 pp.

Reible, D.D. (1999) *Fundamentals of Environmental Engineering*. Lewis Publishers, Boca Raton, Florida, 526 pp.

Ryan, J.A., R.M. Henry, S.L. Hess, C.B. Leovy, J.E. Tillman, and C. Walcek (1978) Mars meteorology: Three seasons at the surface. *Geophys. Res. Lett.*, *5*, 715-718.

Saffman, P.G. (1965) The lift on a small sphere in a slow shear flow. *Journal of Fluid Mechanics*, *22*, part 2, 385-400.

Sagan, C. and J.B. Pollack (1969) Windblown dust on Mars. *Nature*, *223*, 791-794.

Sagan, C. (1973) Sandstorms and eolian erosion on Mars. Journal of Geophysical Research, 78, 20: 4155-4161.

Sagan, C., D. Pieri, P. Fox, R. Arvidson, and E. Guinness (1977) Particle motion on Mars inferred from the Viking lander cameras. *J. Geophys. Res.*, *82*, 4430-4438.

Schilchting, H. (1979) *Boundary-Layer Theory, 7th ed.* McGraw-Hill, New York, 744 pp.

Schofield, J.T., J.R. Barnes, D. Crisp, R.M. Haberle, S. Larsen, J.A. Magalhães, J.R. Murphy, A. Seiff, and G. Wilson (1997) The Mars Pathfinder Atmospheric Structure Investigation/Meteorology (ASI/MET) Experiment. *Science*, *278*, 1752-1758.

Seinfeld, J.H. and S.N. Pandis (1998) *Atmospheric Chemistry and Physics: From Air Pollution to Climate Change*. John Wiley & Sons, New York, 1326 pp.

Shames, I.H. (1982) *Mechanics of Fluids, 2nd ed*. McGraw-Hill, New York, 558 pp.

Stull, R.B. (1988) *An Introduction to Boundary Layer Meteorology*. Kluwer Academic Publishers, Boston, 670 pp.

Sullivan, R., M. Golombek, R. Greeley, K. Herkenhoff, M. Kraft, J. Murphy, P. Smith, and G. Wilson (2000) Results of the imager for Mars Pathfinder windsock experiment. 31st LPSC, No. 1853.

Sullivan, R., R. Greeley, M. Kraft, M. Golombek, K. Herkenoff, J. Murphy, G. Wilson, and P. Smith (2000) Results of the imager for Mars Pathfinder windsock experiment. *J. Geophys. Res.*, *105*, E10: 24,547-24,562.

Sutton, J.L., C.B. Leovy, and J.E. Tillman (1978) Diurnal variations of the Martian surface layer meteorological parameters during the first 45 sols at two Viking Lander sites. *J. Atmos. Sci.*, *35*, 2346-2355.

Wang, I.T. (1981) The determination of surface-layer stability and eddy fluxes using wind speed and vertical temperature gradient measurements. *J. Applied Meteorology*, *20*, 10: 1241-1248.

White, B.R. (1979) Soil transport by winds on Mars. *J. Geophys. Res.*, *84*, 4643-4651.

White, B.R. (1981) Low-Reynolds-number turbulent boundary layers. *J. Fluid Mech.*, *103*, 624-630.

White, B.R. (1986) Particle dynamics in two-phase flows. *Encyclopedia of Fluid Mechanics*, 4, Chapter 8, Gulf Publishing Co., Houston, p.239-283.

White, B.R. (1987) A low-density boundary-layer wind tunnel facility. AIAA 25th Aerospace Sciences Meeting, *AIAA-87-2091*, 13 pp.

White, B.R., B.M. Lacchia, R. Greeley, and R.N. Leach (1997) Aeolian behavior of dust in a simulated Martian environment. *J. Geophys. Res.*, *102*, E11: 25,629-25,640.

White, B.R. A method to determine surface roughness, z_o, and friction velocity, u*, for stable and unstable field data. *Class notes.*

White, F.M. (1991) *Viscous Fluid Flow, 2nd ed*. McGraw-Hill, New York, 614 pp.

Wiggs, G.F.S. (1997) Sediment mobilization by the wind. In D.S.G. Thomas (ed.), *Arid Zone Geomorphology: Process, Form, and Change in Drylands, 2nd ed*., John Wiley & Sons, Chichester, 351-372.

Wilson, G.R., R. Greeley, and B.R. White (1997) Experiments of dust threshold and flux under Martian conditions. 28th LPSC, No. 1171.

Wilson, G.R., R. Greeley, and B.R. White (1997) Experiments of dust threshold and flux under Martian conditions. 28th LPSC, 1563-1564.

Wilson, G.R. and M Joshi (2000) The Martian surface boundary layer. 31st LPSC, No. 1678.

Young, A.D. and J.N. Maas (1936) The behavior of a Pitot tube in a transverse total-pressure gradient. *R & M*, *1770*.

Zimon, A.D. (1969) Adhesion of Dust and Powder. Plenum Press, New York, 424 pp.

Zoumakis, N.M. and A.G. Kelessis (1991) The dependence of the bulk Richardson number on stability in the surface layer. *Boundary-Layer Meteorology*, *57*, 407-414.

Appendix A: Instrument Calibration Conversions for Data Reduction

Instrument Calibration Conversions for Data Reduction

Type T Thermocouples **Calibration Date: 2/1/99**

Polynomial conversion equation from thermocouple reading [μV] to temperature [deg C]

Polynomial Order	Polynomial Coefficient	For TC voltage readings >= 0	For TC voltage readings < 0
7	a	0.00000000E+00	2.59491920E-02
6	b	2.59280000E-02	-2.13169670E-07
5	c	-7.60296100E-07	7.90186920E-10
4	d	4.63779100E-11	4.25277777E-13
3	e	-2.16539400E-15	1.33044730E-16
2	f	6.04814400E-20	2.02414460E-20
1	g	-7.29342200E-25	1.26681710E-24
	Range:	0 to 400 deg C	-200 to 0 deg C
	Error:	0.03 to -0.03 deg C	0.04 to -0.02 deg C

Figure A. 1: Calibration equation and performance characteristics for Type T thermocouples.

Traverse Height Mechanism **Calibration Date: 11/6/96**

Linear conversion equation from variable resistor reading [V] to height [mm]

Linear slope:	200.65	mm/V
Linear offset:	0.331982	V
Error:	+/- 0.5	mm
Length from Pitot tube center to outer wall:	0.45	mm

Figure A. 2: Calibration equation and performance characteristics for traverse height measurement.

Tavis Pressure Transducer **Calibration Date: 6/15/00**

Linear conversion equation from Tavis pressure transducer reading [V] to ambient pressure [mb]

Transducer Information

Manufacturer: Tavis Corp
Model Number: P-4AS
Serial Number: 1269
ECN: M112233

Range and Accuracy

Pressure Range: 0 to 0.36 psia
Voltage Range: 0 to 5 V
Static Error (% FS): 0.5
Thermal Effects (% FS): 2.0
Output Noise (% FS): 2.0
Overall Error (% FS): 2.87

Calibration Conditions

Temperature: 20 deg C
Humidity: 48%
Standard Model: WS 112

Calibration Coefficients

Slope [mb/V] = 5.0372
Offset [mb] = 0

Calibration Error

SEE (mb) = 0.893
Range (mb) = 24.822
Bias (% FS) = 7.20%

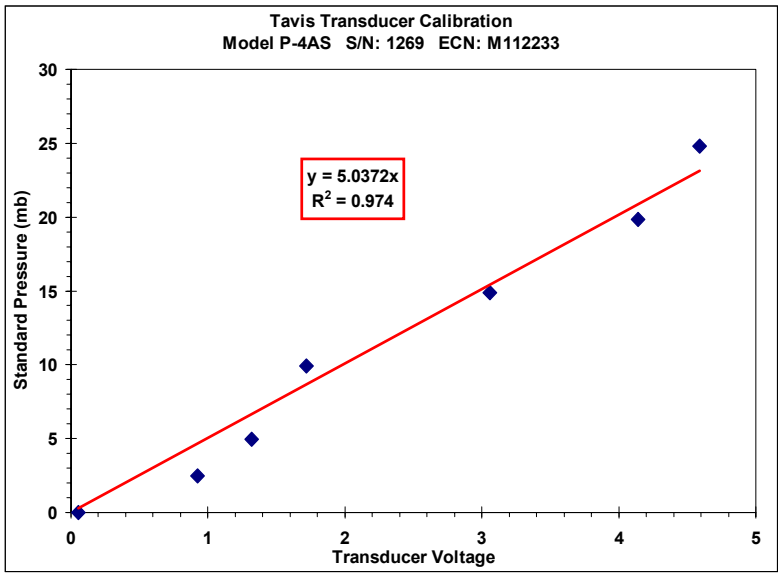

Standard Pressure (psi)	Standard Pressure (mb)	Standard Reference Voltage	Measured Transducer Voltage Output	Error in Measured Transducer Voltage	% Error in Measured Transducer Voltage	Calculated Transducer Pressure (mb)	Error in Calculated Transducer Press (mb)	% FS Error in Calculated Transducer Pressure	Standard Error Estimate SEE (mb)
0.000	0.000	0.400	0.053	-0.347	86.75%	0.267	0.267	#DIV/0!	3.06E+00
0.036	2.482	0.900	0.923	0.023	2.56%	4.649	2.167	87.31%	1.34E-02
0.072	4.964	1.300	1.321	0.021	1.62%	6.654	1.690	34.04%	1.12E-02
0.144	9.929	1.700	1.717	0.017	1.00%	8.649	-1.280	12.89%	7.33E-03
0.216	14.893	2.900	3.060	0.160	5.52%	15.414	0.521	3.50%	6.50E-01
0.288	19.858	4.100	4.141	0.041	1.00%	20.859	1.001	5.04%	4.27E-02
0.360	24.822	4.500	4.591	0.091	2.02%	23.126	-1.696	6.83%	2.10E-01

Figure A. 3: Calibration equation and performance characteristics for Tavis Model P-4AS absolute pressure transducer.

Setra 239 Pressure Transducer **Calibration Date: 6/7/00**

Linear conversion equation from Setra 239 transducer reading [V] to differential pressure [Pa]

Transducer Information

Manufacturer: Setra Systems
Model Number: 239
Serial Number: 42893
ECN: M110860

Range

Pressure Range: 0 to 0.02 psid
Voltage Range: 0 to 5 V

Accuracy

Repeatability (% FS): 0.02
Hysteresis (% FS): 0.01
Non-linearity (% FS): 0.10
Output Noise (% FS): 0.02
Thermal Effects (% FS): 0.01
Overall Error (% FS): 0.105

Calibration Conditions

Temperature: 23 deg C
Humidity: 48%
Calib Standard: M051921

Standard Pressure psid	Standard Pressure Pa	Measured Transducer Voltage Output	Calculated Transducer Pressure (mb)	Error in Calculated Transducer Press (mb)	% Error in Calculated Transducer Pressure	Local Standard Error (Local SEE)
0.0000	0.00	-0.030224	-0.83	-0.83	N/A	0.6859
0.0048	33.10	1.171430	32.10	-1.00	3.01%	0.9930
0.0084	57.92	2.087025	57.19	-0.73	1.26%	0.5319
0.0121	83.43	3.034500	83.15	-0.28	0.33%	0.0774
0.0160	110.32	4.011070	109.91	-0.41	0.37%	0.1670
0.0202	139.28	5.058000	138.60	-0.68	0.49%	0.4620
0.0163	112.39	4.075920	111.69	-0.70	0.62%	0.4902
0.0121	83.43	3.040940	83.33	-0.10	0.12%	0.0103
0.0086	59.30	2.151860	58.97	-0.33	0.56%	0.1100
0.0040	27.58	0.992376	27.19	-0.39	1.40%	0.1497
0.0000	0.00	-0.027851	-0.76	-0.76	N/A	0.5824
-0.0041	-28.27	-1.069245	-29.30	-1.03	3.64%	1.0608
-0.0079	-54.47	-2.016457	-55.25	-0.78	1.44%	0.6154
-0.0126	-86.88	-3.187970	-87.36	-0.48	0.55%	0.2302
-0.0161	-111.01	-4.074200	-111.64	-0.63	0.57%	0.3991
-0.0171	-117.90	-4.312600	-118.17	-0.27	0.23%	0.0726
-0.0163	-112.39	-4.107100	-112.54	-0.15	0.14%	0.0238
-0.0123	-84.81	-3.135120	-85.91	-1.10	1.30%	1.2101
-0.0081	-55.85	-2.046300	-56.07	-0.22	0.40%	0.0498
-0.0043	-29.65	-1.095247	-30.01	-0.36	1.23%	0.1321
0.0000	0.00	-0.024183	-0.66	-0.66	N/A	0.4391

Calibration Coefficients

Slope [Pa/V] = 27.402
Offset [Pa] = 0

Calibration Error

Standard Error of Estimate, SEE (Pa) = 0.6686
SEE Range (Pa) = 257.18
Bias (% FS) = 0.52%

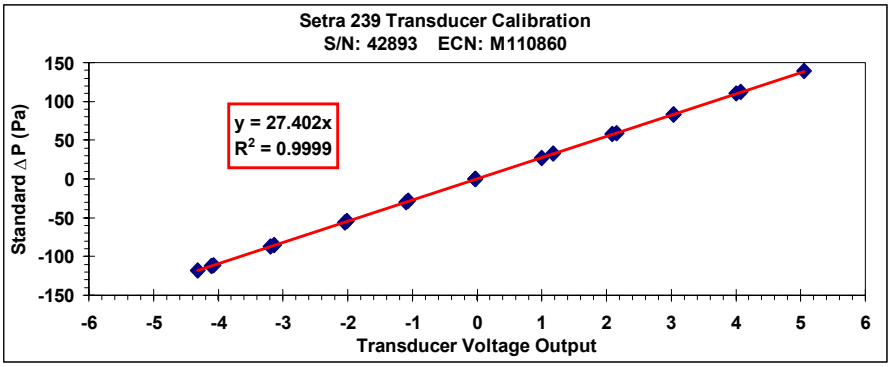

Figure A. 4: Calibration equation and performance characteristics for freestream Pitot-static tube Setra Model 239 differential pressure transducer.

Setra 239 Pressure Transducer **Calibration Date: 6/7/00**

Linear conversion equation from Setra 239 transducer reading [V] to differential pressure [Pa]

Transducer Information

Manufacturer: Setra Systems
Model Number: 239
Serial Number: 649464
ECN: M110861

Range

Pressure Range: 0 to 0.02 psid
Voltage Range: 0 to 5 V

Accuracy

Repeatability (% FS): 0.02
Hysteresis (% FS): 0.01
Non-linearity (% FS): 0.10
Output Noise (% FS): 0.02
Thermal Effects (% FS): 0.01
Overall Error (% FS): 0.105

Calibration Conditions

Temperature: 23 deg C
Humidity: 48%
Calib Standard: M051921

Standard Pressure psid	Standard Pressure Pa	Measured Transducer Voltage Output	Calculated Transducer Pressure (mb)	Error in Calculated Transducer Press (mb)	% Error in Calculated Transducer Pressure	Local Standard Error (Local SEE)
0.0000	0.00	0.026399	0.73	0.73	N/A	0.5258
0.0048	33.10	1.224905	33.65	0.55	1.66%	0.3035
0.0084	57.92	2.137089	58.70	0.79	1.36%	0.6173
0.0121	83.43	3.084060	84.72	1.29	1.54%	1.6552
0.0160	110.32	4.059680	111.52	1.20	1.08%	1.4289
0.0202	139.28	5.105480	140.24	0.96	0.69%	0.9282
0.0163	112.39	4.124050	113.28	0.90	0.80%	0.8011
0.0121	83.43	3.090130	84.88	1.45	1.74%	2.1120
0.0086	59.30	2.201898	60.48	1.19	2.00%	1.4088
0.0040	27.58	1.045124	28.71	1.13	4.09%	1.2735
0.0000	0.00	0.028170	0.77	0.77	N/A	0.5988
-0.0041	-28.27	-1.011978	-27.80	0.47	1.67%	0.2223
-0.0079	-54.47	-1.954545	-53.69	0.78	1.43%	0.6101
-0.0126	-86.88	-3.120310	-85.71	1.17	1.34%	1.3577
-0.0161	-111.01	-4.001250	-109.91	1.10	0.99%	1.2082
-0.0171	-117.90	-4.238900	-116.44	1.47	1.24%	2.1496
-0.0163	-112.39	-4.035170	-110.84	1.55	1.38%	2.3914
-0.0123	-84.81	-3.068340	-84.28	0.52	0.62%	0.2749
-0.0081	-55.85	-1.982642	-54.46	1.39	2.49%	1.9274
-0.0043	-29.65	-1.035677	-28.45	1.20	4.05%	1.4388
0.0000	0.00	0.033711	0.93	0.93	N/A	0.8575

Calibration Coefficients

Slope (Pa/V) = 27.469
Offset (Pa) = 0

Calibration Error

Standard Error of Estimate, SEE (Pa) = 1.1260
SEE Range (Pa) = 257.18
Bias (% FS) = 0.88%

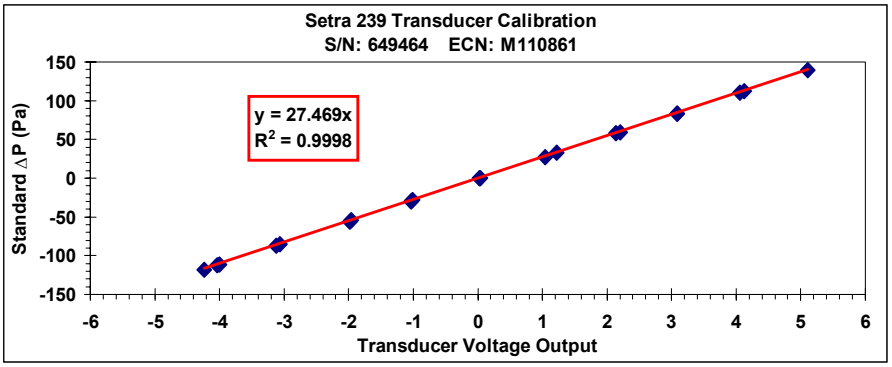

Figure A. 5: Calibration equation and performance characteristics for traversing flattened Pitot tube Setra Model 239 differential pressure transducer.

Appendix B: Procedures for Calculating Dynamic and Kinematic Viscosities

Procedures for Calculating Dynamic and Kinematic Viscosities

Procedures for the calculation of dynamic and kinematic viscosities were obtained from Bird, *et al* (1960). Accordingly, the method begins by determining the dynamic viscosity, which is defined as:

$$\mu = 2.6693 \times 10^{-5} \frac{\sqrt{M_{air} T_a}}{\sigma_{air}^2 \Omega_\mu} \text{ in units of } g/cm\ s \qquad \text{(B-1)}$$

Here, M_{air} is the molecular weight of dry air equal to *28.97 g/mol* (see Figure B. 1), and T_a is the ambient temperature in units of °*K* measured in the wind tunnel test section freestream flow. The variable σ_{air} is the characteristic diameter of an air particle equal to *3.617 Angstroms* (see Figure B. 1), and Ω_μ is the function of non-dimensional temperature, which varies with temperature. Thus, the dynamic and kinematic viscosities are calculated according to the following steps:

Step 1: Solve for the dynamic viscosity using Equation B-1 by first calculating the non-dimensional temperature defined as follows.

$$\frac{\kappa T_a}{\varepsilon_{air}} \qquad \text{(B-2)}$$

Here, $\frac{\varepsilon_{air}}{\kappa}$ is the energy parameter for air, which is equal to *97 °K* (see Figure B. 1). Thus, given the ambient temperature, T_a, the non-dimensional temperature can be calculated using the following substitution in Equation B-2.

$$\frac{\kappa T_a}{\varepsilon_{air}} = \frac{T_a}{97} \qquad \text{(B-3)}$$

Step 2: Use the calculated value for the non-dimensional temperature, $\frac{\kappa T_a}{\varepsilon_{air}}$, from Step 1 to interpolate for the function of non-dimensional temperature, Ω_μ, in Figure B. 2.

Step 3: With all variables given or defined, solve for the dynamic viscosity, μ, in *g/cm s* using Equation B-1.

Step 4: Finally, solve for the kinematic viscosity, ν, using the following equation.

$$\nu = \frac{\mu}{\rho_a} \tag{B-4}$$

Here, ρ_a is the ambient density defined as, $\frac{P_a}{R_{air} T_a}$, where P_a is ambient pressure measured from a static pressure port just outside of the wind tunnel inlet, T_a is ambient temperature measured by a wind tunnel freestream thermocouple, and R_{air} is the gas constant for air. The air gas constant is defined as $\frac{R}{M_{air}}$, where R is the universal gas constant equal to *8,314.472 kJ/kmol K* according to NIST (2001) and M_{air} is the molecular weight for dry air equal to *28.97 kg/kmol* (see Figure B. 1).

TABLE B–I

INTERMOLECULAR FORCE PARAMETERS AND CRITICAL PROPERTIES

Substance	Molecular Weight M	Lennard-Jones Parameters[a]		Critical Constants[b,c,d]				
		σ (Å)	ϵ/κ (° K)	T_c (° K)	p_c (atm)	$\bar{V}_c$ (cm³ g-mole⁻¹)	μ_c (g cm⁻¹ sec⁻¹) × 10⁶	k_c (cal sec⁻¹ cm⁻¹ ° K⁻¹) × 10⁶
Light elements:								
H_2	2.016	2.915	38.0	33.3	12.80	65.0	34.7	—
He	4.003	2.576	10.2	5.26	2.26	57.8	25.4	—
Noble gases:								
Ne	20.183	2.789	35.7	44.5	26.9	41.7	156.	79.2
Ar	39.944	3.418	124.	151.	48.0	75.2	264.	71.0
Kr	83.80	3.498	225.	209.4	54.3	92.2	396.	49.4
Xe	131.3	4.055	229.	289.8	58.0	118.8	490.	40.2
Simple polyatomic substances:								
Air	28.97[e]	3.617	97.0	132.[e]	36.4[e]	86.6[e]	193.	90.8
N_2	28.02	3.681	91.5	126.2	33.5	90.1	180.	86.8
O_2	32.00	3.433	113.	154.4	49.7	74.4	250.	105.3
O_3	48.00	—	—	268.	67.	89.4	—	—
CO	28.01	3.590	110.	133.	34.5	93.1	190.	86.5
CO_2	44.01	3.996	190.	304.2	72.9	94.0	343.	122.
NO	30.01	3.470	119.	180.	64.	57.	258.	118.2
N_2O	44.02	3.879	220.	309.7	71.7	96.3	332.	131.
SO_2	64.07	4.290	252.	430.7	77.8	122.	411.	98.6
F_2	38.00	3.653	112.	—	—	—	—	—
Cl_2	70.91	4.115	357.	417.	76.1	124.	420.	97.0
Br_2	159.83	4.268	520.	584.	102.	144.	—	—
I_2	253.82	4.982	550.	800.	—	—	—	—

Figure B. 1: Table of Lennard-Jones Parameters Scanned from Table B-1 of Bird, et al (1960).

TABLE B–2

FUNCTIONS FOR PREDICTION OF TRANSPORT PROPERTIES OF GASES AT LOW DENSITIES[a]

$\kappa T/\epsilon$ or $\kappa T/\epsilon_{AB}$	$\Omega_\mu = \Omega_k$ (For viscosity and thermal conductivity)	$\Omega_{\mathcal{D},AB}$ (For mass diffusivity)	$\kappa T/\epsilon$ or $\kappa T/\epsilon_{AB}$	$\Omega_\mu = \Omega_k$ (For viscosity and thermal conductivity)	$\Omega_{\mathcal{D},AB}$ (For mass diffusivity)
			2.50	1.093	0.9996
0.30	2.785	2.662	2.60	1.081	0.9878
0.35	2.628	2.476	2.70	1.069	0.9770
0.40	2.492	2.318	2.80	1.058	0.9672
0.45	2.368	2.184	2.90	1.048	0.9576
0.50	2.257	2.066	3.00	1.039	0.9490
0.55	2.156	1.966	3.10	1.030	0.9406
0.60	2.065	1.877	3.20	1.022	0.9328
0.65	1.982	1.798	3.30	1.014	0.9256
0.70	1.908	1.729	3.40	1.007	0.9186
0.75	1.841	1.667	3.50	0.9999	0.9120
0.80	1.780	1.612	3.60	0.9932	0.9058
0.85	1.725	1.562	3.70	0.9870	0.8998
0.90	1.675	1.517	3.80	0.9811	0.8942
0.95	1.629	1.476	3.90	0.9755	0.8888
1.00	1.587	1.439	4.00	0.9700	0.8836
1.05	1.549	1.406	4.10	0.9649	0.8788
1.10	1.514	1.375	4.20	0.9600	0.8740
1.15	1.482	1.346	4.30	0.9553	0.8694
1.20	1.452	1.320	4.40	0.9507	0.8652
1.25	1.424	1.296	4.50	0.9464	0.8610
1.30	1.399	1.273	4.60	0.9422	0.8568
1.35	1.375	1.253	4.70	0.9382	0.8530
1.40	1.353	1.233	4.80	0.9343	0.8492
1.45	1.333	1.215	4.90	0.9305	0.8456
1.50	1.314	1.198	5.0	0.9269	0.8422
1.55	1.296	1.182	6.0	0.8963	0.8124
1.60	1.279	1.167	7.0	0.8727	0.7896
1.65	1.264	1.153	8.0	0.8538	0.7712
1.70	1.248	1.140	9.0	0.8379	0.7556
1.75	1.234	1.128	10.0	0.8242	0.7424
1.80	1.221	1.116	20.0	0.7432	0.6640
1.85	1.209	1.105	30.0	0.7005	0.6232
1.90	1.197	1.094	40.0	0.6718	0.5960
1.95	1.186	1.084	50.0	0.6504	0.5756
2.00	1.175	1.075	60.0	0.6335	0.5596
2.10	1.156	1.057	70.0	0.6194	0.5464
2.20	1.138	1.041	80.0	0.6076	0.5352
2.30	1.122	1.026	90.0	0.5973	0.5256
2.40	1.107	1.012	100.0	0.5882	0.5170

[a] Taken from J. O. Hirschfelder, R. B. Bird, and E. L. Spotz, *Chem. Revs.*, 44,

Figure B. 2: Table of Non-Dimensional Temperature Scanned from Table B-2 of Bird, et al (1960).

Appendix C: Procedures for Calculating Mean Free Path

Procedures for Calculating Mean Free Path

Procedures for determining the mean free path were obtained from Bird, *et al* (1960). Accordingly, the definition for the mean free path is given as follows.

$$\lambda_{air} = \frac{3\mu}{\rho_a \bar{u}} \tag{C-1}$$

Here, μ is the dynamic viscosity in *g/cm s* and ρ_a is the ambient density in g/cm^3, both calculated based on the procedures given in Appendix B. The parameter $\bar{u}$ is the mean speed of an air molecule in *cm/s*, which is defined as follows.

$$\bar{u} = \sqrt{\frac{8\kappa T_a}{\pi m_{air}}} \tag{C-2}$$

Here, T_a is the ambient temperature in °*K*, which is measured in the freestream of the wind tunnel test section, and κ is Boltzman's constant, which is equal to $1.3806503 \times 10^{-23} \frac{J}{^\circ K}$ or $1.3806503 \times 10^{-16} \frac{g \cdot cm^2}{s^2 \cdot ^\circ K}$. The parameter m_{air} is the molecular mass of dry air in *grams*, which is also defined as follows.

$$m_{air} = \frac{M_{air}}{N_A} \tag{C-3}$$

where: M_{air} = the molecular weight for dry air = *28.97 g/mol*

N_A = Avogadro's number = $6.02214199 \times 10^{23}\ mol^{-1}$

Appendix D: Procedures for Applying Flattened Pitot Tube Corrections

Procedures for Applying Flattened Pitot Tube Corrections

Corrections to the velocity measurements collected from the boundary-layer traversed flattened Pitot tube were based on effects generated by: 1) a velocity gradient [MacMillan (1956)], 2) wall proximity [MacMillan (1956)], and 3) viscosity [MacMillan (1954)]. Respectively, the three types of corrections were applied to the flattened Pitot tube readings according to the following "step-by-step" procedure:

Step 1: First, subtract zero-wind voltage offset, taken at the experimental low-pressure condition, from the measured voltages from Setra Model 239 differential pressure transducer connected to the traversing flattened Pitot tube. Then, calculate an initial differential pressure, ΔP_i, in *Pascals* according to the Equation D-1 using the calibration conversion coefficients of that particular transducer serial number.

$$\Delta P_i = \begin{pmatrix} Measured \\ Voltage \end{pmatrix} - \begin{pmatrix} Zero-Wind \\ Voltage \end{pmatrix} * \begin{matrix} Conversion \\ Equation\,Slope \end{matrix} \left[\frac{Pa}{V}\right] + \begin{matrix} Conversion \\ Equation\,Offset \end{matrix} [Pa] \qquad \text{(D-1)}$$

Step 2: Calculate an initial velocity, U_i, in *m/s* as defined in Equation D-2 using the initial differential pressure, ΔP_i, calculated in Step 1.

$$U_i = \sqrt{\frac{2\Delta P_i}{\rho_a}} \qquad \text{(D-2)}$$

Here, the ρ_a is the ambient density in kg/m^3 as calculated in Appendix B.

Step 3: Calculate an initial traverse height, z_i, in *mm* from the traverse variable resistor voltage reading using the following calibration conversion equation.

$$z_i = \begin{pmatrix} Measured \\ Voltage \end{pmatrix} - \begin{pmatrix} Offset \\ Voltage \end{pmatrix} * \begin{matrix} Conversion \\ Equation\,Slope \end{matrix} \left[\frac{mm}{V}\right] + \begin{matrix} Pitot\,Tube \\ Outer\,Radius \end{matrix} [mm] \qquad \text{(D-3)}$$

Step 4: Apply the velocity gradient correction defined in Equation D-4 to initial height, z_i, from Step 3 to get final height, z_f, in *mm*.

$$z_f = z_i + 0.15 * \frac{Pitot\,Tube}{Outer\,Height} \tag{D-4}$$

Step 5: Calculate the ratio of the final height, z_f, calculated from Step 4, to the flattened Pitot tube outer height or diameter, D (i.e., z_f/D).

Step 6: Apply the wall proximity correction given in Equation D-5 to the initial differential pressure, ΔP_i, calculated in Step 1 by first using the ratio, z_f/D, calculated in Step 5 to interpolate for the appropriate "*% of* ΔP_i" value from the experimental data given in Figure D. 1 [MacMillan (1956)]. Then, add the "*% of* ΔP_i" value to ΔP_i to get the final differential pressure, ΔP_f, in *Pascals*.

$$\Delta P_f = \Delta P_i + \left(\frac{\%\ of\ \Delta P_i}{100} * \Delta P_i \right) \tag{D-5}$$

Step 7: Calculate the wall-proximity corrected velocity, U_1, using the wall proximity corrected final differential pressure, ΔP_f, from Step 6 in Equation D-10.

$$U_1 = \sqrt{\frac{2\Delta P_f}{\rho_a}} \tag{D-10}$$

Again, ρ_a is the ambient density in kg/m^3 as calculated in Appendix B.

Step 8: Calculate the Reynolds number at the inlet of the pitot tube, Re_d, according to Equation D-11 and using the pitot tube inner height or diameter, d, and the wall proximity corrected velocity, U_1, from Step 7 to initiate viscosity correction.

$$Re_d = \frac{U_1 d}{\nu} \tag{D-11}$$

Here, ν is the kinematic viscosity as calculated in Appendix B.

Step 9: The viscosity correction is essentially based on the drift of the Pitot tube inlet stagnation pressure coefficient from the ideal value of one. In fact, the complete equation for calculating the pitot tube velocity is defined as:

$$U_f = \sqrt{\frac{2\Delta P_f}{C_p \rho_a}} \tag{D-12}$$

Thus, the next step is then to calculate the corresponding coefficient of pressure, C_p, using the appropriate equation according to the following range in Re_d.

For $0 \le Re_d \le 13.6,\ C_p = -0.06795274 \log_e[Re_d] + 1.16136140$. (D-13)

For $13.6 \le Re_d \le 1000,\ C_p = 0.003722934 \log_e[Re_d] + 0.974282884$. (D-14)

For $Re_d > 1000,\ C_p = 1$. (D-15)

Step 10: Lastly, the final traverse pitot tube velocity value, U_f, can now be determined according the following Equation D-16 using the coefficient of pressure, C_p, and the wall proximity corrected velocity, U_1, from Step 7.

$$U_f = \frac{1}{\sqrt{C_p}} U_1 \tag{D-16}$$

Wall Proximity Correction

Reference: MacMillan, F.A., "Experiments on Pitot Tubes in Shear Flow"
Rep.Memor.Aero.Res.Comm.Lond. or R.& M., No.3028,1956.

Z = height of traverse pitot tube from ground
D = outer diameter of pitot tube

Z/D	% of ΔP
0.4	4.5
0.5	3.1
0.55	2.6
0.6	2.17
0.65	1.8
0.7	1.45
0.75	1.17
0.8	0.95
0.85	0.85
0.9	0.75
0.95	0.68
1	0.62
1.05	0.55
1.1	0.5
1.15	0.45
1.2	0.4
1.25	0.37
1.3	0.32
1.4	0.24
1.5	0.17
1.6	0.1
1.7	0.05
1.8	0

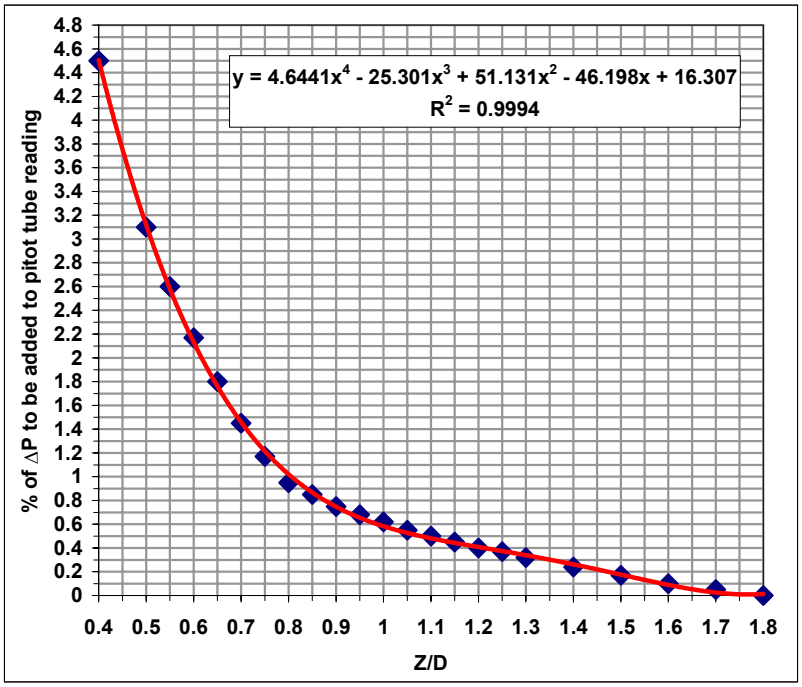

Figure D. 1: Experimental data obtained from MacMillan (1956) for traversing flattened Pitot tube wall-proximity correction.

Appendix E: Procedures for Generating Non-Dimensional Laminar Wind Profile

Procedures for Generating Non-Dimensional Laminar Wind Profile

Generation of the non-dimensional laminar wind profile was based on a presentation of the Blasius' solution for a flat-plate boundary layer in Shames (1982). In summary, the key equations for local velocity, boundary-layer height, and local height are respectively defined as follows:

$$U = U_F G \qquad \text{(E-1)} \qquad \delta = \sqrt{\frac{30\rho x}{U_F}} \qquad \text{(E-2)} \qquad z = \eta\sqrt{\frac{\rho x}{U_F}} \qquad \text{(E-3)}$$

Thus, the dimensionless local velocity is then defined as $\frac{U}{U_F} = G$. (E-4)

The dimensionless local height is then given as:

$$\frac{z}{\delta} = \frac{\eta\sqrt{\rho x/U_F}}{\sqrt{30\rho x/U_F}} \qquad \Rightarrow \qquad \frac{z}{\delta} = \frac{\eta}{\sqrt{30}} \qquad \text{(E-5)}$$

To find the dimensionless values for laminar flow, the values for η and the corresponding value for G was collected from the following Figure E. 1, obtained from Shames (1972).

Grid index	η	f	G	H
1	0	0	0	0
11	0.30	0.014928	0.099513	0.331549
21	0.60	0.059685	0.198788	0.329930
41	1.20	0.237803	0.393651	0.316862
61	1.80	0.529374	0.574950	0.283715
81	2.40	0.922420	0.729741	0.229133
101	3.00	1.397569	0.847381	0.162165
121	3.60	1.931196	0.924986	0.098317
141	4.20	2.500709	0.968592	0.050256
161	4.80	3.088908	0.989203	0.021444
181	5.40	3.685280	0.997334	0.007594
201	6.00	4.284639	1.000000	0.002224

Figure E. 1: Values of η and G for a laminar wind profile scanned from Shames (1972).

Appendix F: Derivation of Equations Used in "Clauser" Smooth-wall Analysis

Derivation of Equations Used in "Clauser" Smooth-wall Analysis

Equations used in the smooth-wall analysis of the boundary-layer profiles [Clauser (1954)] were derived from the dimensionless velocity profile equation for hydraulically smooth-wall flow defined by Schlichting (1979) and in the following equation.

$$\frac{U(z)}{u^*} = \frac{1}{k} ln\left(\frac{u^* z}{\nu}\right) + 5.45 \qquad \text{(F-1)}$$

In general, definitions for the non-dimensional velocity, U/U_F, and the logarithm of local Reynolds number, $log(U_F z/\nu)$, can be derived from Equation F-1. First, convert Equation F-1 into a logarithmic equation by multiplying by *log 2/ln 2*.

$$\left(\frac{log\,2}{ln\,2}\right)\frac{U(z)}{u^*} = \frac{1}{k}\left(\frac{log\,2}{ln\,2}\right) ln\left(\frac{u^* z}{\nu}\right) + \left(\frac{log\,2}{ln\,2}\right) 5.45 \qquad \text{(F-2)}$$

Since, for any variable x, $log(x) = \left(\frac{log\,2}{ln\,2}\right) ln(x)$, Equation F-2 can be redefined as follows:

$$\left(\frac{log\,2}{ln\,2}\right)\frac{U(z)}{u^*} = \frac{1}{k} log\left(\frac{u^* z}{\nu}\right) + \left(\frac{log\,2}{ln\,2}\right) 5.45 \qquad \text{(F-2)}$$

$$\text{Thus, } \frac{U(z)}{u^*} = \frac{1}{k}\left(\frac{ln\,2}{log\,2}\right) log\left(\frac{u^* z}{\nu}\right) + 5.45 \qquad \text{(F-3)}$$

To obtain an equation for the non-dimensional velocity, U/U_F, let $u^* = U_F\sqrt{C_f/2}$. (F-4)

Thus, by substituting the u^* variables in Equation F-3, we get:

$$\frac{U(z)}{U_F\sqrt{C_f/2}} = \frac{1}{k}\left(\frac{ln\,2}{log\,2}\right) log\left(\frac{U_F z\sqrt{C_f/2}}{\nu}\right) + 5.45 \qquad \text{(F-5)}$$

Then, from Equation F-5, we get an equation for the non-dimensional velocity as follows:

$$\frac{U}{U_F} = \sqrt{\frac{C_f}{2}}\left[\frac{1}{k}\left(\frac{ln\,2}{log\,2}\right)log\left(\frac{U_F z}{\nu}\sqrt{\frac{C_f}{2}}\right) + 5.45\right] \tag{F-6}$$

To get the logarithm of local Reynolds number, rearrange Equation F-6 according to the following steps of equations.

$$\frac{U/U_F}{\sqrt{C_f/2}} = \frac{1}{k}\left(\frac{ln\,2}{log\,2}\right)\left[log\left(\frac{U_F z}{\nu}\right) + log\sqrt{\frac{C_f}{2}}\right] + 5.45 \tag{F-7}$$

$$\frac{U/U_F}{\sqrt{C_f/2}} - 5.45 = \frac{1}{k}\left(\frac{ln\,2}{log\,2}\right)\left[log\left(\frac{U_F z}{\nu}\right) + log\sqrt{\frac{C_f}{2}}\right] \tag{F-8}$$

$$k\left(\frac{log\,2}{ln\,2}\right)\left(\frac{U/U_F}{\sqrt{C_f/2}} - 5.45\right) = log\left(\frac{U_F z}{\nu}\right) + log\sqrt{\frac{C_f}{2}} \tag{F-9}$$

Therefore, the definition for the logarithm of local Reynolds number is as follows:

$$log\left(\frac{U_F z}{\nu}\right) = k\left(\frac{log\,2}{ln\,2}\right)\left(\frac{U/U_F}{\sqrt{C_f/2}} - 5.45\right) - log\sqrt{\frac{C_f}{2}} \tag{F-10}$$

To generate the lines of constant C_f, the non-dimensional velocity in Equation F-10 is the resulting value of U/U_F from Equation F-6.

Appendix G: Uncertainty Analysis

Uncertainty Analysis

Uncertainty for any parameter in this study was determined according to the following equation for uncertainty for *95%* confidence [Coleman and Steele (1989)].

$$Unc = \sqrt{X^2 + (tY)^2} \tag{G-1}$$

Here, X is defined as the propagation of bias limits, Y is the propagation of precision limits, and t is precision limit factor, which is a function of the number of samples collected to calculate the specific parameter in mind.

Based on the boundary layer profile experiments, with the scan rate set to *150 Hz* and acquiring data for *120* seconds while also calculating averages every *50* samples, the LabVIEW data acquisition system was able to provide a sample size of *18,000* for each measured parameter. Due to the averaging mode, *360* mean measurements were used for data reduction. Based on the dust threshold experiments, data was collected at *100 Hz* for *600* seconds, while block-averaging *50* samples at a time, thus collecting *1200* mean measurements per experimental run. According to these data acquisition settings and the *t*-distribution table given in the appendix section of Coleman and Steele (1989), $t = 1.96$ at *95%* confidence level.

General parameters that were measured in the experiment were temperature, absolute pressure, and differential pressure. These measured values were then used to measure other parameters such as density, velocity, viscosity, and the Richardson number. To illustrate the steps taken in determining the uncertainties in the magnitudes of these experimental parameters, this section of the report will present the uncertainty calculation of the bulk Richardson number. Later in this section, a table of uncertainty

results will be presented for the many parameters presented in the experimental investigation.

Recall from Chapter 4.8, the bulk Richardson number equation used in the experimental calculations was given as follows according to Figure 4.41.

$$B = \frac{g}{\overline{\theta_{v_F}}} \cdot \frac{\left(\overline{\theta_{v_F}} - \overline{\theta_{v_1}}\right) / \left(\delta - z_1\right)}{\overline{U_F}^2} .\delta^2 \tag{G-1}$$

Here, g is Earth's gravitational constant, δ is the boundary-layer height, z_1 is a chosen height above the surface, θ_{v_F} is the temperature at the wind tunnel freestream, θ_{v_1} is the temperature at height z_1, and U_F is the freestream wind speed.

To initiate the uncertainty analysis, the bulk Richardson number equation was rearranged to include the following equation given for the freestream velocity.

$$U_F = \sqrt{\frac{2\overline{\Delta P}}{k\rho_c}} \tag{G-2}$$

In this equation, ΔP is the differential pressure and k is the pitot tube shape parameter. The variable ρ_c is the chamber density and may be further defined as follows.

$$\rho_C = \frac{\overline{P_C}}{R_{air}\overline{\theta_{v_F}}} \tag{G-3}$$

Here, P_c is the chamber pressure and R_{air} is the gas constant for air, which is also defined as follows.

$$R_{air} = \frac{R}{M_{air}} \tag{G-4}$$

where: R = universal gas constant

M_{air} = molecular weight of an air molecule

By substituting Equations G-4, G-3, and G-2 into Equation G-1 successively, the bulk Richardson number equation can be redefined according to the following equation.

$$B = \frac{gk\overline{P_C}M_{air}\overline{\delta}^2}{2\overline{\Delta P}R\overline{\theta_{v_F}}^2} \cdot \frac{(\overline{\theta_{v_F}} - \overline{\theta_{v_1}})}{(\overline{\delta} - z_1)} \tag{G-4}$$

The reason for this change was so that only one governing data reduction equation (DRE) is tackled in finding the bulk Richardson number uncertainty. Note that this form of the bulk Richardson number depicts all of the measured (P_c, ΔP, δ, θ_{v_F} , and θ_{v_1}) and base or set property (g, M_{air}, R, k, and z_1) values for the experiment.

The second step in an uncertainty analysis procedure is to determine which variables have no effect on the calculated value. In most cases, such variables are base property values. In Equation G-4, the only two variables that have no influence in the calculation turned out to be the acceleration of gravity, g, and the molecular mass of air, M_{air}. According to the National Institute for Standards Technology (NIST) website, Earth's gravity is assigned with an exact value of *9.80665 m/s*^{2}, while the molecular weight for air is *28.97 kg/kmol*.

Variables that do take effect into the uncertainty are those that take on elemental biases and particularly precision biases. Precision biases are generally the standard deviations generated from the measured values in the experiment, thus such variables are essential in the uncertainty analysis. Elemental biases are the inherent variability in the particular parameter, which may be due to: 1) a fossilized bias, 2) manufacturer's specification, 3) calibration, and 4) data acquisition. Measured variables may take on one or more of these elemental biases. Thus, the next step in the uncertainty analysis

procedure is to determine the elemental biases associated with the rest of the base and set property variables and the measured parameters.

A property value that may have influence in the bulk Richardson number calculation is the universal gas constant, R. From the NIST website, R was given a value of *8314.472 kJ/kmol °K* with a fossilized bias of *+/- 0.015 kJ/kmol °K*. Another variable property value was k, which describes the shape characteristics of the pitot tube. Originally, the pitot tube was designed with a shape parameter value of one, which corresponds to an ideal design. This pitot tube has remained as a common instrument inside this low-pressure facility, where it is primarily exposed to fine atmospheric dust experiments. Therefore, due to years of experimental usage, a bias of *+/- 3%*, which can possibly be too low, was used for the uncertainty analysis. The last set property values are the boundary layer height, δ, and the height z_1, which corresponds to the lowest thermocouple rake height. Since the rake is essentially set to have stationary thermocouple height positions, z_1 is set to the height of *2 mm*. This height was also measured with a steel precision linear scale having the lowest increment in the millimeter range. Thus, a calibration bias of *+/- 0.5 mm* was intuitively assigned to the value of z_1. The boundary layer height was a measurement taken from the traverse height mechanism, which was also calibrated against the steel linear precision scale. Thus, it was associated with a calibration bias of *+/- 0.5 mm*, and since voltage data from the traverse height mechanism was collected, a data acquisition bias was applied. Although the boundary layer height was a set value, it also varied between experimental runs.

For all measured variables (δ, P_c, ΔP, θ_{v_F}, and θ_{v_1}), a common data acquisition bias was applied. Using a National Instruments Model AT-MIO-16E-1 12-bit A/D board,

an accuracy of +/- *0.5* least significant bits (LSB) is provided. Therefore, the relative accuracy is determined as follows.

$$\frac{LSB}{2^{\#bits}} = \frac{0.5}{2^{12}} = 1.2207\,x\,10^{-4} \quad \Rightarrow \quad 0.0122\%\ of\ full\ scale(FS) \tag{G-5}$$

With the addition of a National Instruments Signal Conditioning Extension for Instrumentation (SCXI) chassis, the accuracy given in Equation G-5 was improved to *0.006% FS*, according to manufacturer's specifications.

Chamber pressure, P_c, was measured using a Tavis Corporation Model P-4AS total pressure transducer. Biases in the measurements of P_c include not only the data acquisition bias previously described but also biases due to manufacturer's specification and calibration. According to manufacturer's specification, the Tavis pressure transducer generates errors from three sources: 1) *0.5% FS* from static errors, 2) *2.0% FS* from temperature effects, and 3) *2.0% FS* from output noise. The static error also includes errors due to non-linearity, hysteresis, resolution, and repeatability. Overall, the manufacturer's specification bias is calculated as follows:

$$b_{ms,P_c} = \sqrt{(0.5)^2 + (2.0)^2 + (2.0)^2} = 2.87\%FS \tag{G-6}$$

From the calibration data reduction equation, a calibration bias of *7.20% FS* was also determined.

Differential pressure, ΔP, which is used to define the freestream speed in the wind tunnel, was measured by a Setra Systems Model 239 low-range differential pressure transducer. Manufacturer's biases include: 1) *0.02% FS* for repeatability, 2) *0.1% FS* for hysteresis, 3) *0.1% FS* for non-linearity, 4) *0.01% FS* for thermal effects, and 5) *0.02% FS* for output noise. Conducting a calculation similar to Equation G-6 gives an overall

manufacturer's bias for the differential pressure as *0.105% FS*. Calibration of the instrument also generated a calibration bias of *0.88% FS* from the data reduction equation.

All temperature data was measured using Omega Type T thermocouples. These thermocouples were essentially calibrated against a high-precision thermistor temperature sensor input included inside the National Instruments SCXI chassis. According to manufacturer's specifications, the thermistor sustains a bias of *+/- 0.1 °C* from *0* to *55 °C*. Thus, the full-scale calibration bias is given as:

$$b_{ms,\theta} = \frac{0.1}{55}(100) = 0.18\%FS \tag{G-7}$$

A calibration curve was also provided by National Instruments through the LabVIEW data acquisition system software. Based on the polynomial data reduction equation, an error range for temperatures from *0* to *400 °C* was given as *+/- 0.03 °C*. Thus, the calibration bias was determined as:

$$b_{cal,\theta} = \frac{0.03}{400}(100) = 0.0075\%FS \tag{G-8}$$

In order to determine the bias and precision limits in the uncertainty, it is necessary to analyze the sensitivity of the variable parameters towards the main calculated value. Thus, the next step in the investigation was to derive the sensitivity coefficients of all the parameters that affect the uncertainty. Taking the partial derivatives of the variables, k, R, P_c, ΔP, θ_{v_F}, θ_{v_1}, δ, and z_1, from the DRE (Equation G-4) gives the following equation set of sensitivity coefficients.

$$\frac{\partial B}{\partial k} = \frac{g\overline{P_C}M_{air}\overline{\delta}^2}{2\overline{\Delta P}R\overline{\theta_{v_F}}^2}\cdot\frac{(\overline{\theta_{v_F}}-\overline{\theta_{v_1}})}{(\overline{\delta}-z_1)} \tag{G-9}$$

$$\frac{\partial B}{\partial R} = \frac{gk\overline{P_C}M_{air}\overline{\delta}^2}{2\overline{\Delta P}R^2\overline{\theta_{v_F}}^2}\cdot\frac{(\overline{\theta_{v_F}}-\overline{\theta_{v_1}})}{(\overline{\delta}-z_1)} \tag{G-10}$$

$$\frac{\partial B}{\partial P_c} = \frac{gkM_{air}\overline{\delta}^2}{2\overline{\Delta P}R\overline{\theta_{v_F}}^2} \cdot \frac{(\overline{\theta_{v_F}} - \overline{\theta_{v_1}})}{(\overline{\delta} - z_1)} \qquad \text{(G-11)}$$

$$\frac{\partial B}{\partial \Delta P} = \frac{gk\overline{P_C}M_{air}\overline{\delta}^2}{2\overline{\Delta P}^2 R\overline{\theta_{v_F}}^2} \cdot \frac{(\overline{\theta_{v_F}} - \overline{\theta_{v_1}})}{(\overline{\delta} - z_1)} \qquad \text{(G-12)}$$

$$\frac{\partial B}{\partial \theta_{v_F}} = -\frac{gk\overline{P_C}M_{air}\overline{\delta}^2}{2\overline{\Delta P}R(\overline{\delta} - z_1)} \cdot \left(\frac{2\overline{\theta_{v_1}} - \overline{\theta_{v_F}}}{\overline{\theta_{v_F}}^3} \right) \qquad \text{(G-13)}$$

$$\frac{\partial B}{\partial \theta_{v_1}} = -\frac{gk\overline{P_C}M_{air}\overline{\delta}^2}{2\overline{\Delta P}R\overline{\theta_{v_F}}^2(\overline{\delta} - z_1)} \qquad \text{(G-14)}$$

$$\frac{\partial B}{\partial \delta} = \frac{gk\overline{P_C}M_{air}(\overline{\theta_{v_F}} - \overline{\theta_{v_1}})}{2\overline{\Delta P}R\overline{\theta_{v_F}}^2} \cdot \frac{\overline{\delta}}{\overline{\delta} - z_1} \cdot \left(2 - \frac{\overline{\delta}}{\overline{\delta} - z_1} \right) \qquad \text{(G-15)}$$

$$\frac{\partial B}{\partial z_1} = \frac{gk\overline{P_C}M_{air}\overline{\delta}^2}{2\overline{\Delta P}R\overline{\theta_{v_F}}^2} \cdot \frac{(\overline{\theta_{v_F}} - \overline{\theta_{v_1}})}{(\overline{\delta} - z_1)^2} \qquad \text{(G-16)}$$

Using the fastest velocity run over Test Bed 1 under unstable conditions as a sample data set, the sensitivity coefficients in Equations G-9 to G-16 can be determined using the following Table G. 1 of base property and mean measured values. Table G. 2 then presents the resulting sensitivity coefficient quantities.

Table G. 1: Base property and mean measured values from the fastest velocity test run over Test Bed 1 under unstable atmospheric conditions.

Parameter	Value	Units
g	9.80665	m/s^2
M_{air}	28.97	$kg/kmol$
R	8314.472	$kJ/kmol\,°K$
k	1	**
z_1	0.002	m
$\overline{\delta}$	0.301	m
$\overline{P_C}$	969.53	Pa
$\overline{\Delta P}$	40.56	Pa
$\overline{\theta_{v_F}}$	287.47	$°K$
$\overline{\theta_{v_1}}$	341.88	$°K$

** dimensionless

Table G. 2: Resulting sensitivity coefficients for uncertainty calculation of the bulk Richardson number.

Sensitivity Coefficient	Value	Units
$\partial B/\partial k$	-8.465 x 10^{-5}	**
$\partial B/\partial R$	-1.018 x 10^{-8}	$[kJ/kmol\ °K]^{-1}$
$\partial B/\partial P_C$	-8.731 x 10^{-8}	$[Pa]^{-1}$
$\partial B/\partial \Delta P$	-2.168 x 10^{-6}	$[Pa]^{-1}$
$\partial B/\partial \theta_{v_F}$	-2.145 x 10^{-6}	$[°K]^{-1}$
$\partial B/\partial \theta_{v_1}$	-1.556 x 10^{-6}	$[°K]^{-1}$
$\partial B/\partial \delta$	-2.793 x 10^{-4}	$[m]^{-1}$
$\partial B/\partial z_1$	-8.465 x 10^{-5}	$[m]^{-1}$

** dimensionless

With the sensitivity coefficients, the precision limit for the bulk Richardson number calculation can be calculated using an equation for the propagation of precision indices (Equation G-17). The precision index for each measured parameter is the standard deviation for a data set.

$$(Y_B)^2 = \left(\frac{\partial B}{\partial P_c} Y_{P_c}\right)^2 + \left(\frac{\partial B}{\partial \Delta P} Y_{\Delta P}\right)^2 + \left(\frac{\partial B}{\partial \theta_{v_F}} Y_{\theta_{v_F}}\right)^2 + \left(\frac{\partial B}{\partial \theta_{v_1}} Y_{\theta_{v_1}}\right)^2 \qquad \text{(G-17)}$$

For a sample calculation, a precision limit for the bulk Richardson number was calculated based on the following table set of calculated precision indices from the data acquired from the fastest velocity experimental run over Test Bed 1 under unstable conditions.

Table G. 3: Precision indices for the data acquired from the fastest velocity test run over Test Bed 1 under unstable atmospheric conditions.

Measured Parameter	Precision Index Value	Units
P_c	0.008	Pa
ΔP	0.514	Pa
θ_{v_F}	0.221	$°K$
θ_{v_1}	1.580	$°K$

Thus, the corresponding precision limit for the bulk Richardson number is $\pm$ *2.741 x* 10^{-6}.

In determining the bias limit for the bulk Richardson number calculation, overall bias limits were first calculated for each variable according to the biases previously described. An overall bias was generally calculated by taking the square root of the sum of the squares of each particular bias from full scale associated with the corresponding variable. Table G. 4 below presents the collection of elemental biases and overall biases associated with each experimental variable. Note that the highest experimental error originates from the measurement of the chamber pressure.

Table G. 4: Overall and elemental biases from experimental instrumentation and setup.

Variable	Value	Fossilized Bias	Manufacturer's Bias	Calibration Bias	Data Acquisition Bias	Overall Bias
R	8314.472 kJ/kmol °K	0.015 kJ/kmol °K	N/A	N/A	N/A	+/- 0.015 kJ/kmol °K
k	1	3%	N/A	N/A	N/A	+/- 0.03
δ	0.301 m	N/A	N/A	0.0005 m	1.81×10^{-5} m (0.006% FS)	+/- 0.0005 m
z_1	0.002 m	N/A	N/A	0.0005 m	N/A	+/- 0.0005 m
P_c	969.53 Pa	N/A	27.83 Pa (2.87% FS)	69.81 Pa (7.20% FS)	0.06 Pa (0.006% FS)	+/- 75.12 Pa
ΔP	40.56 Pa	N/A	0.042 Pa (0.105% FS)	0.357 Pa (0.88% FS)	0.002 Pa (0.006% FS)	+/- 0.129 Pa
θ_{v_F}	287.47 °K	N/A	0.52 °K (0.18% FS)	0.02 °K (0.0075% FS)	0.02 °K (0.006% FS)	+/- 0.52 °K
θ_{v_1}	341.88 °K	N/A	0.62 °K (0.18% FS)	0.03 °K (0.0075% FS)	0.02 °K (0.006% FS)	+/- 0.62 °K

Since the temperature readings were calibrated against the same thermistor, were acquired through the same data acquisition system, and were reduced using the same calibration equation in the LabVIEW software, the measurements were assumed correlated amongst themselves. One other correlation was also evident which was the use of the same linear scale to determine the heights z_1 and δ. With this in mind, the equation for the propagation of the bias limits is defined as follows.

$$
\begin{aligned}
(X_B)^2 = &\left(\frac{\partial B}{\partial R}X_R\right)^2 + \left(\frac{\partial B}{\partial k}X_k\right)^2 + \left(\frac{\partial B}{\partial P_c}X_{P_c}\right)^2 + \left(\frac{\partial B}{\partial \Delta P}X_{\Delta P}\right)^2 \\
&+\left(\frac{\partial B}{\partial \theta_{v_F}}X_{\theta_{v_F}}\right)^2 + \left(\frac{\partial B}{\partial \theta_{v_1}}X_{\theta_{v_1}}\right)^2 + \left(\frac{\partial B}{\partial \delta}X_{\delta}\right)^2 + \left(\frac{\partial B}{\partial z_1}X_{z_1}\right)^2 \\
&+2\left(\frac{\partial B}{\partial \theta_{v_F}}\right)\left(\frac{\partial B}{\partial \theta_{v_1}}\right)X_{\theta_{v_F}}X_{\theta_{v_1}} + 2\left(\frac{\partial B}{\partial \delta}\right)\left(\frac{\partial B}{\partial z_1}\right)X_{\delta}X_{z_1}
\end{aligned}
\qquad \text{(G-17)}
$$

Again, using the previously calculated sensitivity coefficients and overall elemental biases of each experimental parameter, the corresponding bias limit for the bulk Richardson calculation is ± *7.342 x 10*$^{-6}$. Then, using Equation G-1 and the precision limit factor of $t = 1.96$, the uncertainty in the bulk Richardson number calculation for the fastest velocity run over Test Bed 1 under unstable conditions is ± *8.284 x 10*$^{-6}$. Given that the corresponding value of the bulk Richardson number for the same experimental run was *–8.141 x 10*$^{-5}$, the relative uncertainty is approximately ± *10.2%*. Using the same procedure used in the bulk Richardson number uncertainty, the following table presents the resulting relative uncertainties defined for the corresponding listed experimental parameters calculated in this project.

Parameter Symbol	Description	Relative Uncertainty (± %)
B	bulk Richardson number	10.2
P_c	chamber pressure	7.7
θ_{v_F}	wind tunnel temperature	0.2
ρ_c	chamber density	7.7
μ	dynamic viscosity	0.2
ν	kinematic viscosity	7.7
λ	mean free path	7.7
U_F	freestream velocity	7.7
z_o	roughness height	8.3
u^*	friction speed	7.7
U_{F_t}	freestream speed at dust threshold	9.7